



Wrocław University
of Science and Technology

FIELD OF SCIENCE: ENGINEERING AND TECHNOLOGY

DISCIPLINE OF SCIENCE: MATERIALS ENGINEERING

DOCTORAL DISSERTATION

H₂O₂-modified TiO₂:

Synthesis, Deposition, Properties, and Applications

M.Sc. Eng. Anna Gibas

Supervisors:

Assoc. Prof. Agnieszka Baszczuk, DSc., PhD

Assoc. Prof. Marcin Winnicki, DSc., PhD Eng.

Keywords: TiO₂, oxygen-rich groups, sol-gel synthesis, low-pressure cold spray, suspension spraying

WROCLAW 2025

DISSERTATION DETAILS

Title:	H₂O₂-modified TiO₂: Synthesis, Deposition, Properties, and Applications
Title (in Polish):	TiO ₂ modyfikowany H ₂ O ₂ : synteza, osadzanie, właściwości i zastosowania
Author:	M.Sc. Eng. Anna Gibas ^{1,2}
Supervision:	Assoc. Prof. Agnieszka Baszczuk , DSc., PhD ¹ Assoc. Prof. Marcin Winnicki , DSc., PhD Eng. ²
Affiliation:	¹ Sol-Gel Materials Research Group, Department of Mechanics, Materials and Biomedical Engineering, Faculty of Mechanical Engineering, Wroclaw University of Science and Technology ² Department of Metal Forming, Welding and Metrology, Faculty of Mechanical Engineering, Wroclaw University of Science and Technology
Date of doctoral defence:	2025
Keywords:	TiO ₂ , oxygen-rich groups, sol-gel synthesis, low-pressure cold spray, suspension spraying
Keywords (in Polish):	TiO ₂ , ponadtlenkowe grupy, nadtlenkowe grupy, synteza zol-żel, niskociśnieniowe natryskiwanie na zimno, natryskiwanie zawiesin

Summary:

The presented dissertation consists of a cycle of five scientific articles aiming at developing the synthesis and deposition of H₂O₂-modified TiO₂, which can be applied to the degradation of organic pollutants and bacteria under visible light and in the dark. Selected hydrogen peroxide-based modification is a dopant-free strategy introducing peroxo and superoxo groups which narrows the bandgap energy. The important aspect of the thesis was designing a low-pressure cold spray process for the formation of coatings that maintain the initial characteristics of feedstock materials. The application of feedstock in the form of powder, suspension and aerosolised suspension aimed at investigating the control over the preservation of oxygen-rich groups. The obtained H₂O₂-modified TiO₂ coatings are the results of a synergistic combination of sol-gel synthesis which imparted physicochemical characteristics providing catalytic activity and low-pressure cold spraying that caused thermal drying and offered large-scale technique to produce coatings.

Summary (in Polish):

Na niniejszą rozprawę składa się cykl pięciu artykułów naukowych poświęconych opracowaniu syntezy oraz procesu deponowania TiO₂ modyfikowanego H₂O₂, o potencjale aplikacyjnym do rozkładu zanieczyszczeń organicznych oraz bakterii w świetle widzialnym oraz bez jego udziału. Wybrana modyfikacja oparta na nadtlenu wodoru to strategia niewymagająca domieszkowania, pozwalająca na wprowadzenie do materiału grup nadtlenkowych i ponadtlenkowych, które zmniejszają szerokość pasma wzbronionego. Celem pracy doktorskiej było zaprojektowanie procesu niskociśnieniowego natryskiwania zimnym gazem tak, aby było możliwe wytworzenie powłok o charakterystyce pierwotnych materiałów. Zastosowanie proszków, zawiesin oraz aerozoli zawiesin miało na celu zbadanie wpływu procesu natryskiwania na zachowanie grup bogatych w tlen. Powłoki uzyskane w ten sposób, to synergistyczny efekt syntezy nadającej cechy umożliwiające aktywność katalityczną oraz zastosowanie niskociśnieniowego natryskiwania na zimno jako techniki zapewniającej suszenie oraz obróbkę termiczną uzyskanych materiałów przy zachowaniu skalowalności procesu produkcyjnego.

ACKNOWLEDGEMENTS

I would like to express my gratitude to the following Individuals for their invaluable contributions to this research:

- **My Supervisors**, who readily reviewed each version of the manuscripts, offered reassurance, prepared exciting new collaborations and projects, and supported me in trying new approaches.
 - **My lab team Members**, who provided valuable consultations and advice in professional matters and during all emergencies.
 - Scientist whom I collaborated with:
 - For generously providing access to their equipment essential for research and support during measurements: Daniel Ociński, DSc., PhD, Wrocław University of Economics and Business (DRS), Irena Jacukowicz-Sobala, DSc., PhD, Agnieszka Ciechanowska, PhD, Wrocław University of Economics and Business (photocatalytic activity tests), Magdalena Malik, PhD Eng., WUST (infrared spectroscopy), Konrad Gruber, PhD Eng., WUST (PSA), Aleksandra Małachowska, PhD Eng., WUST (PSA), Mariusz Hasiak, DSc., PhD, WUST (DSC/TGA).
 - For conducting measurements and support in analysis: Wojciech Gil, PhD, University of Wrocław, (TEM), Agnieszka Lewińska, DSc., PhD, University of Wrocław (EPR), Marcin Kuśmierz, PhD, Maria Curie-Skłodowska University (XPS), Ewa Dworniczek, DSc., PhD, M.Sc. Alicja Seniuk, Wrocław Medical University (biocidal activity tests).
 - For consultations: prof. Jerzy Detyna, DSc., PhD Eng., WUST (statistical analysis), Jerzy Łatka, DSc., PhD Eng., WUST (thermal spraying).
 - **My family and friends**, who were genuinely interested in my fancy research and my well-being.
 - **Kuba**, for being, listening and feeding.
-

CONTENTS

LIST OF ABBREVIATIONS AND ACRONYMS	1
LIST OF PUBLICATIONS	2
1 INTRODUCTION	3
1.1 Environmental cleaning	3
1.2 Design of the supported catalyst	7
2 RESEARCH CONCEPT	11
2.1 Rethinking TiO ₂ activity	11
2.2 Development of feedstock materials for the LPCS process	12
2.3 Customization of coatings through LPCS parameters	15
3 AIMS OF RESEARCH	18
4 METHODOLOGICAL CONSIDERATIONS	19
4.1 Sol-gel synthesis	20
4.2 Low-pressure cold spraying	21
4.3 Characterization methods	26
5 Key findings	31
5.1 Influence of H ₂ O ₂ modification	31
5.2 Innovative approaches to oxygen-rich coatings	31
5.3 Thermal drying of sol-gel material by LPCS	32
5.4 Main conclusions	33
6 OUTLOOK	36
7 REFERENCES	37
8 LIST OF TABLES AND FIGURES	40
9 SCIENTIFIC ACHIEVEMENTS	41
9.1 Summary of scientific achievements	41
9.2 Scientific contributions	45
10 REPRINTS	55

LIST OF ABBREVIATIONS AND ACRONYMS

ANOVA	Analysis of variance
CS	Cold spray
DRS	Diffuse reflectance spectroscopy
DSC	Differential scanning calorimetry
EEA	European Environment Agency
E_g	Bandgap energy [eV]
EPR	Electron paramagnetic resonance
IR	Infrared (radiation)
ISO	International Standards Organisation
IUPAC	International Union of Pure and Applied Chemistry
LPCS	Low-pressure cold spray
MB	Methylene blue
Oxygen-rich groups	Peroxo and superoxo groups
P25	Commercially available crystalline titanium(IV) dioxide (Evonik, Germany, formerly Degussa)
pH_{PZC}	pH of the point of zero charge
PM	Particulate matter
PSA	Particle Size Analysis
ROS	Reactive oxygen species
SA	Surface area [μm^2]
SEM	Scanning electron microscopy
TEM	Transmission electron microscopy
TGA	Thermogravimetric analysis
TIPO	Titanium(IV) isopropoxide
TOC	Total organic carbon [mg/dm^3]
TS	Thermal spray
UV	Ultraviolet light
Vis	Visible light
WUST	Wroclaw University of Science and Technology
XPS	X-ray photoelectron spectroscopy
XRD	X-ray powder diffraction

LIST OF PUBLICATIONS

This thesis is based on five peer-reviewed articles [A-E].

Table 1 Compilation of metadata of publications

[A]	A. Gibas, A. Baszczuk, M. Jasiorski, M. Winnicki, D. Ociński, Preparation of visible-light active oxygen-rich TiO₂ coatings using low pressure cold spraying , Coatings, 31.03.2022, DOI: 10.3390/coatings12040475.	MEiN (2019-2022): 100 IF (2022): 3.4 Quartile: Q2
[B]	A. Gibas, M. Winnicki, A. Baszczuk, M. Jasiorski, Influence of spraying parameters on microstructure of oxygen-rich TiO₂ coatings deposited using suspension low-pressure cold spray , Surface & Coatings Technology, 14.02.2023, DOI: 10.1016/j.surfcoat.2023.129321.	MEiN (2023): 100 IF (2023): 5.3 Quartile: Q1
[C]	A. Gibas, A. Baszczuk, M. Jasiorski, A. Lewińska, M. Winnicki, Low-pressure cold spraying of suspension TiO₂ in a single pass – Process optimization , Surface & Coatings Technology, 19.08.2023, DOI: 10.1016/j.surfcoat.2023.129933.	MEiN (2023): 100 IF (2023): 5.3 Quartile: Q1
[D]	A. Gibas, M. Winnicki, A. Baszczuk, M. Jasiorski, Aerosol-assisted low-pressure cold spraying of TiO₂ suspension , Surface & Coatings Technology, 26.12.2024, DOI: 10.1016/j.surfcoat.2024.131715.	MEiN (2024): 100 IF (2023): 5.4 Quartile: Q1
[E]	A. Gibas, A. Baszczuk, I. Jacukowicz-Sobala, A. Ciechanowska, M. Jasiorski, E. Dworniczek, A. Seniuk, A. Lewińska, H₂O₂-sensitized titania with activity under visible light and in the dark , Journal of Environmental Chemical Engineering, 30.08.2024, DOI: 10.1016/j.jece.2024.113975.	MEiN (2024): 100 IF (2023): 7.4 Quartile: Q1

The thesis is further supported by a patent application [F].

- [F] **Method of deposition of functional aerosol coatings from the liquid phase**, original title: Sposób nanoszenia funkcjonalnych powłok z aerozolu z fazy ciekłej, signature number P.442330, reported 21.09.2022 by Wrocław University of Science and Technology, authored by M. Winnicki, A. Gibas, M. Jasiorski, A. Baszczuk.

1 INTRODUCTION

1.1 ENVIRONMENTAL CLEANING

Environmental contamination is a persistent global issue driven by rapid industrialization and urbanization, leading to the release of hazardous chemicals that pose a severe threat to Earth's ecosystems and biodiversity. The European Environment Agency (EEA) highlights significant environmental challenges across Europe. According to Europe's State of Water 2024 [1], only 29% of surface water bodies and 77% of groundwater achieved good chemical status in 2021, as defined under the Water Framework Directive standards. The report identifies that energy generation and agriculture sectors pose the most significant threat to water quality. Priority substances, including pharmaceuticals, brominated flame retardants or polycyclic aromatic hydrocarbons, are challenging to decompose due to their toxicity, and bioaccumulative nature. However, their proper degradation ensures that these substances do not persist in the environment, reducing human health risks and preventing long-term environmental damage.

1.1.1 WATER CLEANING SYSTEMS

The renewal of clean water supplies requires effective water purification processes to meet environmental standards [1]. The comprehensive water purification system consists of various sectors including ultrapure water production, groundwater treatment, air purification, soil remediation, municipal wastewater sludge conditioning, and water and wastewater treatment [2].

Wastewater treatment is a multi-step process with various methods that can be categorised into physical, biological, chemical, and hybrid processes [3]. Physical techniques are used for preliminary wastewater handling [2,3]. Sedimentation, floatation, filtration, etc. focus on the separation of solid waste (sands, metals) or oil media (grease, fats) for their recovery and potential conversion into useful chemicals [2]. Biological methods decompose biodegradable matter including fats, proteins, alcohols, carbohydrates, nitrates and sulphates through aerobic, anaerobic or anoxic procedures. Microbial communities optimized for specific waste types metabolize pollutants converting them into water, carbon dioxide, and, in some systems, bioelectricity [4]. The biological slurry can be then used as biofuels [2]. However, as biological processes depend on living organisms, their activity is time-intensive and constrained by the stability of operational

conditions - such as waste composition, pH, and temperature, to prevent bacterial inhibition or death [5–7]. Chemical treatment often yields faster results than biological methods, but it relies on expensive disposable reagents. Techniques such as precipitation, coagulation, flocculation, and disinfection are effective for removing dissolved pollutants (nutrients, pharmaceuticals or organic chemicals). However, produced chemical slurry may contain a variety of chemical compounds requiring different treatment or recycling methods [4,7].

Unlike processes that result in secondary pollution, advanced oxidation processes (AOPs) offer a complete degradation strategy for organic pollutants [6]. Oxidative degradation reactions can be integrated into the degradation process at any stage as pre-, main, and post-treatment [8]. AOPs generate reactive oxygen species (ROS), mainly $\cdot\text{OH}$ radicals [7,8]. The non-selective character of radicals causes degradation of target pollutants and intermediates, ultimately leading to complete mineralization into harmless products like CO_2 and H_2O [6]. Depending on the type of pollution, the ROS can be generated using different forms of energy including electromagnetic (photolysis, photocatalysis), thermal (hydrothermal treatment, thermal activation), mechanical (ultrasounds, cavitation), electrical (current, plasma) or chemical (ozonation, peroxide, Fenton) energies [4,7]. To achieve synergistic removal of heavy pollution, several processes are typically combined into hybrid procedures, such as UV/peroxide/ozone or photo-electrocatalysis [4,6–8].

1.1.2 TITANIUM DIOXIDE

Photocatalysts stand out in AOPs for their reusability, as they are not consumed during degradation reactions. The most popular photocatalyst is titanium dioxide [6]. TiO_2 is a versatile semiconductor known for its exceptional optical and electrical activity. When exposed to light with energy larger than its bandgap energy (E_g), the photocatalyst absorbs a photon which excites an electron (e^-) to the conduction band, leaving a hole (h^+) in the valence band. Then the electron participates in reduction reactions, such as converting oxygen (O_2) to superoxide radicals ($\text{O}_2^{\cdot-}$), while the hole drives oxidation reactions, such as transforming water (H_2O) into hydroxyl radicals ($\cdot\text{OH}$).

Photocatalytic activity depends on several factors, which can be categorized based on their role in the degradation process. Key elements of a photocatalytic pollution degradation system include the pollutant, excitation source and catalyst.

- Pollutant-related catalytic efficiency depends on the physicochemical characteristics of the target pollutants, including solubility, polarity, surface charge, chemical bonding, and concentration which determine the choice of catalyst and decomposition procedure. For example, hydrophobic pollutants (oils, hydrophobic pesticides) require the addition of surfactants or organic solvents [9,10], while water-soluble pollutants (phenolic compounds, pesticides) are readily accessible for degradation in aqueous environments. Non-polar pollutants (oils, aromatic hydrocarbons) primarily undergo degradation through direct oxidation procedures. In contrast, polar pollutants (phenolic compounds, antibiotics) strongly adsorb onto the catalyst surface, allowing degradation via surface-driven reactions [11]. The adsorption is enhanced by the opposite charge of pollutant and catalyst surfaces. As a result, TiO_2 surfaces may adsorb selectively cationic dyes (e.g. methylene blue) and anionic dyes (e.g. congo red), depending on the material's pH-dependent surface charge [11]. Weakly-bonded pollutants (dyes, pharmaceuticals) are easily-degraded in simple procedures while chemically stable pollutants (personal care products, perfluoroalkyl and polyfluoroalkyl substances, microplastic) require hybrid processing [5,7,12]. Degradation of pollution depends also on its concentration. When too high, it can saturate the catalyst's active sites and hinder catalytic efficiency.
- Light-related catalytic efficiency is closely connected to the energy absorption, restricted by the bandgap width of the photocatalyst. Consequently, only a limited range of wavelengths can be absorbed. Suitable light can be delivered from a wide range of sources, including natural (the Sun) and artificial (lamps and diodes) sources. Sunlight, a renewable energy source, contains approximately 7% ultraviolet (UV) radiation, 43% visible light, and 49% infrared radiation [13] and is limited by daylight conditions, weather, seasons and geographic location. Whereas artificial light sources offer constant illumination with tailored spectra and controlled light intensity.
- Catalyst-related catalytic efficiency is determined by the properties of the catalyst including the electron structure, stability, reactivity, surface charge, selectivity, particle size, surface area, morphology, and form. TiO_2 -based materials are generally UV-activated photocatalysts and are characterized by high chemical stability, non-toxicity and high resistance to corrosion and light. Particle size is frequently controlled through synthesis because nanomaterials are favoured for

their higher specific surface area-to-mass ratio compared to larger equivalents [10]. Photocatalysts exist in various forms, including fine particles, powders, or granules. They can be used as bulks (unsupported catalysts), membranes or coatings (supported catalysts) [12]. Suspended catalysts exhibit generally higher reactivity than immobilized ones, but their post-process separation is more challenging [10,12]. Because nanomaterials pose ecological and health risks when released into the environment [14], the supported catalysts are preferred.

1.1.3 STRATEGIES FOR VISIBLE LIGHT AND DARK ACTIVITIES

The photocatalytic potential of titanium dioxide is limited due to a large bandgap energy (3.0 to 3.2 eV, requiring irradiation with ultraviolet light) and the rapid recombination of photo-excited charge carriers. To extend its applicability and overcome limitations associated with UV-only activation, recent efforts focus on reducing the bandgap for visible light activation and improving charge separation.

Several attempts were made thereby to enhance the efficiency of TiO_2 , including two basic methodologies: bandgap engineering and junction engineering [13]. Bandgap engineering interferes with band structure by changing the original positions of valence and conduction bands or introducing new midgap states by forming extrinsic defects (metal and nonmetal doping or metal-nonmetal codoping) or intrinsic defects, such as Ti^{3+} or oxygen vacancies [13]. Junction structures are formed by coupling semiconductors, which align their energy bands in a way that enhances charge separation and reduces recombination [13]. However, coupling additive materials or doping various elements to TiO_2 may favour the undesired charge recombination and hamper recyclability.

Hydrogen peroxide-based modification, introducing intrinsic defects, is a dopant-free strategy imparting a characteristic yellow colour as a side-effect [15]. Simple soaking in H_2O_2 may introduce several changes such as diverse oxygen-rich groups (Figure 1), including peroxo and superoxo groups, which provide the photocatalytic activity observed under visible-light radiation [4,16]. Interestingly, the oxygen-rich groups prove advantageous also for the non-light-driven catalytic removal of organic contaminants [17,18]. Apart from the dark degradation of organic pollutants, H_2O_2 -modified TiO_2 demonstrates bactericidal properties [19,20].

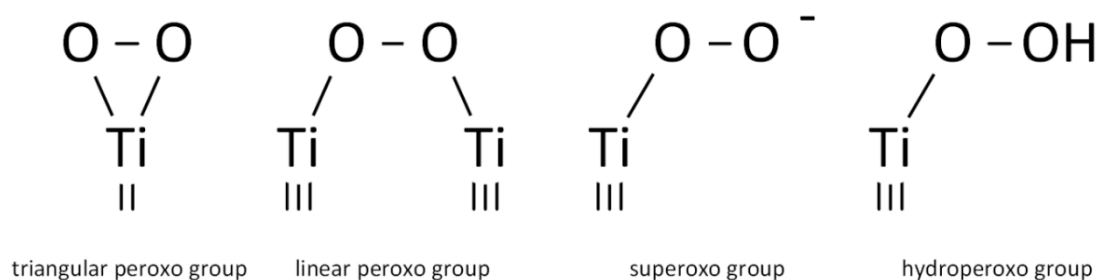


Figure 1 Scheme of the oxygen-rich groups [E]

The analysis of recent studies on H_2O_2 -modified TiO_2 reveals two key trends. H_2O_2 is an oxidant used for the modification of TiO_2 or in situ pollution degradation [E]. The modification process is either part of bottom-up synthesis or the top-down adjustment. Most of the H_2O_2 -modified TiO_2 is thermally treated to achieve crystalline phases. The visible-light photocatalytic activity is caused by material modification causing surface hydroxylation, defected structure or the presence of peroxo groups [11,21–24]. In contrast, when H_2O_2 is added in situ, dark activity is often observed, which is explained to be caused by the presence of superoxo groups [17,18,25].

1.2 DESIGN OF THE SUPPORTED CATALYST

1.2.1 SOL-GEL SYNTHESIS

The bottom-up approach for synthesizing oxygen-rich TiO_2 typically involves the aqueous peroxo-titania sol-gel route [11]. Liquid-phase processes offer versatile morphologies, scalable processes and cost-effective solutions, compared to vapour-based and solid-phase methods [14,15,26]. The sol-gel technique offers high control over catalyst-related features, including structure, size and functionality [14,27].

According to the International Union of Pure and Applied Chemistry (IUPAC), the sol-gel route is “a process through which a network is formed from solution by a progressive change of liquid precursor(s) into a sol, to a gel, and in most cases finally to a dry network” [28]. The sol-gel method operates at relatively low temperatures and ambient pressures [29]. The change from solution to sol proceeds via hydrolysis and condensation reactions while from sol to gel through further condensation (Figure 2). Then the wet gel is dried to remove physically adsorbed water and organic solvents and chemically adsorbed hydroxyl groups and precursor residues [29,30]. Drying processes necessitate

post-synthesis treatments, including supercritical drying, freeze drying or thermal drying. Thermal drying, such as calcination, is commonly used to achieve the desired crystallinity [30]. Considering wet gels are prone to significant volume shrinkage, heat treatment at inappropriate temperatures and rates may cause cracking [29]. This issue is, however, of lesser importance in the production of powders.

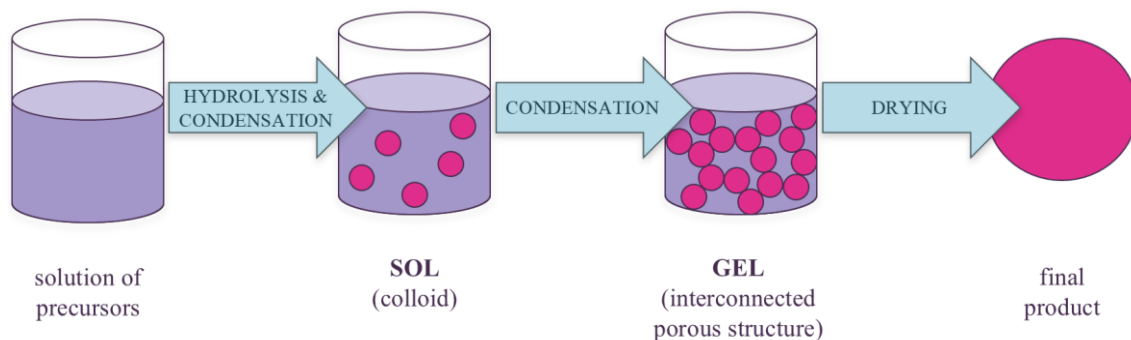


Figure 2 Sol-gel route

1.2.2 THERMAL SPRAYING OF SOL-GEL MATERIALS

From the economical and structural point of view, photocatalyst in the form of coating is more versatile and highly recommended, provided the risk of nanomaterial release is minimized [12]. Unfortunately, coating formation causes the aggregation of the nanomaterials, which reduces the active surface area compared to the suspended particles [14]. Many nanostructured coating formation methods facilitate smooth surfaces only [10,14]. But, unlike them, thermal spraying (TS) uniquely offers a wide range of surface roughness, from coarse to smooth [31] enabling the partial retrieving of initial high surface area-to-mass ratio properties of nanomaterials [10].

Although it is not common, thermal spraying can be coupled with sol-gel synthesis. Sol-gel materials including TiO_2 , SiO_2 , ZrO_2 , Al_2O_3 or hydroxyapatites with tailored chemical composition and functionality may serve as feedstock material for thermal spraying. Whereas thermal spraying can function in two ways. Firstly, it may be used as a thermal drying technique for the removal of the residual solvents, full condensation of the network and removal of synthesis residues. Additional delivered thermal energy is usually consumed on phase transformations [32]. Secondly, thermal spraying offers a scalable method for the production of reproducible coatings.

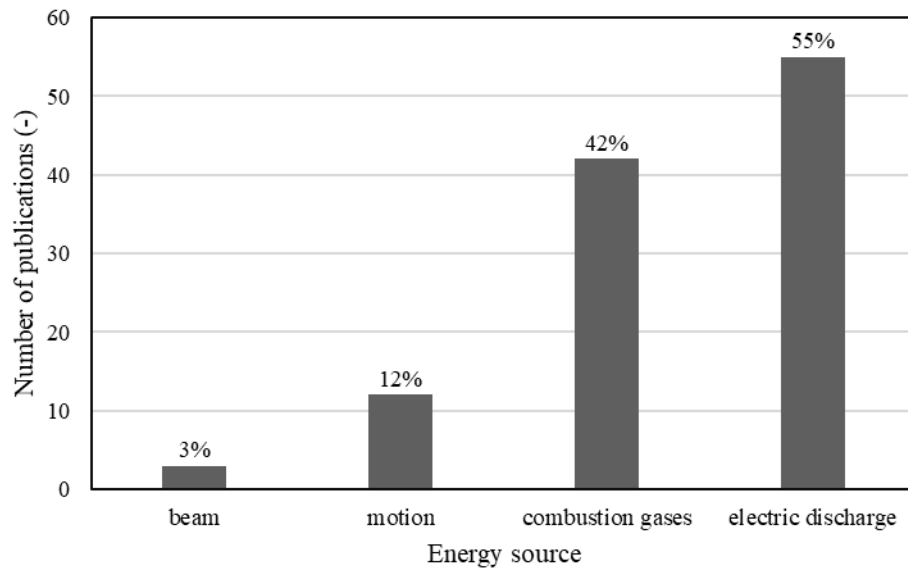


Figure 3 Analysis of current literature on thermal spraying of sol-gel materials based on used energy source for spraying¹

It is highly convenient that the sol-gel process can be stopped at every step of the synthesis. Sol-gel can be fed in the form of sol-gel solution (precursors or mixture of precursors), suspension (typically powders suspended in the dispersion medium), or powder [14][33] (Figure 2). Solution spraying forms smooth, crack-free structures, while powder spraying provides appropriate porosity and roughness [34,35]. The wet gel is commonly used to form powders and coatings. The powders are mostly produced for catalytic purposes, which require high crystallinity, that can be obtained through high-temperature treatments, such as flame pyrolysis or plasma spraying [36]. Photocatalytic coatings may be produced using flame, plasma, high-velocity oxy-fuel and cold spray [14]. However, the potential uses of coatings extend far beyond photocatalytic activity. Coatings may appear as monolithic, gradient, and multilayer structures. In thermal sprayed multilayers, sol-gel materials play the role of topcoats, interlayers and bond coats deposited on various substrates. Topcoats are used primarily as a sealing agent to decrease porosity. Other applications include increasing the wear, corrosion, or thermal resistance

¹ Based on the analysis of 287 paper found using the inquiry AB=("thermal spray*" OR "flame spray*" OR "detonation spray*" OR "high velocity spray*" OR "high velocity oxy fuel" OR "cold spray*" OR "plasma spray*" OR "laser spray*" OR "laser clad*") AND ALL=("sol-gel*" OR "Sol-gel" OR "sol gel" OR "Sol-gel process" OR "sol-gel process" OR "sol gel process" OR "sol-gel synthesis" OR "sol-gel synthesis" OR "sol gel synthesis") among which 113 was verified to contain the topic of thermal spraying of sol-gel materials

and providing proper roughness and biocompatibility of the outer surface. Interlayers and bond coats usually improve thermal shock resistance and cohesion between layers.

Analysis of current literature on thermal spraying of sol-gel materials conducted for this thesis (Figure 3) shows that the most popular techniques are plasma spraying (55%) and flame pyrolysis (42%). Few papers, investigate laser cladding (3%) and cold spraying (12% of which 7% constitute papers authored by the research team of which the author of this thesis is a member).

1.2.3 COLD SPRAYING OF SOL-GEL MATERIALS

Among thermal spraying techniques, cold spraying is particularly advantageous by operating at lower temperatures, because it may preserve the features of heat-sensitive feedstock materials, which H_2O_2 -sensitized TiO_2 surely is [37,38]. Traditionally, the cold spray technique has been used for metal spraying, leveraging the ductility of metals and the advantages of low-temperature deposition to preserve their properties without causing surface oxidation or phase changes [37]. Hard ceramic powders were used preliminary as an admixture to metal powder for reinforcement and densification [37]. However sol-gel materials without thermal treatment may be prone to ductile-like behaviour at the microscale, which enables the formation of coatings due to mechanical interlocking [32,39,40]. Considering the success of the research team to which the doctoral candidate belongs in spraying unmodified TiO_2 [32], cold spraying was chosen to develop oxygen-rich TiO_2 coatings in this thesis.

2 RESEARCH CONCEPT

The chapter outlines the key research areas related to oxygen-rich TiO₂ materials, focusing on their applications, properties, synthesis and deposition. This thesis specifies 9 research aspects based on current scientific knowledge, complemented by the explicit contributions provided within this thesis, and highlights of potential challenges for future considerations.

2.1 RETHINKING TiO₂ ACTIVITY

When considering the activity of TiO₂-based materials, current trends include photocatalyst activation by visible light, achieving activity in darkness, and the use of amorphous titanium dioxide.

2.1.1 VISIBLE-LIGHT ACTIVITY

TiO₂ has been proven active photocatalyst against over 1000 substances, including pesticide residues, drugs, and hormones, as well as nitrogen oxides, toxic fumes, cigarette smoke, viruses, fungi and bacteria [12,17,18,25,26]. Overcoming UV-only activation that is harmful to living organisms could broaden the applicability of already-developed UV-induced photocatalytic solutions. Visible-light activation is more practical for integration into human environments, as it operates efficiently under natural sunlight and human-neutral artificial lighting. Additionally, it enables clean energy applications, such as solar water splitting for hydrogen production and CO₂ reduction into valuable fuels.

Contribution: The modification of TiO₂ with H₂O₂ is designed to provide visible-light activity against standard organic pollutant (methylene blue) [A,C,E].

Possible issue: The visible-light activity in model pollutant degradation may be caused by the in-situ addition of H₂O₂ [23] dye sensitization [41] or adsorption [24].

2.1.2 DARK ACTIVITY

Recent studies show that TiO₂ can be active in the degradation of organic pollutants and microorganisms for some time after removal of radiation and TiO₂ can be active independently on the delivered light [25]. The dark activity was observed for the oxidised surface of titanium implants [20] or coloured TiO₂, mainly black TiO₂ [18]. Especially interesting is yellow TiO₂ as the addition of H₂O₂ provides dark activity in a facile, room

temperature, dopant-free manner (Chapter 1.1.3). Catalysis in the dark holds promise for implant applications (devoiding light) and continuous cleaning processes (not necessarily under continuous illumination), particularly in medical settings, where certain bacteria may persist under photocatalytic conditions and recover in the absence of light [17][18].

Contribution: The modification of TiO_2 with H_2O_2 is designed to provide dark activity against standard organic pollutant (methylene blue) and microbes (*Escherichia coli*, *Enterococcus faecalis*) [E].

Possible issue: Observed dark activity may be partially caused by the exposure to daylight that occurred during synthesis and drying.

2.1.3 ACTIVITY OF AMORPHOUS MATERIALS

Commercially available TiO_2 (P25), a standard photocatalytic material, is composed of anatase, rutile and amorphous particles. Their junction can provide a synergistic effect as anatase is active in oxidative decomposition reactions while rutile - for reductive pathways [42]. Thermal treatment is used to increase crystallinity and get rid of the amorphous phase which is considered inactive [42]. Current research shows, however, that amorphous materials may be active photocatalyst, too [43]. The amorphous phase as the name suggests, is characterized by long-range disorder. Defects may promote charge carrier generation, improve charge separation and transfer efficiency, all of which enhance visible light absorption [13,42]. Additionally, amorphous TiO_2 is a perfect surface adsorbent [44]. What is even more interesting, some researchers observe an even higher photocatalytic activity of amorphous titanium dioxide compared to its commercially available crystalline version, P25 [43,44].

Contribution: The modification of TiO_2 with H_2O_2 is designed to produce an amorphous structure with defects ensuring visible-light activity of the material in the form of powder [A,E] and coating [A,B,C,D].

Possible issue: (1) Amorphous TiO_2 is unstable in aqueous media (photo-corrosion) [43]. (2) Defects may serve as recombination centres that limit the activity [13,42].

2.2 DEVELOPMENT OF FEEDSTOCK MATERIALS FOR THE LPCS PROCESS

Developing feedstock materials for LPCS requires a thorough evaluation of their initial functionality, as it directly influences the characteristics of the formed coating. It is also

essential to determine whether such materials are suitable for deposition. Moreover, the deposition process may be analysed for its potential to contribute to material preparation which may provide additional features and shorten the production time.

2.2.1 DESIGNING AOP ACTIVITY

Few reports study coatings which underwent top-down H_2O_2 -modification [17] probably due to the difficult formation of coatings from H_2O_2 -modified TiO_2 . Therefore, in designing active feedstock for thermal spraying, analysis of literature on TiO_2 in AOP technologies [15,18] may give useful insights. Generally, H_2O_2 is used as a strong oxidant in UV/ H_2O_2 and UV/ TiO_2 / H_2O_2 systems due to its ability to in-situ generate reactive oxygen species (ROS), including reactive hydroxyl radicals ($\cdot\text{OH}$) [41]. Although H_2O_2 decomposition is spontaneous, UV-photolysis can improve and control its decomposition rate [5]. In UV/ TiO_2 / H_2O_2 systems, the presence of metal ions catalyses the decomposition of H_2O_2 at the TiO_2 interface and enables the formation of different radicals, such as superoxide radicals ($\text{O}_2^{\cdot-}$) and hydroperoxyl radicals (radical $\cdot\text{OOH}$). Both radicals ($\text{O}_2^{\cdot-}/\cdot\text{OOH}$) can be stabilized on metal oxide surfaces [19] to form metal-dioxygen complexes, called oxygen-rich groups (Figure 1) that can be excited during degradation processes. Apart from oxygen-rich groups, the literature review in [E] displays that the common material features providing AOP activity are surface hydroxylation, phase composition, and defects in the structure. Those features can be introduced into the material before the degradation processes. The resulting material structure determines which reactive oxygen species, including $\cdot\text{OH}$, $\text{O}_2^{\cdot-}$, $\cdot\text{OOH}$, or photogenerated intermediates, such as $[\equiv\text{Ti}^{\text{IV}}-\text{OOH}]^\bullet$ and $[\equiv\text{Ti}^{\text{III}}-\text{OOH}]^-$, are preferentially formed during the test [11].

Contribution: The synthesis of feedstock TiO_2 is followed by the modification with H_2O_2 favouring the formation of oxygen-rich groups, intermediates and radicals to provide visible light and dark activity without relying on in situ addition of H_2O_2 and UV light [A,E].

Possible issue: (1) Excited oxygen-rich groups on TiO_2 may be consumed and fail to regenerate during the degradation processes [11]. Their regeneration may require H_2O_2 treatment [17,24]. (2) Oxygen-rich groups are thermally-sensitive [11] and may not sustain the LPCS process.

2.2.2 IMPARTING DUCTILITY

The principal disadvantage of low pressure cold spaying is the limited range of feedstock materials as this technique was developed for metals which are ductile [37]. It is impossible to plastically deform hard and brittle ceramic materials, such as crystalline TiO_2 [37]. The typical way to embed ductility or deformability of TiO_2 is to combine it with commercially available polymer powder, such as polyvinyl alcohol [37,39]. Some studies show, however, that amorphous oxides such as SiO_2 or Al_2O_3 may exhibit ductile behaviour [45], too. The most effective way to obtain amorphous TiO_2 is to produce it using sol-gel synthesis (Chapter 1.2.1). Apart from promising amorphicity, wet processing gives control over the particle size and agglomeration. Too small particles may be ejected outside the carrier gas stream, so nanoparticles can be deposited using LPCS only in the form of agglomerates [37]. TiO_2 network formed upon sol-gel synthesis encompasses residues of precursors and byproducts like alcohols and adsorbed water. The synthesis residues bind the TiO_2 particles in weakly-bonded agglomerates [32]. Such agglomerates may be then fractured, slipped and compacted to form coatings, which provide so-called ductile-like behaviour [40] ensuring higher deposition efficiency [37]. Hence the heat treatment of the sol-gel TiO_2 may be intentionally omitted to sustain the amorphous structure with the synthesis residues [32]. To maximise further the deposition efficiency of TiO_2 feedstock the substrate material can be selected to be ductile. The evident choice is aluminium, as it tends to jet at the impact of incoming particles enhancing particle attachment [34][40].

Contribution: The synthesis of H_2O_2 -modified TiO_2 was conducted using the sol-gel method without following heat treatment to produce an amorphous metal-oxygen network, full of synthesis residues which can act as a binder upon deposition and can be easily anchored on the aluminium substrate [A].

Possible issue: Room-temperature dried TiO_2 may contain irregular shapes and intra-agglomerate pores which may cause the formation of undesired closed porosity that reduces the mechanical properties of the formed coating [39].

2.2.3 PROVIDING THERMAL DRYING

While the sol-gel process begins with a liquid precursor, the final product is a solid. The liquid phase is removed via supercritical, freeze or thermal drying (Figure 2). Apart from

the removal of organic residues, thermal treatment is used to change chemical, textural, morphological and crystallographic properties [30,35]. Among thermal post-treatment methods of sol-gel materials, calcination is the standard approach [30,32]. Some attempts have been made to produce sol-gel coatings using air-spraying, but additional calcination is needed to achieve the desired properties [46]. Although this approach remains relatively unknown (Figure 3), instead of traditional long-lasting or energy-consuming heat treatment, thermal spray offers a scalable alternative for thermal drying (Figure 2, Chapter 1.2.2). Either room-dried powders or wet gels can be fed to a spraying gun.

Contribution: LPCS was used as an integrated solution to sol-gel synthesis offering scalability in coating formation and thermal treatment of liquid residues remaining after condensation (wet gel) [B,C,D] or room temperature drying [A].

Possible issue: Undried sol-gel materials are characterized by reduced flowability which hinders their transport from the feeder to the spraying gun [47].

2.3 CUSTOMIZATION OF COATINGS THROUGH LPCS PARAMETERS

The final characteristics of the deposited coating can be controlled by adjusting the parameters of deposition. Modifications of the low-pressure cold spray setup can address the limitations of the feedstock materials.

2.3.1 DEPOSITION PARAMETERS-DEPENDENT EFFECTS

Coating quality depends on the deposition parameters. Selecting appropriate parameters is challenging, as there are dozens of possible spraying parameters to consider [48]. The first group of parameters involve feedstock material characteristics, the second contains spraying setup characteristics including carrier gas, manipulator, nozzle and feeding, whereas the third is pre- and post-spraying treatment methods [48]. For LPCS (Chapter 1.2.3), generally, the most important parameters are pressure and temperature as they limit the accessible particle velocities [37]. Increasing delivered thermal energy is crucial for ensuring the homogeneity of the produced coatings and facilitates rough surface development [33,37]. LPCS is generally an air-based technique [39] but for better quality, it can be coupled with inert gases or vacuum [35]. It is worth noting that the continuous coating can be produced in the range of parameters (a window), not a single specific combination (a point) [39].

Contribution: Increasing carrier gas temperature enables coating formation from H_2O_2 -modified TiO_2 [A]. Partially and fully condensed sol differently react on delivered thermal energy [B]. Proper particle size distribution causes sufficient momentum of particles and enables coating formation [D]. The formation of discontinuities can be limited using a plan of experiments [C].

Possible issue: (1) Window of deposition for ceramic powders is significantly lower compared to metallic powders [37,39,49]. (2) The currently deposited ceramics LPCS coatings are characterized rather by poor quality (porosity and insufficient particle interlocking) [34,39] (3) Rapid drying of sol-gel materials may cause cracking [29].

2.3.2 COMBATING THERMAL-SENSITIVITY

Although LPCS keeps a low-temperature regime it may cause feedstock material changes, such as an increase in grain size, phase transition or decomposition of O-O species [34]. Given the thermal sensitivity of oxygen-rich complexes [11], their presence and stability in the final product need to be assured by omitting high temperature or pressure post-treatment. To lower the risk of preheating, feedstock material can be used in liquid form [38]. Water and alcohols are the most used solvents in other thermal spraying techniques [33]. Liquid share enables control of the agglomeration of fine particles and their sedimentation [33,38]. In the case of sol-gel material, the synthesized particles may remain suspended in the post-synthesis mixture containing water, unreacted precursors and synthesis by-products which eliminates the need for the application of additional solvents. Additionally, such a wet gel may include a higher solid content compared to a conventional slurry composed of particles and solvent [33]. Thus, the application of H_2O_2 -modified TiO_2 wet gels as feedstock material reduces total coating production time by eliminating the drying step (about a week in the room conditions) and repurposes synthesis residues which minimize waste and consumption of chemicals.

Contribution: Suspension spraying leads to the efficient material use and preservation of amorphous TiO_2 with oxygen-rich structures upon spraying [B,C].

Possible issue: The residues containing H_2O_2 which are trapped in the coating cause coating disintegration due to H_2O_2 -containing bubble collapse [B,C]. Poorly evaporated liquid increases thermal shock and causes cracking [46].

2.3.3 RESIDUES EVAPORATION

Excess liquid can lead to inefficient material use due to overspray and increased coating defects due to cracking [46]. The obvious solution is to increase thermal energy, but increasing energy can cause changes in the composition and hence is not suitable for heat-sensitive materials. Another solution for enhanced liquid evaporation is better control of the droplets that can be provided using non-continuous feeding systems – aerosolization of the feedstock suspension. Liquid aerosol formation can be done using an atomizer, including pneumatic, hydraulic and sonic atomizers [33]. The atomizer breaks the suspension into separate droplets. The formation of mist gives control over the diameter of liquid particles [50]. The high kinetic energy of carrier gas in cold spraying may induce evaporation [50]. The final structure of the coating depends on the droplet flattening [50]. The behaviour of large liquid droplets is similar to the behaviour of solid particles of adequate size [33]. In other thermal spraying techniques, usually liquid evaporates before reaching the substrate material [51].

Contribution: The aerosolization of feedstock suspension enhances the complete removal of residual H_2O_2 -containing liquid and hence retains coating integrity [D].

Possible issue: Rare commercial spraying guns for liquid injection are not designed for cold spraying [33].

3 AIMS OF RESEARCH

The thesis aims at the development of oxygen-rich TiO_2 coatings deposited using low pressure cold spraying of sol-gel synthesized TiO_2 modified with H_2O_2 . This dissertation addresses gaining a better understanding of the spraying parameters on TiO_2 embedding and preserving oxygen-rich structures. Produced coatings are meant to demonstrate visible-light activity. Additionally, the dark activity of powders is investigated.

The main aims can be summed up with regard to each study:

Table 2 Compilation of main aims

[A]	The oxygen-rich powder is designed using an aqueous peroxo-titania sol-gel route. The effects of H_2O_2 modification are confirmed by the presence of oxygen-rich groups and the reduction of the bandgap width. Feeding as-synthesized amorphous powder without thermal treatment provides ductile-like behaviour during spraying. The maximum range of carrier gas temperature is used to show wide deposition widow. The dye degradation test verifies visible-light activity.
[B]	The oxygen-rich suspension is used instead of powder to combat the thermal sensitivity of feedstock (retain the chemical and structural changes) and reduce the total production time (no drying step). Relatively high carrier gas temperature is used but deposition is controlled additionally by manipulator movement.
[C]	The oxygen-rich suspension is sprayed with parameters of ranges selected based on [B] to provide the same chemical and optical structure as powders [A] . The spraying parameters are optimized for bandgap energies and surface area to reduce the number of performed photocatalytic tests. The dye degradation test verifies the visible-light activity of the coating sprayed with optimal parameters.
[D]	The oxygen-rich suspension is atomized for spraying to improve the removal of residual H_2O_2 -containing liquid and improve coating integrity. The influence of the preparation of suspension is investigated with respect to the formed coating.
[E]	The oxygen-rich, H_2O_2 -modified powder [A] is compared with unmodified TiO_2 and P25 to investigate the factors contributing to its visible-light and dark activity verified in dye degradation and bacteria-killing tests.

4 METHODOLOGICAL CONSIDERATIONS

This thesis analyses H_2O_2 -modified TiO_2 (coloured blocks in Figure 4) in various forms.

- The **coating** is produced by the spraying of feedstock material in the form of powder, suspension (wet gel formed via the sol-gel reactions without consecutive drying) and aerosol of suspension.
- The **powder** is obtained by ambient drying of suspensions at room temperature.

Unmodified sol-gel synthesised TiO_2 and typical commercial TiO_2 , P25, were investigated for comparison (white blocks in Figure 4).

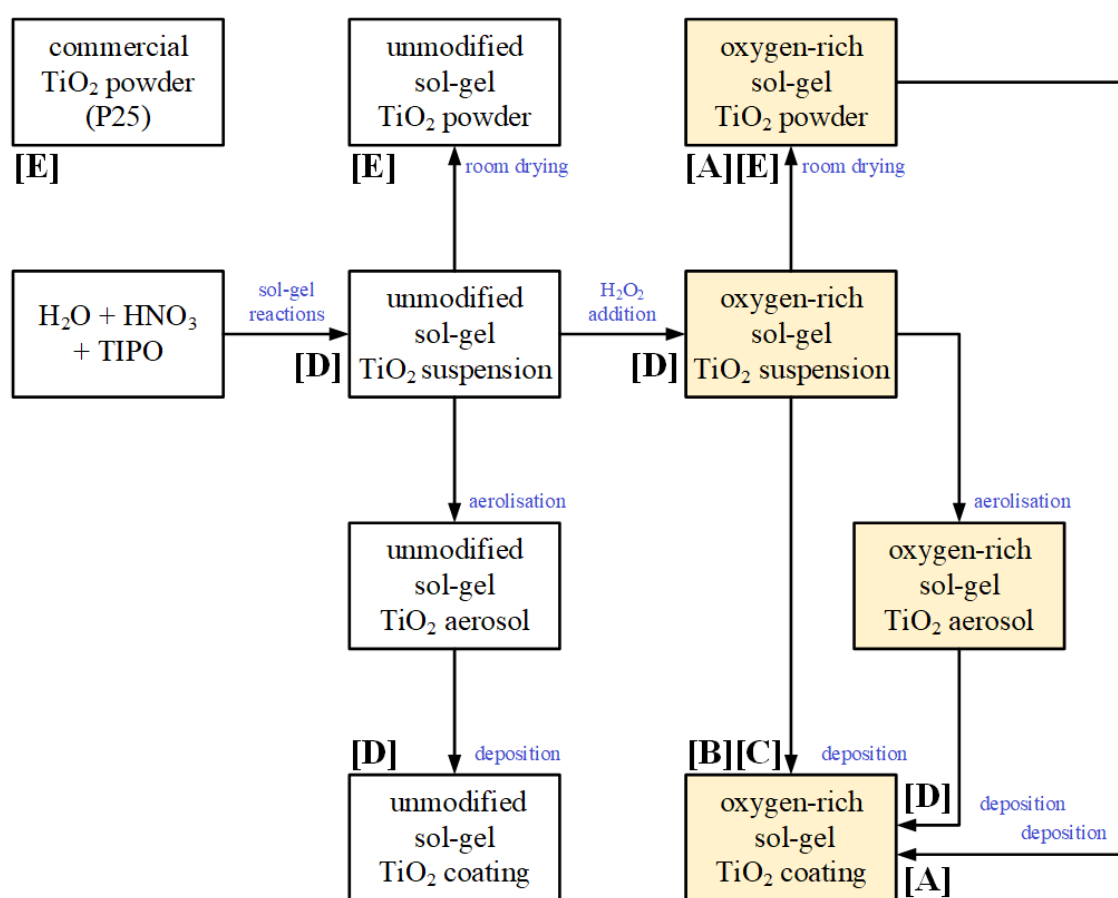


Figure 4 Thematic correlation between the papers that constitute the scientific achievement. Coloured blocks denote TiO_2 materials modified with H_2O_2 , and white blocks represent TiO_2 without H_2O_2 modification and commercial P25 powder. Process flow labels indicate the transformations occurring between each step. Citations are included to specify which papers studied each material type.

4.1 SOL-GEL SYNTHESIS

TiO₂ was synthesised via single-pot sol-gel method (Figure 5). Titanium dioxide was formed from titanium(IV) isopropoxide (TIPO) used as a precursor, distilled water and nitric acid. The sol-gel reactions result in formation of metal-oxygen network with residual isopropoxide groups or partially hydrolysed species. Upon the contact of H₂O₂, oxygen-rich groups are formed on the surface of the titania [21,23]. The colour of reaction mixture changes instantly and ranges from red, through orange to yellow depending on the type of the peroxo groups (linear Ti-OOH, Ti-O-O-Ti, and triangular TiO₂), superoxo groups and their concentrations [21]. The colour of the dried H₂O₂-treated TiO₂ appear yellow to the naked eye. In other research oxygen-rich groups serve most commonly as an essential intermediate step to achieve hydrated crystalline TiO₂ phases which is obtained through heat treatment which transform oxygen-rich group to hydroxy groups [24]. In this research, resigning from thermal treatment aimed to preserve oxygen-rich groups (possible issue 2.2.1).

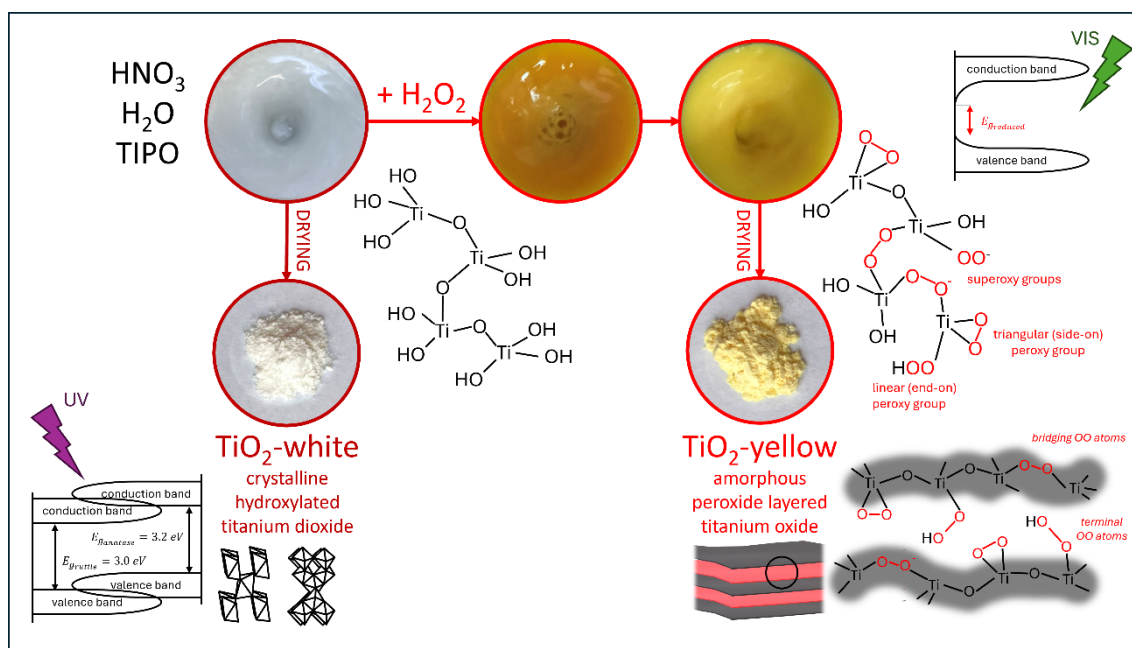


Figure 5 Scheme of sol-gel synthesis of H₂O₂-modified and unmodified TiO₂ supplemented with a graphic illustration depicting the differences in the chemical composition [E]

In this thesis, the same recipe is used to synthesize:

- powders (oxygen-rich TiO₂ [A, E] and unmodified [E])
- suspensions (oxygen-rich TiO₂ [B,C,D] and unmodified [D]).

4.2 LOW-PRESSURE COLD SPRAYING

The coatings were deposited on the aluminium AW-1050A H14/H24 (min. 99.5 wt.% of Al) substrates with dimensions of 20 mm × 20 mm × 4 mm. Aluminium naturally passivates (Al_2O_3) in humid or aqueous environments which provides water and corrosion resistance. Compared to other corrosion-resistant metals, such as stainless steel or titanium, aluminium is significantly more affordable. Its low density (approximately one-third that of steel) makes it exceptionally lightweight without compromising structural integrity. This property is particularly beneficial in complex assemblies where minimizing weight is crucial, such as in aerospace, automotive, architectural applications or photocatalytic reactors with replaceable inserts. Aluminium is also a highly ductile metal, allowing it to be easily shaped, textured, or micro-patterned. During cold spraying, aluminium enhances coating build-up due to its impact characteristics [34,40]. Roughening provides an additional point of contact with surface and valleys that facilitate the anchoring of particles due to shear instabilities [32,34,40]. Typical techniques for topography modification include grit and sand blasting, grinding, and laser texturing [39]. In this thesis, before the LPSC process, all substrates were grit-blasted using corundum (Al_2O_3 , mesh 45).

All coatings are prepared using a Dymet 413 unit (Obninsk Center for Powder Spraying, Obninsk, Russia) coupled with a computer-controlled manipulator (BZT Maschinenbau GmbH, Leopoldshöhe, Germany). Dymet systems are considered a benchmark for low-pressure cold spraying [39,52]. The integration with a computer-controlled manipulator provides precise movement and positioning, ensuring operator safety, uniform coating thickness, and customizable layer designs. Additionally, it enables flexible coating patterns and efficient application on complex geometries.

Only one nozzle design is used throughout the study. The feedstock material is delivered to the nozzle (internal feed system, Figure 6a and Figure 8a) or bypassing the nozzle (external feed system, Figure 7a and Figure 8a).

4.2.1 POWDER FEED LPCS SYSTEM [A]

Dymet system is equipped with a standard vibrational hopper feeder designed for metallic powders with particles ranging from 5-50 μm [37,52]. In the case of low-density soft-phase powders with wide particle size distribution, the vibrations cause powder tamping

and clogging of the hopper outlet [39](possible issue 2.2.3). That is why instead of a hopper, an aerosol powder feeder RBG 1000 SD (Palas GmbH, Karlsruhe, Germany) was applied [53]. According to producer information, the particle size range is larger (0.1-100 μm) [53]. The powder is filled into a feedstock powder compartment whose size is controlled by the programmable movement of the piston. The powder is delivered into the dispersion head with a rotating precision brush. Then due to the application of carrier gas (nitrogen, 0.1 MPa), the loose powder is transferred to the dispersion unit outlet.

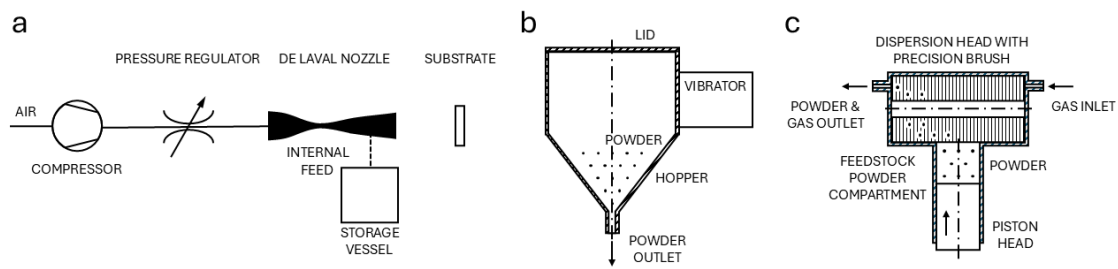


Figure 6 (a) Scheme of low-pressure cold spraying system with powder feeder, (b) with a detailed view of the standard hopper feeder, and (c) Palas aerosol generator based on producer data [53]

4.2.2 SUSPENSION FEED LPCS SYSTEM [B,C]

Suspension spraying is an effective heat-protection technique. The liquid phase reduces thermal energy delivered to the particles by consuming it partially for evaporation. The system for suspension feed needs to be leakproof. Traditional syringe pumps are used in thermal spraying procedures [33]. For spraying of H_2O_2 -modified TiO_2 suspension, different construction was developed (Figure 7b,c). The carrier gas is supplied to the

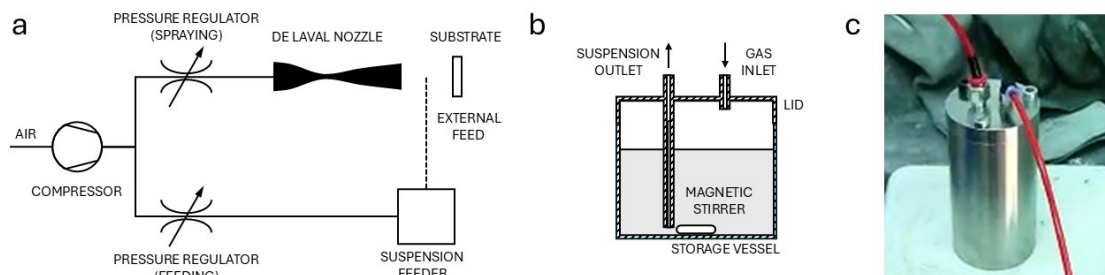


Figure 7 (a) Scheme of low-pressure cold spraying system with suspension feeder, (b) with a detailed view of the suspension feeder, and (c) the photograph of the suspension feeder on the magnetic stirrer

storage vessel and pushes the suspension. The suspension is homogenized by constant stirring. To enable proper stirrer operation, austenitic stainless steel (non-magnetic) was used for construction. Its corrosion resistance reduces vessel degradation in contact with H_2O_2 -containing substances. The important part of the storage vessel is the pressure relief valve, as the decomposition of H_2O_2 is exothermic which may lead to explosions.

The volume of the suspension delivered to the substrate is controlled by the gas pressure and the diameter of the feeder outlet. Small diameters cause nozzle clogging. Too high a feed rate may cause problems with the evaporation of the liquid part which is required for H_2O_2 -containing structures [B,C]. This is especially important for cold spraying in which the distance from the nozzle to the substrate is generally lower than for other thermal spraying techniques [33,35].

4.2.3 AEROSOL FEED LPCS SYSTEM [D]

The application of a non-continuous suspension feeding system facilitates the rapid evaporation of liquid. The most important effect of this research is that it may provide full evaporation of H_2O_2 -containing suspension. The construction of the atomizer was also developed for this research. It consists of a specially designed 3-D printed storage vessel and a vacuum generator mounted inside (Figure 8b,c) [54][F]. The suspension is supplied in a batch process and to provide homogeneity it is under continuous mixing with a magnetic stirrer. For aerosolization, gas flows through the vacuum generator which creates a negative pressure that draws the liquid from the chamber to the aerosol outlet. Then the aerosol of suspension is introduced either at the diverging section of the de Laval nozzle or externally in the middle of the distance between the nozzle end and the substrate material.

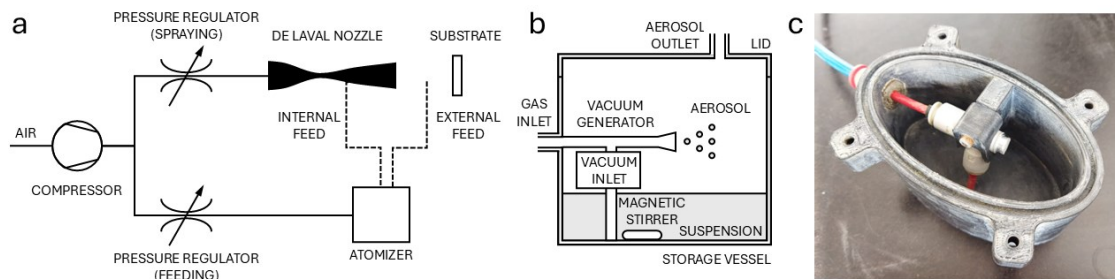


Figure 8 (a) Scheme of the low-pressure cold spraying system with suspension atomizer, (b) a with detailed view of the atomizer, and (c) the photograph of the atomizer with the lid removed [D]

4.2.4 SPRAYING PARAMETERS SUMMARY

To reach the various aims of research (Chapter 3), different combinations of spraying parameters were selected (Table 3).

Table 3 Compilation of spraying parameters

<p>[A] The modified spraying parameters:</p> <ul style="list-style-type: none"> – carrier gas temperature (200, 600 °C). <p>Other spraying parameters:</p> <ul style="list-style-type: none"> – feedstock material: oxygen-rich TiO₂ powder – carrier gas: type: air, pressure: 0.5 MPa, – nozzle: circular with 2.5 mm throat and 5 mm outlet, – manipulator: traverse speed: 2.5 mm/s, stand-off distance: 10 mm, scanning step: 2 mm, – feeding: feeding rate: 61 g/h, powder feed: internal.
<p>[B] The modified spraying parameters:</p> <ul style="list-style-type: none"> – scanning step (1, 2, 3 mm), – standoff distance (10, 20, 30 mm), – traverse speed (75, 150, 300 mm/min) – temperature of carrier gas (400 and 600 °C). <p>Other spraying parameters:</p> <ul style="list-style-type: none"> – feedstock material: oxygen-rich TiO₂ suspension – carrier gas: type: air, pressure: 0.5 MPa, – nozzle: circular with 2.5 mm throat and 5 mm outlet, – feeding: feeding rate: 28.6 µL/s, suspension feed: external, in the middle of standoff distance, skewed 20° relative to nozzle axis.
<p>[C] The modified spraying parameters:</p> <ul style="list-style-type: none"> – scanning step (2, 3, 4 mm) – traverse speed (150, 300, 450 mm/min) – temperature of carrier gas (200, 400, 600 °C). <p>Other spraying parameters:</p> <ul style="list-style-type: none"> – feedstock material: oxygen-rich TiO₂ suspension – carrier gas: type: air, pressure: 0.5 MPa, – nozzle: circular with 2.5 mm throat and 5 mm outlet,

-
- manipulator: standoff distance: 30 mm, scanning step: 2 mm,
 - feeding: feeding rate: 28.6 $\mu\text{L/s}$, suspension feed: external, in the middle of standoff distance, skewed 20° relative to nozzle axis.
-

[D] The modified spraying parameters:

- suspension feed (downstream injection or external injection (in the middle of standoff distance, skewed 20° relative to nozzle axis)).
- feedstock material (oxygen-rich TiO_2 **aerosol of suspension** or unmodified TiO_2 **aerosol of suspension**).

Other spraying parameters:

- carrier gas: type: air, pressure: 0.5 MPa,
 - nozzle: circular with 2.5 mm throat and 5 mm outlet,
 - manipulator: standoff distance: 10 and 30 mm, scanning step: 2 mm, traverse speed: 300 mm/min, temperature of carrier gas: 600 °C,
 - feeding: feeding rate: 28.6 $\mu\text{L/s}$, suspension feed: internal, and external, in the middle of standoff distance, skewed 20° relative to nozzle axis.
-

[E] No coating²

² No coatings. The paper provides an in-depth analysis of the powders utilized in [A].

4.3 CHARACTERIZATION METHODS

This section presents the most relevant techniques for the examination of H₂O₂-modified TiO₂ powders, suspensions and coatings.

4.3.1 X-RAY DIFFRACTION [A,D,E]

X-ray diffraction is widely used for the investigation of phase composition, degree of crystallinity, and structural defects. In this thesis, it was primarily used to detect whether LPCS deposition caused phase transition from amorphous phase to anatase [32].

4.3.2 RAMAN [A,B,C,D,E] AND INFRARED SPECTROSCOPY [E]

Raman spectroscopy confirms phase composition changes and recognises oxygen-rich groups. Raman bands are assigned based on the literature review which is presented in [A]. Infrared spectroscopy is more specific for distinguishing their different geometries, including triangular or linear groups [11].

4.3.3 ELECTRON PARAMAGNETIC RESONANCE SPECTROSCOPY [C,E]

Interaction of TiO₂ with H₂O₂ causes the formation of paramagnetic defects. In this research, electron paramagnetic resonance spectroscopy excluded the presence of most popularly detected oxygen vacancies and Ti³⁺ defects [11,21] and enabled the identification of superoxide radical anion (O₂⁻) in the powders [C] and coatings [E] before and after catalytic activity tests.

4.3.4 X-RAY PHOTOELECTRON SPECTROSCOPY [E]

X-ray photoelectron spectroscopy confirms primarily the oxidation states of titanium (Ti⁴⁺) and provides information about Ti–O bonding, including the existence of surface hydroxy groups, oxygen-rich groups, and adsorbed water [11,21].

4.3.5 SURFACE CHARGE [E]

The point of zero charge (pH_{PZC}) is critical for understanding the adsorption processes of pollutants on the catalyst surface. The drift method [55] is a simple and inexpensive approach to assess at which pH negative and positive charges are equal. This means that at pH lower than pH_{PZC} the positively charged surface of TiO₂ attracts anions (including

condo red), while at pH higher than pH_{PZC} negatively charged surface attracts cations (such as methylene blue) [11].

4.3.6 SEDIMENTATION TEST [D]

To maintain constant feed, homogeneity, and prevent defects in the coating, the stability and settling behaviour of suspension should be examined. To avoid interactions between glass and titanium precursors, polymeric cylinders are used instead of standard glass cylinders for the sedimentation test.

4.3.7 DIFFUSE REFLECTANCE SPECTROSCOPY [A,B,C,D,E]

The Kubelka-Munk function is used to determine the optical bandgap width, which represents the energy gap between the valence and conduction bands of semiconductors. Additionally, the method provides information about localized electronic midgap states which are caused by the disorder and defects and may be observed as the Urbach tail [56]. Thanks to sub-bandgap absorption, which allows absorbing photons of energy lower than the bandgap, H_2O_2 -modified TiO_2 is a promising material for visible-light applications.

The reflectance measurement is, however, influenced by multiple factors, including surface characteristics [57]. This aspect was used in [C] where bandgap energy underestimation in coatings with the same chemical characteristics resulted from the presence of coating discontinuities. Detection of defective coatings facilitated the optimisation of spraying parameters for the development of crack-free surfaces.

4.3.8 TRANSMISSION ELECTRON MICROSCOPY [E]

Electron microscopy provides information about the morphology of the powders. Selected-area electron diffraction offers observation of diffraction patterns at different orientations directly on the transmission electron images which confirms the presence of crystalline phases at atomic level. This technique is particularly useful for heterogeneous materials and nanostructures of low-crystallinity.

4.3.9 SURFACE FEATURES [A,B,C]

There are two technical approaches to determining the specific surface area of TiO_2 coatings: detaching the coating or measuring it in situ without detachment. The first option is impractical, as TiO_2 coatings lack sufficient mechanical integrity to be removed

without damaging their structure. In the second option, mercury porosimetry or nitrogen adsorption to access specific surface area are limited to detecting only open porosity. Additionally, such analysis relies on comparing the mass of the sample and the substrate. For thin coatings with low mass (on the order of a few milligrams), this can lead to significant measurement errors due to the small mass difference.

To overcome these challenges, optical image profilometry is used. This optical technique generates a three-dimensional surface profile by scanning multiple focal planes along the z-axis, allowing for the calculation of surface area and roughness. Its resolution is limited by the nature of light, preventing the detection of features smaller than approximately 200 nm, as well as complex topologies such as step edges and undercuts [17]. But optical image profilometry (as used in [B,C]) is more suitable for analysing thin coatings compared to tactile profilometry (as used in [A]), which may damage brittle surfaces.

4.3.10 SURFACE AND CROSS-SECTION IMAGING [A,B,C,D]

The morphology of surface and cross sections is investigated using a scanning electron microscope equipped with secondary electrons and backscattered electrons detectors. The limitation of backscatter images includes low contrast (because of the relatively close atomic number of titanium ($Z=22$) and aluminium ($Z=13$)) and reduced resolution due to image distortion caused by the lack of conductivity of TiO_2 layers. To reduce charging without carbon or gold sputtering, the low vacuum mode is used.

4.3.11 CROSSCUT TEST [D]

To assess the adhesion strength of thermal sprayed coatings, the standard method typically used is the pull-off test (ASTM C633). However, for very thin and smooth coatings, the scratch test (ASTM C1624) is often employed. In our study, the coatings were too thin (with a thickness below $380\text{ }\mu\text{m}$) to apply the ASTM C633 standard and too rough to utilize the ASTM C1624 standard. As a result, the adhesion was assessed strength using the cross-cut method, in accordance with the ISO 2409 standard, which is suitable for coatings with the characteristics observed in this study.

4.3.12 STATISTICAL ANALYSIS [C]

Photocatalytic activity testing is time-consuming. Taguchi's orthogonal design approach reduces the number of experimental test runs. The method was developed for the industry

but currently is applied also scientific research of various processes, including coating preparation processes using thermal spraying [48]. This means that the photocatalytic activity test in [C] has been performed only for selected samples.

4.3.13 MB DEGRADATION [A,C,E]

Dyes degradation test coupled with UV-VIS spectroscopy is a simple, cheap, reliable and reproducible mean to assess real-time photocatalytic activity. Several standardised methods for dye degradation in aqueous solution using UV light have been developed, including ISO 10678:2010, and the newest ISO 10678:2024 standards. Visible light can, however, excite dye molecules (possible issue 2.1.1). To exclude dye sensitization, it is essential to use an irradiation source with wavelengths shorter than the maximum absorption of methylene blue (600–700 nm, Figure 9a). Consequently, a source with maximum emission within the range of 420–500 nm was used (Figure 9b) or an appropriate cut-off filter (Figure 9c).

The spectroscopic method is based on measuring the decreasing concentration of MB. To exclude the effect of dye adsorption (possible issue 2.1.3), total organic carbon measurements were carried out to provide a quantitative value for degraded dye [E].

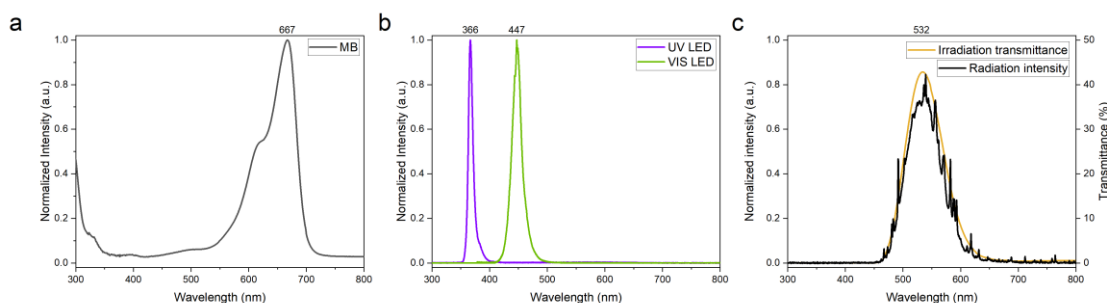


Figure 9 (a) UV-Vis absorption spectrum of methylene blue and spectral characteristics of (b) UV and Vis diodes [E] and (c) Xe lamp with the UV cut-off filter [A,C]

4.3.14 BACTERIA KILLING [E]

The bactericidal effects of TiO₂ against both Gram-positive (*Enterococcus faecalis*) and Gram-negative (*Escherichia coli*) bacteria were evaluated under solar-like illumination and in darkness to observe dose-dependent effects. Bacterial viability was quantified by counting colony-forming units on agar plates. Although a cooling system was used, the XENON lamp often caused a temperature rise, potentially influencing bacterial viability.

Additionally, the XENON lamp emitted a mixture of UV and visible light, complicating the interpretation of light-specific effects. No standard substances active under visible light or in darkness were used for comparison of antimicrobial activity as there are currently none popularly used.

4.3.15 LIST OF CHARACTERIZATION METHODS

The overview of all characterization methods is presented in Table 4.

Table 4 Compilation of methods used for characterization of prepared materials

[A]	Particle size (particle size analysis), surface topography and cross-section morphology (scanning electron microscopy), surface roughness (tactile profilometry), phase composition (X-ray diffraction), chemical composition (Raman spectroscopy), optical bandgap width (diffuse reflectance spectroscopy), MB degradation (UV-Vis spectroscopy)
[B]	Surface topography and cross-section morphology (scanning electron microscopy), surface roughness (optical profilometry), chemical composition (Raman spectroscopy)
[C]	Surface topography and cross-section morphology (scanning electron microscopy), surface roughness (optical profilometer), chemical composition (Raman, electron paramagnetic resonance spectroscopy), MB degradation (UV-Vis spectroscopy)
[D]	Particle aggregation in feedstock suspensions (particle size analysis), suspension stability (sedimentation test), surface topography and cross-section morphology (scanning electron microscopy), phase composition (X-ray diffraction), chemical composition (Raman spectroscopy), mechanical integrity (cross-cut test)
[E]	Phase composition (X-ray diffraction), morphology (transmission electron microscopy), particle size (particle size analysis), thermal stability of oxygen-rich groups (differential scanning calorimetry and thermogravimetric analysis), optical bandgap width (diffuse reflectance spectroscopy), chemical composition (X-ray photoelectron, electron paramagnetic resonance, infrared, and Raman spectroscopy), net charge (pH_{PZC}), MB degradation (UV-Vis spectroscopy, total organic carbon), bacteria-killing (colony forming unit assay)

5 KEY FINDINGS

The concluding remarks include the investigated results of TiO₂ modification with H₂O₂, the development of low-pressure cold spraying strategies for the deposition of oxygen-rich TiO₂ and careful examination of the influence of delivered thermal energy on deposited sol-gel materials.

5.1 INFLUENCE OF H₂O₂ MODIFICATION

In this thesis, different impacts of TiO₂ modification with H₂O₂ on its structure and activity are observed. The effects of oxygen-rich groups include:

- Narrowing the optical bandgap energy of the TiO₂ by forming midgap states (Urbach tail) so TiO₂ can be potentially activated by visible light.
- Blocking the formation of 3D structures (during bottom-up synthesis) which inhibits crystallization and may lead to the formation of the layered structure (2D).
- Improving the adsorption process through the formation of an oppositely charged TiO₂ surface, which attracts pollution.
- Creating an oxidative environment for the oxidation of pollutants or bacteria (ROS analysis) which provides the activity in the darkness.
- Depending on the type, promoting short-term activity (superoxo groups) or long-term activity (peroxo groups).

5.2 INNOVATIVE APPROACHES TO OXYGEN-RICH COATINGS

The other key aspect of this thesis is to provide the procedure for oxygen-rich coating formation using low-pressure cold spraying with feedstock in various forms.

- Spraying of sol-gel powder is possible without an inert atmosphere or vacuum. Changing spraying parameters may reduce unwanted phase transformations and enable the preservation of oxygen-rich groups (possible issue 2.2.1). Application of appropriate feeder excludes clogging of feeding system (possible issue 2.2.3)
- Spraying of sol-gel suspension may be beneficial. The liquid phase in the wet gel consumes excessive thermal energy on liquid evaporation so oxygen-rich groups can be preserved (possible issue 2.2.1)
- Spraying of aerosolised sol-gel suspension may improve liquid evaporation which combats coating disintegration caused by trapping residual H₂O₂ in the coating

(possible issue 2.3.2), providing coating homogeneity and presence of oxygen-rich groups (possible issue 2.2.1).

5.3 THERMAL DRYING OF SOL-GEL MATERIAL BY LPCS

The spraying temperature does indeed influence TiO_2 particle bonding and the resulting coating microstructure. Discussion of the thermal energy effects on coatings sprayed from sol-gel materials relies on liquid evaporation [B].

The suggested mechanism (Figure 10) was developed because wet gels differ from the most commonly used particle-solvent systems. The sol-gel particle consists of a condensed core and a partially condensed shell which behave differently in the gas stream. The dense particles result in dense coating with a well-developed profile while the porous shells can be preserved to form multi-tier roughness on generally flatter coatings.

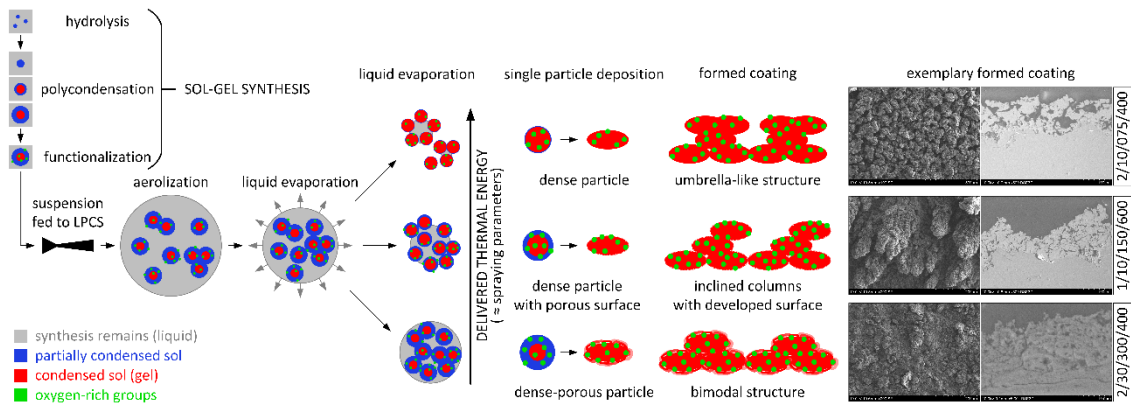


Figure 10 Scheme of the proposed mechanism for suspension low-pressure cold spraying of oxygen-rich TiO_2 [B]

Insufficient thermal energy in coatings sprayed from aerosolized suspension [D] resulted in pancake-like coatings, while higher energy improved particle bonding and coating density. Coatings applied using the internal feed system exhibited uniform bonding due to the rapid evaporation of the liquid phase, causing mechanical interlocking of the particles. In contrast, the external feed system produced thicker coatings, which reduced the influence of the underlying grit-blasting texture. While increased thermal energy promoted densification, it also led to the formation of network-like cracks within the coatings.

5.4 MAIN CONCLUSIONS

The major results can be summed up with regard to each study:

Table 5 Compilation of main findings

[A] The oxygen-rich TiO_2 powder produced using the aqueous peroxo-titania sol-gel route without thermal treatment is characterized by narrowed bandgap width through the formation of midgap states (2.2 eV) and lack of powder annealing sustains it in an amorphous state.

The characteristic of oxygen-rich TiO_2 coatings produced from oxygen-rich TiO_2 powder using low-pressure cold spray depends on carrier gas temperature:

- With 600 °C: 25–50 μm thick, porous anatase coating, rough at the surface, weighting 35 ± 9 mg, with bandgap energy 3.1 eV was formed.
- With 200 °C: 2–3 μm thin, discontinuous amorphous coating weighing less than 1 mg with bandgap energy 2.8 eV was formed.

Both coatings exhibit visible light activity in methylene blue degradation (17 % and 3.1 % degradation in 6 h for coating sprayed using carrier gas preheated to 600 °C and 200 °C).

Feedstock powder changes upon spraying. Structure crystallization and only partial preservation of oxygen-rich groups in coatings are observed.

[B] Application of liquid feedstock for spraying oxygen-rich TiO_2 coatings using low-pressure cold spray reduces the material changes upon spraying:

- In most of the coatings, the oxygen-rich structure is preserved.
- For coatings sprayed with the scanning step of 1 mm, the standoff distance of 10 mm, the traverse speed of 150 mm/min and the carrier gas temperature of 600 °C, delivered thermal energy-induced partial crystallization but despite this oxygen-rich groups are partially preserved.

50 μm thick coatings can be deposited in a single pass.

The most uniform coatings are produced using the standoff distance of 30 mm.

Application of sol-gel materials (consisting of partially condensed sol and condensed gel) produces complex structures after deposition.

The residues containing H_2O_2 which are trapped in the coating cause coating disintegration shortly after coating deposition due to H_2O_2 -containing bubble collapse.

[C] The spraying of oxygen-rich TiO_2 suspension with parameters preserving oxygen-rich amorphous structure selected based on **[B]** is reproducible and provides the same chemical and optical properties of coating as of powders **[A]**.

Experimenting with spraying oxygen-rich TiO_2 coatings according to plan (Taguchi method) provides:

- The process parameters for spraying optimal E_g and SA values (the scanning step of 2 mm, the traverse speed of 150 mm/min and the carrier gas temperature of 600 °C).
- ANOVA showed that the most influential spraying parameter is carrier gas temperature with an effect of 53.81 % and 56.62 % on the E_g and SA values, respectively. The least significant parameter is traverse speed with a contribution of 15.69 % on E_g .

The coating prepared with optimal parameters (thickness 5–25 μm , mass 3.4 mg) possesses the expected characteristics (E_g and SA of the optimal coating were 2.39 eV and 2 553 369 μm^2 , respectively). It exhibits visible light activity (14.1 % degradation in 6 h).

The residues containing H_2O_2 which are trapped in the coating cause coating disintegration shortly after coating deposition due to H_2O_2 -containing bubble collapse.

[D] The spraying of aerosolized oxygen-rich TiO_2 suspension causes full evaporation of H_2O_2 -containing synthesis residues which preserve the structure of coatings.

The oxygen-rich TiO_2 coatings produced from oxygen-rich TiO_2 aerosolised suspension using low-pressure cold spray retain an oxygen-rich structure and form thick coatings (20 to 80 μm).

-
- The internal feed enhances liquid evaporation and causes loosely bound particles to be observed on the coating similar to [A].
 - The external feed provides surface uniformity.

Coating deposition in a single pass contributes to maintaining amorphous structure, while 3 passes cause partial crystallisation to anatase.

The initial characteristics of suspension changed with respect to mixing times of suspension before and after modification:

- The addition of H_2O_2 to TiO_2 suspension mixed for 48 h causes the formation of a jelly-like structure, not possible to be aerosolised.
- Prolonged mixing after the addition of H_2O_2 causes the decomposition of oxygen-rich groups.

[E] More detailed research on oxygen-rich TiO_2 powder, as in [A], shows that:

- Chemical and structural changes in the titania composition are introduced by the incorporation of additional oxygen in the whole volume.
- Modifications narrows the bandgap width through the formation of midgap states (2.2 eV).
- Lack of powder annealing sustains the produced powder in an amorphous state, which can be used for low-temperature low-energy deposition techniques (such as low-pressure cold spray described in [A-D]).

H_2O_2 -modified TiO_2 showed visible light photo-activity and dark activity for methylene blue oxidation and bacteria killing:

- The adsorption is facilitated by the low pH_{pzc} of the material (3.2).
 - The visible light activity is caused by photocatalytic oxidation and photocatalysis leading to degradation of 75% of MB in 8 h in zero-order kinetics, $k = 0.027 \text{ (mg/L) min}^{-1}$, and bacteria ($\text{MBC}_{\text{enterococcus}} = 750 \text{ }\mu\text{g/mL}$, $\text{MBC}_{\text{coli}} = 375 \text{ }\mu\text{g/mL}$ (6 \log_{10} CFU/mL removal)).
 - Dark activity resulted from the unique chemical composition of the studied material (presence of superoxo groups) which enabled the oxidation of pollutants degrading 36% of MB in 8 h in zero-order kinetics, $k = 0.014 \text{ (mg/L) min}^{-1}$, and bacteria ($\text{MBC}_{\text{enterococcus}} > 1500 \text{ }\mu\text{g/mL}$, $\text{MBC}_{\text{coli}} = 1500 \text{ }\mu\text{g/mL}$ (6 \log_{10} CFU/mL removal)).
-

6 OUTLOOK

Modern photocatalytic materials are meant to provide multi-faceted activity. The presented research can be extended with new types of pollution including antibiotics, microplastics or personal care products. Additionally, the degradation of air pollution may be addressed, so that an integrated environmental strategy can be developed.

Because in dark degradation processes, oxygen-rich groups were partially consumed, the regeneration strategies with H_2O_2 or laser may be investigated. Such procedures may be studied particularly for coatings because the application of a supported catalyst offers easy separation.

Electron paramagnetic resonance spectroscopy may be employed for in-situ detection of free radicals and reactive oxygen species ($\bullet\text{OH}$, $\text{O}_2^{\bullet-}$, $\bullet\text{OOH}$) during degradation reactions, which are popular for the specification of degradation pathways [18][19].

Microstructures obtained from low pressure cold spraying of aerosolised suspensions may be promising for depositing other materials. For instance, bone-like structures obtained in [E] can be beneficial in the process of formation of hydroxyapatite coatings.

In-flight particle characteristics can be studied more extensively, too. Information about the exact temperature and velocity could improve the deposition efficiency of powders, suspensions and aerosolised suspensions, and provide data to understand the spraying of partially condensed sol-gel materials. Computational fluid dynamics modelling would require more detailed materials information which can be accessed from density functional theory.

7 REFERENCES

- [1] EEA, Europe ' s state of water 2024 The need for improved water resilience, 2024. <https://doi.org/10.2800/02236>.
- [2] K.K. Kesari et al., Wastewater Treatment and Reuse: a Review of its Applications and Health Implications, Water, Air, Soil Pollut. (2021). <https://doi.org/10.1007/s11270-021-05154-8>.
- [3] R. Rashid et al., A state-of-the-art review on wastewater treatment techniques: the effectiveness of adsorption method, Environ. Sci. Pollut. Res. (2021). <https://doi.org/10.1007/s11356-021-12395-x>.
- [4] S. Malato et al., Decontamination and disinfection of water by solar photocatalysis: Recent overview and trends, Catal. Today (2009). <https://doi.org/10.1016/j.cattod.2009.06.018>.
- [5] W. Hamd et al., Recent Advances in Photocatalytic Removal of Microplastics: Mechanisms, Kinetic Degradation, and Reactor Design, Front. Mar. Sci. (2022). <https://doi.org/10.3389/fmars.2022.885614>.
- [6] S. Feijoo et al., Generation of oxidative radicals by advanced oxidation processes (AOPs) in wastewater treatment: a mechanistic, environmental and economic review, Springer Netherlands, 2023. <https://doi.org/10.1007/s11157-023-09645-4>.
- [7] M.P. Rayaroth et al., Advanced oxidation processes (AOPs) based wastewater treatment - unexpected nitration side reactions - a serious environmental issue: A review, Chem. Eng. J. (2022). <https://doi.org/10.1016/j.cej.2021.133002>.
- [8] P. Kumari et al., Advanced Oxidation Process: A remediation technique for organic and non-biodegradable pollutant, Results in Surfaces and Interfaces (2023). <https://doi.org/10.1016/j.rsurfi.2023.100122>.
- [9] M.F. La Russa et al., Multifunctional TiO₂ coatings for Cultural Heritage, Prog. Org. Coatings (2012). <https://doi.org/10.1016/j.porgcoat.2011.12.008>.
- [10] K.L. Arun et al., A Comprehensive Review on Various Ceramic Nanomaterial Coatings Over Metallic Substrates: Applications, Challenges and Future Trends, Springer International Publishing, 2023. <https://doi.org/10.1007/s40735-022-00717-6>.
- [11] J. Seo et al., Visible light-photosensitized oxidation of organic pollutants using amorphous peroxotitania, Appl. Catal. B Environ. (2018). <https://doi.org/10.1016/j.apcatb.2017.12.009>.
- [12] K.P. Sundar et al., Progression of Photocatalytic reactors and it's comparison: A Review, Chem. Eng. Res. Des. (2020). <https://doi.org/10.1016/j.cherd.2019.11.035>.
- [13] W. Zhang et al., Visible-Light Responsive TiO₂ -Based Materials for Efficient Solar Energy Utilization, Adv. Energy Mater. (2021). <https://doi.org/10.1002/aenm.202003303>.
- [14] M. Dell'Edera et al., Photocatalytic TiO₂-based coatings for environmental applications, Catal. Today (2021). <https://doi.org/10.1016/j.cattod.2021.04.023>.
- [15] J.Y. Piquemal et al., Preparation of materials in the presence of hydrogen peroxide: From discrete or “zero-dimensional” objects to bulk materials, Dalt. Trans. (2013). <https://doi.org/10.1039/c2dt31660a>.
- [16] M. Janczarek et al., Defective Dopant-Free TiO₂ as an Efficient Visible Light-Active Photocatalyst, Catalysts (2021). <https://doi.org/10.3390/catal11080978>.
- [17] D. Wiedmer, TiO₂ dark catalysis in biomedical applications, University of Oslo, 2017.
- [18] C.J. Querebillo, A Review on Nano Ti-Based Oxides for Dark and Photocatalysis: From Photoinduced Processes to Bioimplant Applications, Nanomaterials (2023). <https://doi.org/10.3390/nano13060982>.
- [19] D. Wiedmer, TiO₂ dark catalysis in biomedical applications, University of Oslo, 2017.
- [20] P. Tengvall et al., Bactericidal properties of a titanium-peroxy gel obtained from metallic titanium and hydrogen peroxide, J. Biomed. Mater. Res. (1990). <https://doi.org/10.1002/jbm.820240305>.
- [21] J.W. Lee et al., Facile synthesis of amorphous Ti-peroxo complex for photocatalytic activity under

- visible-light irradiation, *J. Clean. Prod.* (2019). <https://doi.org/10.1016/j.jclepro.2019.118013>.
- [22] X. Kong et al., Ti-O-O coordination bond caused visible light photocatalytic property of layered titanium oxide, *Sci. Rep.* (2016). <https://doi.org/10.1038/srep29049>.
- [23] K. Yaemsunthorn et al., Yellow TiO₂ from titanium peroxo complexes: Verification of the visible light activity and a rational enhancement of its photocatalytic efficiency, *J. Environ. Chem. Eng.* (2023). <https://doi.org/10.1016/j.jece.2023.111520>.
- [24] C. Randorn et al., Synthesis of visible-light-activated yellow amorphous TiO₂ photocatalyst, *Int. J. Photoenergy* (2008). <https://doi.org/10.1155/2008/426872>.
- [25] L.D. Sánchez et al., TiO₂ suspension exposed to H₂O₂ in ambient light or darkness: Degradation of methylene blue and EPR evidence for radical oxygen species, *Appl. Catal. B Environ.* (2013). <https://doi.org/10.1016/j.apcatb.2013.05.017>.
- [26] S. Horikoshi et al., Can the photocatalyst TiO₂ be incorporated into a wastewater treatment method? Background and prospects, *Catal. Today* (2020). <https://doi.org/10.1016/j.cattod.2018.10.020>.
- [27] K. Abdul Razak et al., Factors of Controlling the Formation of Titanium Dioxide (TiO₂) Synthesized using Sol-gel Method – A Short Review, *J. Phys. Conf. Ser.* (2022). <https://doi.org/10.1088/1742-6596/2169/1/012018>.
- [28] sol-gel process, in: *IUPAC Compend. Chem. Terminol.*, International Union of Pure and Applied Chemistry (IUPAC), Research Triangle Park, NC, 2014. <https://doi.org/10.1351/goldbook.ST07151>.
- [29] D. Bokov et al., Nanomaterial by Sol-Gel Method: Synthesis and Application, *Adv. Mater. Sci. Eng.* (2021). <https://doi.org/10.1155/2021/5102014>.
- [30] I.P.A.F. Souza et al., Optimization of thermal conditions of sol-gel method for synthesis of TiO₂ using RSM and its influence on photodegradation of tartrazine yellow dye, *J. Environ. Chem. Eng.* (2021). <https://doi.org/10.1016/j.jece.2020.104753>.
- [31] P.L. Fauchais et al., *Thermal Spray Fundamentals*, 2014. <https://doi.org/10.1007/978-0-387-68991-3>.
- [32] A. Baszczuk et al., Low-Temperature Transformation of Amorphous Sol–Gel TiO₂ Powder to Anatase During Cold Spray Deposition, *J. Therm. Spray Technol.* (2018). <https://doi.org/10.1007/s11666-018-0769-0>.
- [33] L. Pawlowski, Suspension and solution thermal spray coatings, *Surf. Coatings Technol.* (2009). <https://doi.org/10.1016/j.surfcoat.2009.03.005>.
- [34] J.O. Kliemann et al., Formation of cold-sprayed ceramic titanium dioxide layers on metal surfaces, *J. Therm. Spray Technol.* (2011). <https://doi.org/10.1007/s11666-010-9563-3>.
- [35] G. Kubicki et al., Microstructure and Properties of Hydroxyapatite Coatings Made by Aerosol Cold Spraying–Sintering Technology, *Coatings* (2022). <https://doi.org/10.3390/coatings12040535>.
- [36] B. Tian et al., Flame sprayed V-doped TiO₂ nanoparticles with enhanced photocatalytic activity under visible light irradiation, *Chem. Eng. J.* (2009). <https://doi.org/10.1016/j.cej.2009.02.030>.
- [37] M. Winnicki, Advanced functional metal-ceramic and ceramic coatings deposited by low-pressure cold spraying: A review, *Coatings* (2021). <https://doi.org/10.3390/coatings11091044>.
- [38] S. An et al., Review of recent progress in the supersonic cold-spraying technique with solid particles and liquid suspensions, *Exp. Fluids* (2021). <https://doi.org/10.1007/s00348-021-03247-y>.
- [39] O. Tregenza et al., Air-based cold spray: An advanced additive manufacturing technique for functional and structural applications, *Int. J. Adv. Manuf. Technol.* (2025). <https://doi.org/10.1007/s00170-025-15022-y>.
- [40] A.M. Vilardell et al., Feasibility of using low pressure cold gas spray for the spraying of thick ceramic hydroxyapatite coatings, *Int. J. Appl. Ceram. Technol.* (2019). <https://doi.org/10.1111/ijac.13088>.
- [41] U.G. Akpan et al., Parameters affecting the photocatalytic degradation of dyes using TiO₂-based photocatalysts: A review, *J. Hazard. Mater.* (2009). <https://doi.org/10.1016/j.jhazmat.2009.05.039>.

- [42] K. Wang et al., P25 and its components - Electronic properties and photocatalytic activities, *Surfaces and Interfaces* (2022). <https://doi.org/10.1016/j.surfin.2022.102057>.
- [43] S. Sun et al., Amorphous TiO₂ nanostructures: Synthesis, fundamental properties and photocatalytic applications, *Catal. Sci. Technol.* (2019). <https://doi.org/10.1039/c9cy01020c>.
- [44] C. Random et al., Bleaching of Methylene Blue by Hydrated Titanium Dioxide, *ScienceAsia* (2004). <https://doi.org/10.2306/scienceasia1513-1874.2004.30.149>.
- [45] J. Zhang et al., Room temperature plasticity in amorphous SiO₂ and amorphous Al₂O₃: A computational and topological study, *Acta Mater.* (2023). <https://doi.org/10.1016/j.actamat.2023.119223>.
- [46] E. Enríquez et al., Effective Air-Spray Deposition of Thin Films Obtained by Sol-Gel Process onto Complex Pieces of Sanitary Ware, *J. Am. Ceram. Soc.* (2016). <https://doi.org/10.1111/jace.13967>.
- [47] G.S. Lin et al., Silica gel-coated silicon carbide layer deposited by atmospheric plasma spraying, *J. Taiwan Inst. Chem. Eng.* (2020). <https://doi.org/10.1016/j.jtice.2020.04.003>.
- [48] C. Pierlot et al., Design of experiments in thermal spraying: A review, *Surf. Coatings Technol.* (2008). <https://doi.org/10.1016/j.surfcoat.2008.04.031>.
- [49] A. Moridi et al., Cold spray coating: review of material systems and future perspectives, *Surf. Eng.* (2014). <https://doi.org/10.1179/1743294414Y.0000000270>.
- [50] M. Shahien et al., Controlling the coating microstructure on axial suspension plasma spray process, *Surf. Coatings Technol.* (2018). <https://doi.org/10.1016/j.surfcoat.2018.09.055>.
- [51] D.Y. Kim et al., Supersonic cold spraying for zeolitic metal-organic framework films, *Chem. Eng. J.* (2016). <https://doi.org/10.1016/j.cej.2016.03.029>.
- [52] M.F. Smith, Introduction to Cold Spray, High Press. Cold Spray (2020). <https://doi.org/10.31399/asm.tb.hpcspa.t54460001>.
- [53] Palas, RBG 1000 I, (n.d.). <https://www.palas.de/en/product/rbg1000i>.
- [54] W. Łapa et al., Investigation of aerosol droplets diameter generated in aerosol jet printing, *Mater. Sci. Pol.* (2022). <https://doi.org/10.2478/msp-2022-0046>.
- [55] G. Newcombe et al., Granular activated carbon: Importance of surface properties in the adsorption of naturally occurring organics, *Colloids Surfaces A Physicochem. Eng. Asp.* (1993). [https://doi.org/10.1016/0927-7757\(93\)80311-2](https://doi.org/10.1016/0927-7757(93)80311-2).
- [56] G.L.C. Rodrigues et al., Study of Structural and Optical Properties of Titanate Nanotubes with Erbium under Heat Treatment in Different Atmospheres, *Materials* (Basel). (2023). <https://doi.org/10.3390/ma16051842>.
- [57] A. Murphy, Band-gap determination from diffuse reflectance measurements of semiconductor films, and application to photoelectrochemical water-splitting, *Sol. Energy Mater. Sol. Cells* (2007). <https://doi.org/10.1016/j.solmat.2007.05.005>.

8 LIST OF TABLES AND FIGURES

Table 1	Compilation of metadata of publications	2
Table 2	Compilation of main aims	18
Table 3	Compilation of spraying parameters	24
Table 4	Compilation of methods used for characterization of prepared materials	30
Table 5	Compilation of main findings	33
Table 7	Compilation of metadata of other scientific articles	41
Table 8	Compilation of conference presentations	42
Figure 1	Scheme of the oxygen-rich groups [E]	7
Figure 2	Sol-gel route	8
Figure 3	Analysis of current literature on thermal spraying of sol-gel materials based on used energy source for spraying	9
Figure 4	Thematic correlation between the papers that constitute the scientific achievement. Coloured blocks denote TiO ₂ materials modified with H ₂ O ₂ , and white blocks represent TiO ₂ without H ₂ O ₂ modification and commercial P25 powder. Process flow labels indicate the transformations occurring between each step. Citations are included to specify which papers studied each material type.	19
Figure 5	Scheme of sol-gel synthesis of H ₂ O ₂ -modified and unmodified TiO ₂ supplemented with a graphic illustration depicting the differences in the chemical composition [E]	20
Figure 6	(a) Scheme of low-pressure cold spraying system with powder feeder, (b) with detailed view of the standard hopper feeder, and (c) Palas aerosol generator based on producer data [51]	22
Figure 7	(a) Scheme of low-pressure cold spraying system with suspension feeder, (b) with detailed view of the suspension feeder, and (c) the photograph of the suspension feeder on the magnetic stirrer	22
Figure 8	(a) Scheme of the low-pressure cold spraying system with suspension atomizer, (b) with detailed view of the atomizer, and (c) the photograph of the atomizer with the lid removed [D]	23
Figure 9	(a) UV-Vis absorption spectrum of methylene blue and spectral characteristics of (b) UV and Vis diodes [E] and (c) Xe lamp with the UV cut-off filter [A,C]	29
Figure 10	Scheme of the proposed mechanism for suspension low-pressure cold spraying of oxygen-rich TiO ₂ [B]	32

9 SCIENTIFIC ACHIEVEMENTS

9.1 SUMMARY OF SCIENTIFIC ACHIEVEMENTS

9.1.1 OTHER ARTICLES

The skills and techniques used to develop this work were also valuable in preparing 10 published and 2 currently proceeded scientific publications (Table 6).

Table 6 Compilation of metadata of other scientific articles

[1]	K. Płatek, L. Łatka, A. Gibas , A. Lewińska, M. Michalska, P. Sokołowski, Deposition of defect-rich titanium oxide coatings using Ar/H ₂ powered suspension plasma spraying, submitted for peer-review, 2025
[2]	A. Gibas , A. Baszczuk, M. Jasiorski, M. Winnicki, W. Seremak, Alloying of composite Cu-Al cold sprayed coatings by near-infrared radiation, submitted for peer-review, 2025
[3]	A. Szukalska, A. Żak, E. Chrzumnicka, A. Gibas , A. Baszczuk, J. Myśliwiec, Crystallization-driven tuneable lasing of perylene doped into the nematic liquid crystal, Giant, 2024, DOI: 10.1016/j.giant.2024.100279, IF: 5.4 (2023)
[4]	E. Kociołek-Balawejder, A. Gibas , A. Baszczuk, M. Jasiorski, I. Jacukowicz-Sobala, Transformation of CuO and Cu ₂ O particles into Cu _x S within the polymeric matrix of anion exchangers, and its structural and morphological implications, Reactive & Functional Polymers, 2023, DOI: 10.1016/j.reactfunctpolym.2023.105734, IF: 4.5 (2023)
[5]	M. Winnicki, A. Baszczuk, A. Gibas , M. Jasiorski, Experimental study on aluminium bronze coatings fabricated by low pressure cold spraying and subsequent heat treatment, Surface & Coatings Technology, 2023, DOI: 10.1016/j.surfcoat.2023.129260, IF: 5.3 (2023)
[6]	I. Jacukowicz-Sobala, A. Ciechanowska, E. Kociołek-Balawejder, A. Gibas , A. Zakrzewski, Photocatalytically-assisted oxidative adsorption of As(III) using sustainable multifunctional composite material – Cu ₂ O doped anion exchanger, Journal of Hazardous Materials, 2022, DOI: 10.1016/j.jhazmat.2022.128529, IF: 13.6 (2022)
[7]	W. Seremak, A. Baszczuk, M. Jasiorski, A. Gibas , M. Winnicki, Photocatalytic activity enhancement of low-pressure cold sprayed TiO ₂ coatings induced by

-
- long-term water vapour exposure, *Journal of Thermal Spray Technology*, 2021, DOI: 10.1007/s11666-021-01244-5, IF: 2.8 (2021)
-
- [8] **A. Gibas**, J. Gąsiorek, Perspective of sol-gel hydrophobic silica deposited using low-pressure cold spray and ultrasonic atomizing for automotive coatings, *Journal of TransLogistics*, ISSN 2450-5870, 2021, DOI: 10/JoT2021_08
-
- [9] M. Winnicki, **A. Gibas**, A. Baszczuk, M. Jasierski, Low pressure cold spraying of TiO₂ on acrylonitrile butadiene styrene (ABS), *Surface & Coatings Technology*, 2021, DOI: 10.1016/j.surfcoat.2020.126717, IF: 4.9 (2021)
-
- [10] **A. Gibas**, A. Baszczuk, M. Jasierski, M. Winnicki, Prospects of low-pressure cold spray for superhydrophobic coatings, *Coatings*, 2019, DOI: 10.3390/coatings9120829, IF: 2.4 (2019)
-
- [11] **A. Gibas**, M. Gnych, Tlenkowe materiały proszkowe otrzymywane metodą zol-żel jako atrakcyjny substrat do nanoszenia powłok techniką niskociśnieniowego natryskiwania na zimno, Wydawnictwo Naukowe TYGIEL, 2019, ISBN: 978-83-65932-70-9, <http://bc.wydawnictwo-tygiel.pl/publikacja/B748B37A-5C63-7A37-CE6D-B000648E2D2E>
-
- [12] V. Hoppe, **A. Gibas**, W. Grzegorzczak, M. Małecki, M. Hasiak, Experimental study of Fe-Ni-Ti-Cr system, *Interdisciplinary Journal of Engineering Sciences*, 2019, http://ijes.pwr.wroc.pl/Vol-VII/No-1/VII-p1-9_Hoppe.pdf
-

9.1.2 CONFERENCE CONTRIBUTIONS

The research presented in the thesis was also supported by 10 contributions (6 oral presentations and 4 posters) related to the thesis delivered at 8 international and 2 domestic scientific conferences (Table 7).

Table 7 Compilation of conference presentations

-
- [a] ORAL PRESENTATION: **A. Gibas**, A. Baszczuk, I. Jacukowicz-Sobala, A. Ciechanowska, M. Jasierski, Peroxide gel route: photocatalytic activity of TiO₂ in visible light and darkness, International Sol-Gel Conference, <https://premc.org/solgel2024>, Berlin, Germany, 1-6.09.2024.
-
- [b] ORAL PRESENTATION: **A. Gibas**, M. Winnicki, A. Baszczuk, Aerosol-assisted low-pressure cold spraying of TiO₂ suspension, Les Rencontres

Internationales de la Projection Thermique: 11 RIPT, <https://go.fzj.de/ript2024>, Jülich, Germany, 5-7.06.2024.

-
- [c] POSTER: **A. Gibas**, W. Seremak, Thermal spraying of sol-gel materials, Les Rencontres Internationales de la Projection Thermique: 11 RIPT, <https://go.fzj.de/ript2024>, Jülich, Germany, 5-7.06.2024.
-
- [d] ORAL PRESENTATION: **A. Gibas**, A. Baszczuk, All the shades of H₂O₂-sensitized TiO₂, Interdisciplinary Doctoral Symposium: Rajd Doktoranta 2024, Przesieka, Poland, 17-19.05.2024.
-
- [e] ORAL PRESENTATION: **A. Gibas**, I. Jacukowicz-Sobala, A. Baszczuk, M. Jasierski, A. Ciechanowska, E. Dworniczek, A. Seniuk, A. Lewińska, Photocatalytic and antibacterial properties of H₂O₂-sensitized TiO₂, 2nd International Conference an Advanced Materials for Bio-Related Applications, AMBRA 2024, <https://ambra.pwr.edu.pl>, Wroclaw, Poland, 19-23.05.2024.
-
- [f] POSTER: **A. Gibas**, M. Winnicki, Towards sustainable coatings: cold spray additive manufacturing, The Fourth International Conference on Intelligent Systems in Production Engineering and Maintenance, ISPEM 2023, <https://ispem.pwr.edu.pl>, Wroclaw, Poland, 13-15.09.2023.
-
- [g] POSTER: **A. Gibas**, A. Baszczuk, Effect of modification of TiO₂ powders using H₂O₂ on photocatalytic activity, original title: Wpływ modyfikacji proszków TiO₂ używając H₂O₂ na aktywność fotokatalityczną, XVI Kopernikańskie Seminarium Doktoranckie, Wydział Chemii Uniwersytet Mikołaja Kopernika w Toruniu, Toruń, 29-30.06.2023
-
- [h] ORAL PRESENTATION: **A. Gibas**, M. Winnicki, A. Baszczuk, M. Jasierski, Low pressure cold sprayed TiO₂ suspension coatings for visible-light photocatalytic applications, 6th International Thermal Spraying and Hardfacing Conference, ITSHC 2022: progress, application and modern technologies, <https://www.itshc.pwr.edu.pl>, Wroclaw, Poland, 22-23.09.2022.
-
- [i] ORAL PRESENTATION: **A. Gibas**, A. Baszczuk, M. Jasierski, M. Winnicki, Morphology and structure of selected low-pressure cold sprayed TiO₂ coatings analysed for working as photocatalysts, 10th edition of Les Rencontres Internationales de la Projection Thermique, 10 RIPT, <https://www.fz-juelich.de/en/iek/iek-1/news/news/10ript-2022-from-june-1st-to-3rd-in-julich>, Jülich, Germany, 1-3.06.2022.
-

-
- [j] POSTER: **A. Gibas**, J. Gąsiorek, Ultrasonic atomizing as a feasible method of sol-gel coatings fabrication, 7th ISGS Online Summer School: Hybrid Materials: cutting edge applications, Castelló de la Plana, Spain, 2-3.09.2020.
-

9.1.3 OTHER SCIENTIFIC EVENTS

The author of this thesis actively participated in organizing international scientific events:

- Conference secretary and editor of the book of abstract for the 2nd International Conference on Advanced Materials for Bio-Related Applications (AMBRA2024)
Contribution: event coordination, communications with keynote speakers, organizing conference materials, registration and participant management, organizing committee management, developing promotional materials, on-site support, best poster and best short communication contest management
- Organizing committee member for the 6th International Thermal Spraying and Hardfacing Conference (ITSHC2022)
Contribution: registration and participant management, on-site support, entertainment organization, developing promotional materials

9.1.4 GRANTS

The author of this thesis contributed to the following scientific projects:

- Sonic Jet - a precision printer for producing flexible electronics (in Polish: Sonic Jet - precyzyjna drukarka do wytwarzania elastycznej elektroniki), Lider 013/L/0009/20, grant type: NCBR, budget: 1 498 875.00 PLN, grant manager: dr. hab. inż. Marcin Winnicki
Contribution: Atomic force microscope analysis of silver traces
- Multi-scale numerical modeling of condensation and mechanical properties of organosilica-based aerogels, grant type: OPUS-LAP, NCN, budget: 1 243 624.00 PLN, grant manager: Leader: dr hab. inż. Jakub Maksymilian Gac, Warsaw University of Technology, Partner: mgr. inż. Bartosz Babiarczuk, Wrocław University of Science and Technology, Foreign partner: prof. Barbara Milow, The German Aerospace Center
Contribution: Raman spectroscopy analysis of silica aerogel formation

9.2 SCIENTIFIC CONTRIBUTIONS

9.2.1 AUTHOR CONTRIBUTION

The author of this thesis made a significant impact on the research, which included the following contributions:

- **Conceptualization:** Proposing the research idea and framework, formulating hypotheses and establishing experimental objectives.
- **Methodology:** Proposing methods and tools for conducting research. Designing and carrying out syntheses and modification procedures. Refining the coating preparation setup for spraying powders, suspensions and aerosolized suspensions. Selecting key parameters for the spraying process.
- **Formal analysis:** Interpreting all analysed data in the context of the study. Support in the statistical analysis.
- **Investigation:** Conducting experiments to generate primary data, XRD, Raman and IR spectroscopies, DRS, PSA, sedimentation, SEM, optical profilometry, cross-cut test, DSC/TGA, UV-Vis spectroscopy during dye degradation. Managing laboratory activities.
- **Resources:** Acquiring materials and small laboratory equipment. Managing access to datasets, computational tools, or relevant facilities.
- **Writing – Original Draft:** Drafting all initial manuscripts.
- **Writing – Review & Editing:** Revising the manuscript in response to feedback from coauthors and reviewers, polishing language, structuring and formatting.
- **Visualization:** Creating illustrations and schematics to explain concepts or methodologies, and generating figures, graphs, and tables to present data.
- **Project Administration:** Coordinating tasks, timelines, and responsibilities among coauthors. Managing communication.
- **Funding Acquisition:** Receiving an internal research grant for EPR and XPS measurements, precursors and substrates (Internal mini-grant for PhD students).

9.2.2 COAUTHORS' STATEMENTS

The statements of the coauthors are included on the following pages.

10 REPRINTS

This section provides the appended publications.

[A] A. Gibas, A. Baszczuk, M. Jasiorski, M. Winnicki, D. Ociński, **Preparation of visible-light active oxygen-rich TiO₂ coatings using low pressure cold spraying**, Coatings, 31.03.2022, DOI: 10.3390/coatings12040475.

[B] A. Gibas, M. Winnicki, A. Baszczuk, M. Jasiorski, **Influence of spraying parameters on microstructure of oxygen-rich TiO₂ coatings deposited using suspension low-pressure cold spray**, Surface & Coatings Technology, 14.02.2023, DOI: 10.1016/j.surfcoat.2023.129321.

[C] A. Gibas, A. Baszczuk, M. Jasiorski, A. Lewińska, M. Winnicki, **Low-pressure cold spraying of suspension TiO₂ in a single pass – Process optimization**, Surface & Coatings Technology, 19.08.2023, DOI: 10.1016/j.surfcoat.2023.129933.

+ Supplementary materials

[D] A. Gibas, M. Winnicki, A. Baszczuk, M. Jasiorski, **Aerosol-assisted low-pressure cold spraying of TiO₂ suspension**, Surface & Coatings Technology, 26.12.2024, DOI: 10.1016/j.surfcoat.2024.131715.

[E] A. Gibas, A. Baszczuk, I. Jacukowicz-Sobala, A. Ciechanowska, M. Jasiorski, E. Dworniczek, A. Seniuk, A. Lewińska, **H₂O₂-sensitized titania with activity under visible light and in the dark**, Journal of Environmental Chemical Engineering, 30.08.2024, DOI: 10.1016/j.jece.2024.113975.

+ Supplementary materials 1

+ Supplementary materials 2

Article

Preparation of Visible-Light Active Oxygen-Rich TiO₂ Coatings Using Low Pressure Cold Spraying

Anna Gibas ^{1,*} , Agnieszka Baszczuk ¹ , Marek Jasiorski ¹, Marcin Winnicki ²  and Daniel Ociński ³

¹ Department of Mechanics, Materials and Biomedical Engineering, Wrocław University of Science and Technology, 25 M. Smoluchowskiego Street, 50-370 Wrocław, Poland; agnieszka.baszczuk@pwr.edu.pl (A.B.); marek.jasiorski@pwr.edu.pl (M.J.)

² Department of Materials Science, Strength and Welding Technology, Wrocław University of Science and Technology, 5 Łukasiewicza Street, 50-371 Wrocław, Poland; marcin.winnicki@pwr.edu.pl

³ Department of Chemical Technology, Wrocław University of Economics and Business, 118/120 Komandorska Street, 53-345 Wrocław, Poland; daniel.ocinski@ue.wroc.pl

* Correspondence: anna.gibas@pwr.edu.pl

Abstract: Visible-light active photocatalysts in the form of coatings that can be produced using large-scale methods have attracted considerable attention. Here we show a facile approach to deposit coatings using the low pressure cold spray (LPCS) from oxygen-rich amorphous titanium dioxide, which is a structurally-unconventional feedstock powder for LPCS. We synthesized amorphous TiO₂, in which we introduced numerous defects, such as oxide groups (peroxy and superoxy) in volume and hydroxyl groups on the surface. Then we deposited as-prepared powder preserving the presence of active groups, which we demonstrated using Raman spectroscopy. To show the activity of the prepared coatings, we perform methylene blue degradation under visible light. Our research shows that it is worth considering the internal atomic structure and surface chemistry of the powders to be preserved after low pressure cold spraying.

Keywords: low pressure cold spraying; TiO₂; yellow TiO₂; visible-light-active photocatalyst; hydrogen peroxide



Citation: Gibas, A.; Baszczuk, A.; Jasiorski, M.; Winnicki, M.; Ociński, D. Preparation of Visible-Light Active Oxygen-Rich TiO₂ Coatings Using Low Pressure Cold Spraying. *Coatings* **2022**, *12*, 475. <https://doi.org/10.3390/coatings12040475>

Academic Editor:
Ana-Maria Lepadat

Received: 28 February 2022

Accepted: 30 March 2022

Published: 31 March 2022

Publisher's Note: MDPI stays neutral with regard to jurisdictional claims in published maps and institutional affiliations.



Copyright: © 2022 by the authors. Licensee MDPI, Basel, Switzerland. This article is an open access article distributed under the terms and conditions of the Creative Commons Attribution (CC BY) license (<https://creativecommons.org/licenses/by/4.0/>).

1. Introduction

The formation of TiO₂ photocatalytic coatings has been a constant challenge over the past 30 years [1–3]. During this time, titanium dioxide has remained one of the most photocatalytically efficient and highly stable materials, and stayed at a low price. TiO₂ coatings for photocatalytic systems may be produced through several low-temperature preparation techniques: by the transport of the precursor to the substrate using gas or plasma (chemical vapor deposition (CVD) [4], pulsed laser deposition (PLD) [5], atomic layer deposition (ALD) [6], ion sputtering [7]); deposition of liquid phase containing precursors (dip-coating [8], spin coating [9], spray pyrolysis [10]); or deposition of precursors in the solid-state (using screen-printing, doctor blade method [11] or thermal spraying [12]). Due to increasing environmental pollution, greener and more energy-efficient deposition methods that are large-scale and inexpensive are being actively sought. This urge does not change the main requirement of photocatalytic coatings, which is, namely, to retain or create a specific surface area as high as possible [13].

In response to those demands (apart from environmental safety and economic efficiency) the cold-spray method offers preservation of the nanoparticulate structure of the initial feedstock [14–16]. Several publications have already been published on various photocatalytic cold-sprayed coatings [12,15–17]. The coatings were cold sprayed most often using the high pressure variant (HPCS), >2 MPa [12], which have an environmental cost that consists of the consumption of gas and electrical power as well as the replacing of parts due to the relatively high rate of nozzle erosive wear [18]. Deposition at lower pressures

(below 1 MPa), in which the energy expenditure is reduced, if successful, proceeded so far with the use of helium or nitrogen as the carrier gas, just like in the HPCS variant [19]. Most cold-sprayed TiO₂ coatings concern commercially available crystalline TiO₂ feedstocks [19,20]. The most typical among them is Degussa (Evonik) P25, which is a mixture of rutile and anatase in a proportion of one to four [1,2]. Until now, we did not manage to find any successful approach to spray pure P25 without additions using the cold spray. Regardless of the deposition pressure, the deposition mechanism, and simultaneously, the main depositional problem of ceramic feedstock powder arises from its brittleness [21]. The impact of ceramic aggregates accelerated to sonic velocities causes the aggregate to break down, which then enables the interlocking of secondary particles. The as-formed layer is usually very thin as the incoming aggregates detach the already embedded particles [22]. In addition, too much energy (i.e., increased by the use of high pressure carrier gas) can lead to uncontrolled phase transformation (for instance of anatase to rutile, which is a less photocatalytically active polymorph) or grain overgrowth (decreasing particle surface area); while an insufficient amount energy impedes the embodiment of the particles [22]. The deposition efficiency in a cold spray can be enhanced by increasing the ductility of feedstock powder particles [16,17]. One method is to admix ductile phase to ceramic feedstock [17]. Another method is to spray amorphous TiO₂ [16], and this is the amorphous TiO₂ which seems, up to now, to be the only efficient variant for feedstock powder to deposit thick single-phase coatings using low pressure cold spray (LPCS). We showed in our previous work [16,23] that the synthesis of amorphous TiO₂ may, on the one hand, impart plasticity reducing erosion during the deposition process, and on the other hand favor the beneficial transformation in terms of photocatalytic efficiency (from the amorphous phase to anatase). In other research, we showed that amorphous powder can be an efficient photocatalyst, too [24].

There may be, however, even a better line of research for the cold spraying of photocatalytic coatings than the spraying of unmodified TiO₂. Previous efforts concerned mainly the physical parameters of feedstock powders, such as the degree of agglomeration or particle size [16,22,25–27]. What was not prioritized yet, is to consider the internal atomic structure and surface chemistry of the deposited powders. The wide bandgap of unmodified TiO₂ (approximately 3.0 eV for rutile and 3.2 eV for anatase) means that to obtain the activation energy for photocatalytic reactions, ultraviolet light is needed [1,2]. However, UV only constitutes ~5% of the solar energy that reaches the surface of Earth. To avoid artificial lighting and employ solar light, the latest scientific advancements in the field of photocatalysis aims to replace UV-activated photocatalysts with visible-light-induced photocatalysts [1,3]. Several strategies have been developed over the years in material sciences to alter the unmodified TiO₂ (both available on the market or self-synthesized). The main concept is to shift the absorption of TiO₂ towards longer wavelengths by doping the crystal structure with metal and non-metal ions [28,29]. Other ideas focus on dye sensitization [30] or the application of noble metals or other sensitizers as a cocatalyst to provide additional active sites [28,31]. The above procedures can be applied for already formed feedstock powder [29–31] or on the powder synthesis route [28]. All popular approaches rely on the interaction of new substances with TiO₂, which may lead to the formation of secondary impurities that could promote the adverse recombination of photogenerated charges ($e^- - h^+$). “Self-doped” TiO₂ with intrinsic point defects, such as vacancies and interstitials, might absorb energy from the visible region of the solar spectrum [32]. Such modified titanium dioxide is often no longer a white powder, however, it can turn black, grey or blue [32,33]. Although black TiO₂ is considered the most representative and effective for thermal hydrogenation (due to the absorption onset lying in the IR region and hence being activated with maximum solar energy) [34], its production requires complex synthetic methods. Moreover, oxygen vacancies and Ti⁺³ ions generated in this high-temperature or high-pressure process can give the material high photocatalytic activity, yet can also play a negative role by becoming recombination centers (especially when their distribution is uncontrolled and not limited only to the semiconductor surface) [32,33]. Recently, it has been shown

that self-doping TiO_2 may be caused not only by oxygen deficiency manifested by various shades of black of the oxide but also by an excess of oxygen (induced by the treatment with oxidizing agents, such as hydrogen peroxide), which yields yellow-orange coloring of titanium dioxide [33]. Similarly as TiO_2 obtained using other absorption-shifting strategies, oxygen-rich yellow TiO_2 can be produced either through bottom-up synthesis [35–39] or by surface modification [40–42]. In both ways, sensitizing TiO_2 with H_2O_2 is simple as it lacks involving doping agents, metals, non-metals, etc. and hence has great application potential in the industry. Triangular peroxo–titanate complexes formed during synthesis with O–O bonds are predisposed to capture photogenerated electrons and use them for photocatalytic degradation, which reduces unfavorable recombination processes and significantly improves photocatalytic ones [35,42]. What is more, oxygen self-doping using hydrogen peroxide (H_2O_2) enhances the photocatalytic efficiency of TiO_2 in the form of crystal phases, such as rutile, anatase [37,40,42], and even amorphous phase [36,38,39]. To the best of our knowledge, only the oxygen-rich TiO_2 powders have been studied so far [35–42], however, there are no records of them having been used as a feedstock for coatings formation. Bearing in mind the high deposition efficiency of the amorphous phase in the low pressure cold spray process [16,23,24] and observing the excellent well-documented photoactive performance under visible light irradiation of amorphous yellow TiO_2 powders [35–39], we decided to employ oxygen-rich feedstock powder for cold spraying to investigate the potential of the spraying of visible-light active photocatalytic coatings.

Here we show a facile approach to obtaining the visible-light active titanium dioxide coatings from self-synthesized oxygen-rich titanium dioxide using low pressure cold spraying. First, we synthesized nanoparticulate amorphous oxygen-rich TiO_2 feedstock powder by one-pot hydrolysis of titanium isopropoxide (TiO_2 precursor) and its reaction with hydrogen peroxide (H_2O_2). Then, we sprayed as-prepared feedstock aiming at maintaining its high photocatalytic efficiency. Knowing that the activity of oxygen-rich TiO_2 is determined by the complex chemical nature of both the interior and the surface of the semiconductor, we conducted a Raman spectroscopy inspection to show how deposition parameters affect the defect chemistry of TiO_2 . In the last part, we demonstrate the photocatalytic activity using the popular methylene blue dye as a model pollutant to ensure embedding activity in visible light.

2. Materials and Methods

2.1. Synthesis of Feedstock Powder

The amorphous oxygen-rich TiO_2 powder, referred to later as FP (feedstock powder), was produced in the one-pot synthesis. The reagents used were: 1 mL of nitric acid (HNO_3 , 65%, Chempur, Karlsruhe, Germany), 100 mL of demineralized water, 10 mL of titanium (IV) isopropoxide ($\text{Ti}[\text{OCH}(\text{CH}_3)_2]_4$, 97%, Sigma-Aldrich, St. Louis, MO, USA) and 20 mL hydrogen peroxide (H_2O_2 , 30%, Stanlab, Ltd., Lubin, Poland). Titanium precursor was added to the water-acid solution, and then the H_2O_2 was added to dope the already formed titanium dioxide with oxygen. A similar procedure was described elsewhere by Wu et al. in [35], with the difference being that in this research the titanium dioxide was air-dried at ambient temperature, not at 50 °C as Wu did. No color fading was observed after a year of storage in the air in room conditions.

2.2. Spraying of 200, 600 Coatings

As-synthesized feedstock powder was low pressure cold sprayed using DYMET 413 unit (Obninsk Center for Powder Spraying, Obninsk, Russia). Air with a pressure of 0.5 MPa served as a working gas and was accelerated in a circular de Laval nozzle with a throat and outlet diameters of 2.5 and 5 mm, respectively. Two various gas temperatures were tested: 200 and 600 °C. The samples produced in such conditions are referred to later as samples 200 and 600, respectively. A spraying gun was attached to the manipulator (BZT Maschinenbau GmbH, Leopoldshöhe, Germany) moving with a traverse speed of 2.5 mm/s and a stand-off distance of 10 mm. To ensure small waviness, the distance between the next

spraying beads was 2 mm. An untypical aerosol powder feeder (Palas GmbH, Karlsruhe, Germany) with a cylindrical chamber of 14 mm diameter, a height of 95 mm and a powder feeding rate of 61 g/h was applied. The powder was fed radially at the beginning of the divergent part of the nozzle by nitrogen with a pressure of 0.1 MPa. Aluminum alloy AW-1050A H14/H24 (min. 99.5 wt.% of Al) plates with dimensions of $20 \times 20 \times 4$ mm were selected as a substrate material. Before spraying, the substrate surface was degreased, and grit blasted with alumina powder (Al_2O_3 , mesh 45).

2.3. Feedstock Powder and Coatings Characterization

The crystal structure of feedstock powder and low pressure cold sprayed coatings was investigated using the X-ray diffractometer Ultima IV (Rigaku, Tokyo, Japan), with $\text{CuK}\alpha$ irradiation ($\lambda = 1.54056 \text{ \AA}$) for the 2θ ranging from 5° to 75° in the 0.05 steps 3 s per each measurement point.

The evaluation of the surface and sections of the samples were conducted using the SEM microscope (Hitachi S-3400 N, Tokyo, Japan). For the cross-sections of coatings, the samples were cut in the middle of their lengths, embedded in the resin and consecutively polished without etching. The topography of the feedstock powder and coatings after spraying was investigated without any additional preparation.

The particle size analysis of the feedstock powder was carried out by laser diffraction using PSA-1190 (Anton Paar GmbH, Graz, Austria). After the initial measurement, the powder was subjected to ultrasound treatment for 30 min to observe the changes in the size of the initial agglomerates.

The surface roughness (R_a , R_z) of the coatings was measured using a profilometer (Form Talysurf 120 L, Taylor-Hobson, Leicester, United Kingdom). The diamond stylus with a radius of $5 \mu\text{m}$ was transversed at the contact mode with a measuring force of 0.75 mN and a measuring speed of 1 mm/s along tracing length $L_t = 15 \text{ mm}$ and with a cut-off filter $\lambda_C = 2.5 \text{ mm}$.

The specific surface of the samples was measured using VHX-6000 digital microscope (Keyence, Osaka, Japan). The magnification was set to 200, which provided the surface area of $1.733 \text{ mm} \times 1.299 \text{ mm}$ (2.233 mm^2). Three measurements were carried out for all deposited coatings and the mean value was determined for 200 and 600 samples.

The mass of the coatings was established by weighting the initial substrate before and after coating deposition.

Diffuse Reflectance Spectroscopy (DRS) was applied to determine the bandgap value (E_g) of the TiO_2 feedstock powder and coatings using a UV-VIS spectrophotometer equipped with a 75 mm integrating sphere (Specord 210, Analytik Jena, Jena, Germany). The DRS spectra of the sample were measured in the range of 200–800 nm with a Spectralon[®] as the reference material. The Kubelka–Munk function (Equation (1)) was used to convert the obtained reflectance (R) into the absorption coefficient ($F(R)$), and the Tauc's plot ($[F(R)h\nu]^{0.5}$ vs. $h\nu$) was drawn to determine the bandgap energy (E_g):

$$F(R) = \frac{(1 - R)^2}{2R} \quad (1)$$

The Raman spectra of samples were collected using the Raman spectrophotometer LabRam HR800 (Horiba/Jobin-Yvon, Kyoto, Japan) upon Ar^+ laser excitation at 514.55 nm with 50 mW laser power within the spectral range from 50 to 4000 cm^{-1} .

The photocatalytic degradation of methylene blue (MB) was carried out in the TOPT-V reactor equipped with eight quartz vessels with magnetic stirrers, and a low-temperature cooling circulating pump (Toption Instruments Co., Xi'an, China). The TiO_2 covered plates, immersed in MB solution (100 mL , $1 \cdot 10^{-5} \text{ M} \approx 3.2 \text{ mg/L}$), were exposed to VIS irradiation emitted from a xenon lamp (300 W) with a UV cut-off filter. The measured light intensity on the surface of TiO_2 was 0.31 mW/cm^2 . To allow the equilibrium adsorption of MB on TiO_2 , the process was initially conducted in the dark for 1 h. During the experiments, aliquots of the solution were collected every hour and the concentration of methylene blue was

measured using a UV-VIS spectrometer (Specord 210 Plus, Analytik Jena, Jena, Germany) at the wavelength of 668 nm (the detection limit was 0.25 mg/L with $RSD \leq 6\%$). Due to an insignificant pH decrease, no chemicals were used to maintain pH at a constant level. All studies (MB photocatalytic degradation as well as adsorption in the dark) were conducted in the photoreactor equipped with a circulation cooling system to ensure constant temperatures (21.5 °C) of all solutions in individual experiments during the tests.

3. Results and Discussion

There are a number of factors that influence the efficiency of the TiO₂ heterogeneous photocatalysis process: i.e., the degree and type of long-range ordering of atoms in the material, morphological properties that mainly determine the active surface of the catalyst, as well as the defects of its structure and surface. The latter factor seems especially important for oxygen-rich TiO₂, which has been intentionally defected to achieve an additional activity in visible light. Therefore, here we conduct research on the structural characteristics of the manufactured materials (powders and coatings), taking into account the morphology, the degree of crystal order, and the analysis of chemical groups modifying titanium dioxide (e.g., O–O and hydroxyl groups). The high photocatalytic efficiency of yellow powders is well reported in the literature [35–40,42], and therefore the main objective of the research is to preserve it after spraying to produce coatings. Here we discuss the feedstock powder characteristic first and then compare the data with the records for coatings sprayed using carrier gas at two different temperatures: 200 and 600 °C.

3.1. Crystal Structure Analysed Using X-ray Diffraction (XRD)

At first, we studied the phase composition of oxygen-rich TiO₂ in the form of powder and coatings. In the diffraction pattern of the feedstock powder (Figure 1, black plot), the broad hump centered approximately on 2 theta 25° indicates the amorphous structure of the powder. The diffractograms for coatings show that the amorphous share can be preserved during spraying in both samples (Figure 1, green and red plots). Spraying of the powder with carrier gas at 600 °C (Figure 1, red plot) led to partial crystallization of the employed feedstock powder. An asymmetrical anatase reflection (with Miller indices 101) at 25.35° appears out of the amorphous hump. Furthermore, the background of this sample is raised in the regions where other anatase peaks are located (consecutively 37.80° (004), 48.05° (200), 53.90° (105), 55.05° (211), 62.70° (204), 68.75° (116) (ICSD-9852, marked as letter A). The remaining, medium-intensity, peaks in the 600 diffractograms are present at 38.45°, 44.70° and 65.50° and originate from the aluminum substrate (ICSD-18839, marked as Al).

For the 200 coating (Figure 1, green plot), the diffraction of aluminum is stronger than in the case of the 600 sample. For example, the peak at 38.45° is approximately 100 times more intense than the background level (inset in Figure 1), which is a result of penetration of the aluminum substrate by X-rays during the diffraction measurement caused by the low thickness of the 200 coating. Apart from the aluminum in the diffractogram of the 200 sample, an intense peak centered at about 25° can be found, which may seem identical to anatase (detected in the red plot), however, clear differences exist between them: aluminum oxide peak is sharper and more symmetrical than building up anatase and the additional peak in the green plot is shifted toward the right to appear at 2θ equal 25.55° (ICSD-9770, marked as Al₂O₃). An additional confirmation of the presence of aluminum oxide is that at higher angles all subsequently observed peaks match the peaks characteristic of the alumina phase. Al₂O₃ can occur in the sample as the residue of substrate grit-blasting or as the passivation product. Here, the residual Al₂O₃ is more probable, as XRD studies of the substrate after grit-blasting confirm its presence. Interface contamination with blasting medium is a very popular side effect of grit blasting and can be omitted by using crystalline titanium oxide instead of Al₂O₃ [43]. That said, there are reports on the deposition of TiO₂ coating on Al₂O₃ substrates which increased their photocatalytic activity [44]. If passivation occurs while depositing a partially amorphous coating, it may provide better

adhesion of the coating to the substrate, via overgrowing, through the residual porosity of the coating [24]. However, the detection of both Al and Al_2O_3 may be evidence of the poor deposition efficiency in 200 sample.

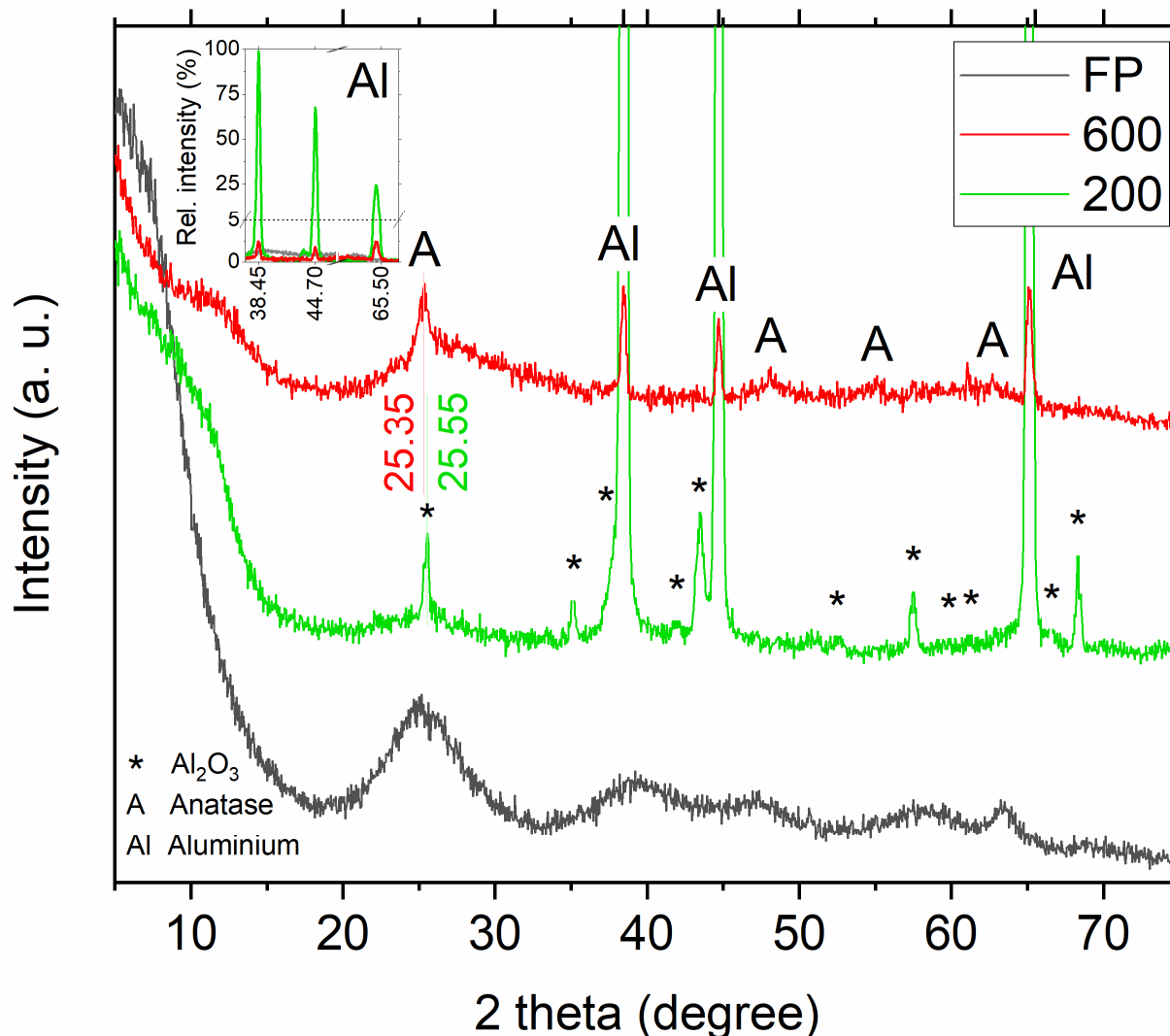


Figure 1. X-ray diffraction patterns of feedstock powder (black), sample 200 (green) and 600 (red).

The conducted X-ray diffraction tests showed that spraying the feedstock powder with cold gas has little effect on the long-range arrangement of the material. Even at a higher carrier gas temperature, the feedstock building coating crystallized only partially. At lower temperature, the deposited feedstock remained amorphous. We know from our previous work [23,24], that the amorphous form facilitated the deposition process and initiated the crystallization (observed here for the 600 sample), however, to determine the outcome for yellow TiO_2 , further structural characterization is needed.

3.2. Morphology and Microstructure Analysed Using Scanning Electron Microscopy (SEM) Supported via Particle Size Analysis and Roughness Measurements

The results of XRD diffraction imposes, especially in 200 sample, a significant reflection that originated from the substrate material, encouraging the observation of the topography and cross-section of the samples. Again, we begin our observation by investigating the morphology of the powder. SEM micrographs (Figure 2) reveal strongly unsymmetrical agglomerates of TiO_2 . The particle size of as-synthesized powder presented in (Figure 2a,b) is in the wide range of 6.8–212.2 μm ($D_{0.5} = 44.1 \mu\text{m}$). Regardless of the size of the

agglomerates (Figure 2c), they are porous and covered with smaller, densely packed unsymmetrical submicrometric flocculent particles. The agglomerates lacking flocculent covering seem denser, but still, they are characterized instead by the developed surface (Figure 2d). A 30-min ultrasound treatment for laser diffraction particle size analysis caused the detachment of the flocculent covering from the agglomerates, thus decreasing the size of the particles to 1.8–36.5 μm ($D_{0.5} = 12.9 \mu\text{m}$). This may suggest that the flocculent covering of agglomerates is weakly bonded, and hence it may be rather easily disintegrated, while in deposition (which proceeds in more drastic conditions than ultrasonication) (as in Figure 2d).

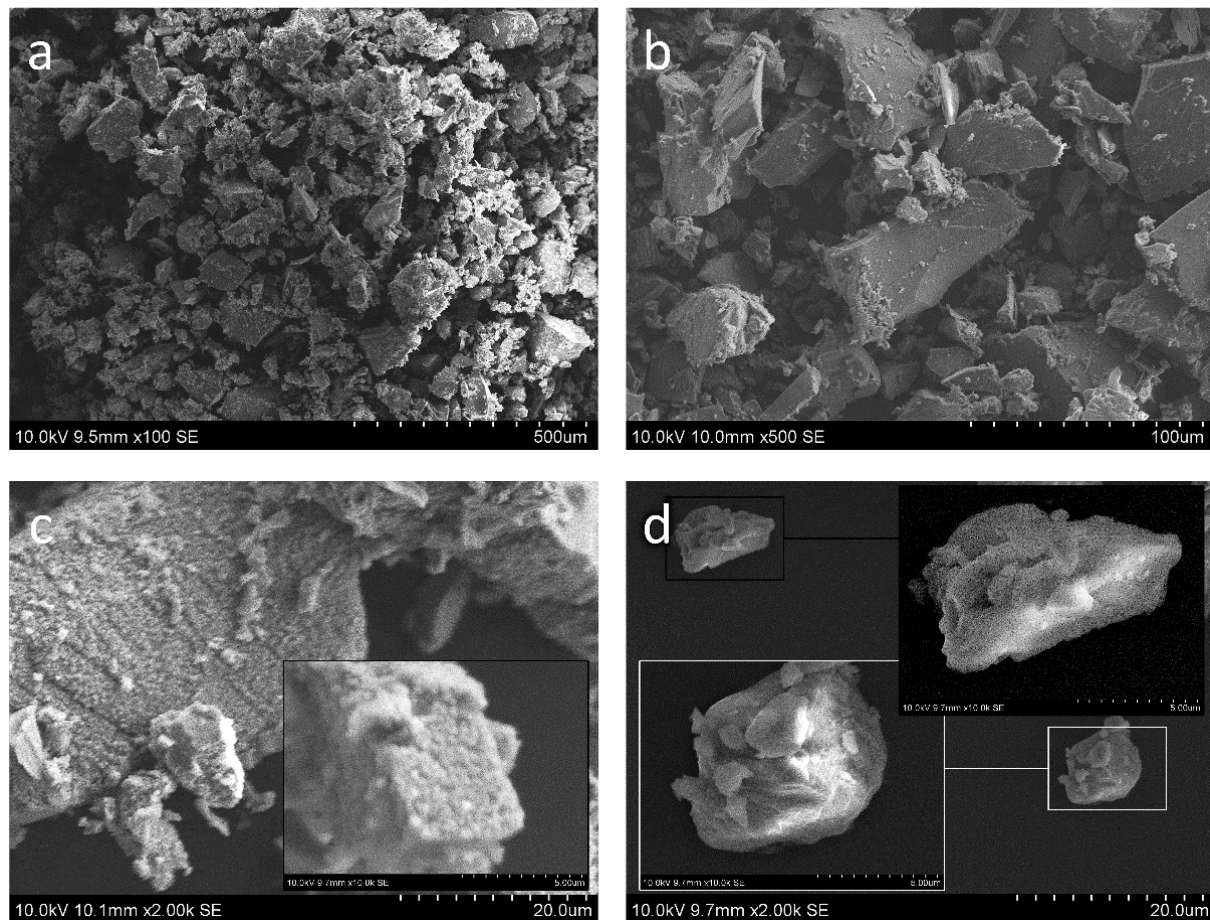


Figure 2. (a,b) SEM micrograph of feedstock powder morphology with a detailed view of (c) average as-synthesized agglomerates before DLS and (d) agglomerates after 30-min ultrasound treatment in DLS.

It is not only the particle interactions of a substrate that affects the deposition efficiency in cold spray; the surface roughness also has an impact. The irregular geometry introduced via grit-blasting ($R_a = 8.84 \mu\text{m}$, $R_z = 51.72 \mu\text{m}$) was developed to fit the size of the powder considered optimal for cold spray deposition. The initial parameters were modified upon the coating deposition process. The morphology of the 200 coating (Figure 3a) shows a rough surface with blunt edges of protruding irregularities. Since the roughness profile becomes more uniform after coating deposition ($R_a = 5.91 \mu\text{m}$, $R_z = 37.12 \mu\text{m}$) it would support the tendency of particles to fill the valleys of roughness and flatten only the top of the roughness peaks. However, at the magnification of 100 times, the coating is too thin to be successfully investigated (Figure 3c). On the contrary, the SEM morphology of the 600 sample (Figure 3b), shows an undulating surface. The substantial waviness is characteristic of cold sprayed coatings and results from the plastic deformation of the

surface upon anchoring large self-inflicted agglomerates [45]. The cross-sectional images (Figure 3d) reveal thick 25–50 μm dense coating, coarser with respect to the grit-blasted substrate ($R_a = 12.18 \mu\text{m}$, $R_z = 67.49 \mu\text{m}$). The roughness of the coatings favors the specific surface area. The measured specific surface of the 200 and 600 samples was 2.315 mm^2 and 2.456 mm^2 , respectively. Compared to the surface area measured for the flat sample before grit-blasting (2.253 mm^2), the 200 showed an increase in the surface of 3% and the 600 sample—by 9%. The surface area of grit-blasted substrates was 2.366 mm^2 , which means that the deposition of 200 coating flattened the surface, and the 600 coating—roughened it. Yet, at this magnification, good interlocking is observed throughout the entire cross-section.

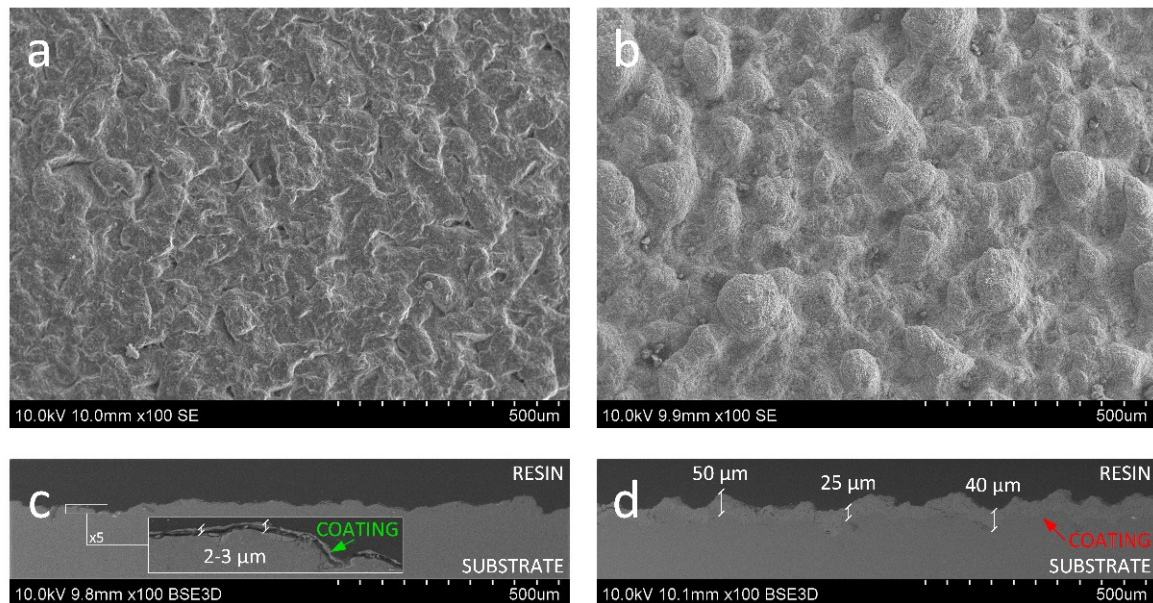


Figure 3. SEM micrograph of (a,b) topography and (c,d) cross section of (a,c) 200 and (b,d) 600 coatings. General view.

The morphology of the outer layer of both coatings (Figure 4a,b) has a feedstock powder-like structure. The top view of sample 200 resembles a shot-peened structure (Figure 4a). In the case of ceramic particles, the kinetic energy is transformed into the fragmentation of agglomerated particles instead of plastic deformation [45]. With this regard, probably only larger and denser agglomerates without flocculent cover reached the substrate and break apart upon impact. Generally, smaller particles, such as pieces of weakly bonded covering, accelerate more rapidly in the de Laval nozzle and achieve higher velocities, however, their kinetic energy can be lost in the bow shock region due to its lower mass [46]. The deceleration of the powder below the critical velocity contributes to the bouncing back of particles from the substrate and shock bow [26]. Hence, smaller flocculent particles are not observed in the 200 coating, which may be caused either by its bouncing back or its compaction by other incoming particles. The surface of the 600 sample seems more developed since the powder submicron structure was preserved (Figure 4b). The increase in the working gas temperature to 600 $^{\circ}\text{C}$ resulted in a greater acceleration of feedstock powder particles (even those flocculent covering—loose or weakly connected to the agglomerates) and therefore improved the impact velocity of particles and deposition efficiency, which is all consistent with the literature [27].

In both cases (Figure 4a,b), isolated discontinuities can be found (yellow arrows), much less frequently in the 600 sample, and hence the cross-sections were prepared to evaluate their severity (Figure 4c,d). In the case of the 200 sample, it was possible to form a very thin ceramic coating of 2–3 μm thickness (Figure 4c). The bond strength of the coating was not high enough to prevent detachment of the deposited particle by elastic spring-back forces during incoming particles bombardment [25]. The incoming particles significantly

densified the deposited thin ceramic coating, smoothing its surface upon the impact of the new particles. The thickness of the embedded coating was too small to absorb the excess energy, and, as a result, a net of cracks appeared in the coating material, leading to delamination of the coating. The cross-sections of the 600 sample (Figure 4d) show that it was possible to produce a uniform dense coating of high internal porosity and a rough surface well connected to the substrate. The outer part of the coating consists of loosely connected particles that were probably ejected from the gas stream and stuck on the coating surface. The detachments appear only in the upper part of the coating (yellow arrow, Figure 4d). The coating-substrate interface remains, however, solid.

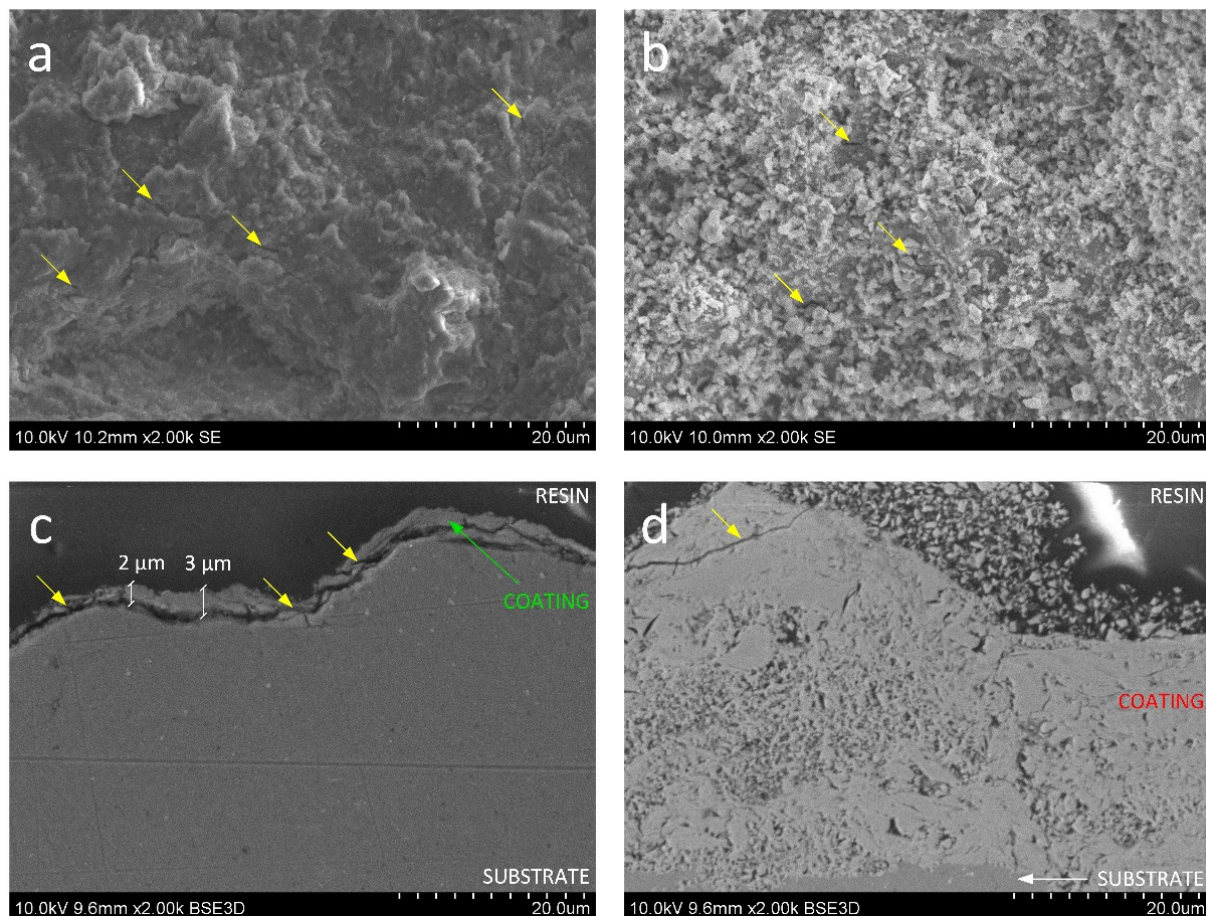


Figure 4. SEM micrograph of (a,b) topography and (c,d) cross section of (a,c) 200 and (b,d) 600 coatings. Detailed view.

The SEM analysis showed that in lower temperatures of carrier gas, only a very thin coating was possible to be deposited. Too low a level of both thermal and kinetic energy caused insufficient bonding of the coating to the substrate. Despite low adhesion, the coating was not fully detached and maintained contact with the substrate. The 600 coating was relatively thick and porous well connected to the substrate. The open porosity was the result of the agglomerates being broken apart and, as such, they revealed the internal porosity of the feedstock. Such reorganization enabled the surface of agglomerates to be compacted upon the impact on the substrate and the interior to be revealed. On one hand, the porosity may have been the origin of the crack formation, but in the case of the photocatalytic coatings, which were not under mechanical loading, the porosity ensures a high surface area.

3.3. Optical Properties Analysed Using Diffuse Reflectance Spectroscopy (DRS)

The optical properties of the feedstock powder and the cold-sprayed coatings were studied by UV-VIS diffuse reflectance spectra (DRS) (Figure 5). For all samples in the ultraviolet range, almost all incident UV light is absorbed (Figure 5a). The yellow color of the feedstock powder results in higher absorption at 400–500 nm visible as a shoulder to the peak located at ~320 nm (UV) [47]. The spectrally uniform absorption through the 400–800 nm range causes the yellow to fade, imparting simultaneously a grey-white finish [47]. The spectrum of the 600 sample shows a spectral response towards the visible region from 500 to 700 nm. The Tauc plots were used to estimate the bandgaps (Figure 5b). The Tauc plot for the feedstock powder reveals the presence of two optical bandgaps: one at 2.54 eV and another one at 2.24 eV. The records indicate that sample 200 has a lower bandgap (2.83 eV) than sample 600 (3.09 eV).

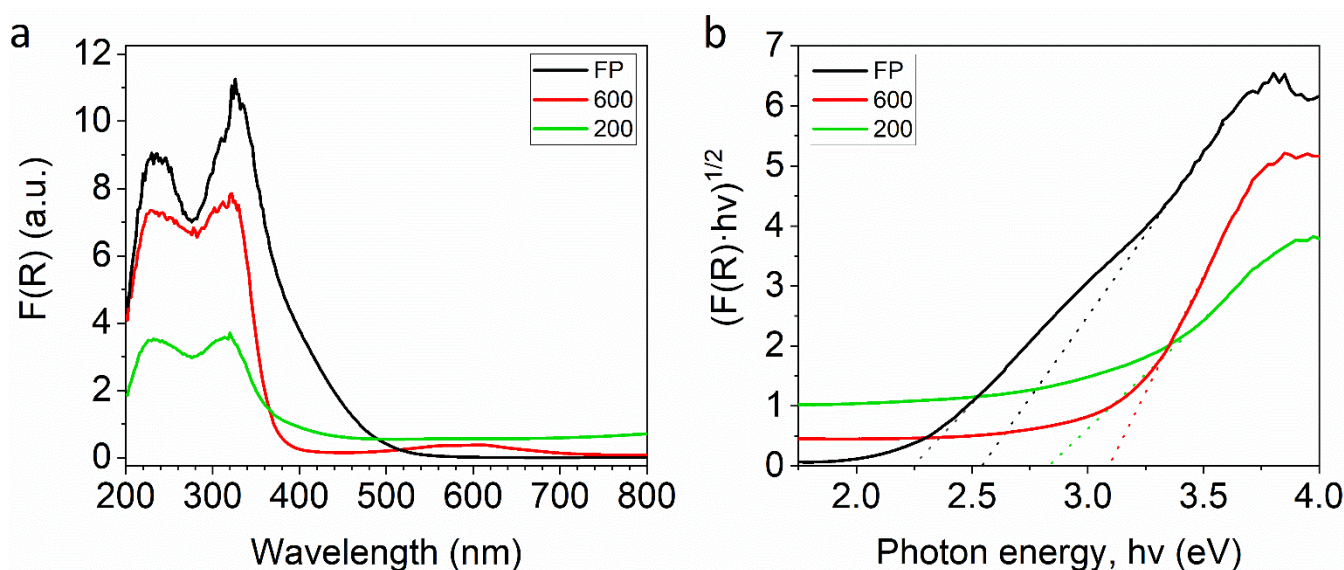


Figure 5. (a) Kubelka–Munk function spectra with (b) Tauc plot for estimating the bandgap energy for feedstock powder (black), sample 200 (green) and 600 (red).

The edge of adsorption is generally dependent on the crystal structure and the number of active sites (such as defects or dopants) [35]. In the literature, it is shown that the slight decrease in the bandgap could be, for instance, the result of oxygen vacancies and titanium ions present in the sample [48]. In other research, it is stated that the more defected state would lower the bandgap even more [49]. Here, the broadening of the bandgap of coatings with regard to feedstock powder must be directly related to the structural reorganization induced by spraying. The diffraction measurements (Figure 1) showed only a slight tendency to increase the degree of ordering of the titanium dioxide powder as a result of the spraying, while the optical measurements suggest that, in addition, there are also more subtle changes in the chemical structure. Therefore, it is necessary to investigate the structure and chemical composition of materials at the molecular level.

3.4. Vibrational Characterization Using Raman Spectroscopy

To gain additional information about the existence of the $-O-O-$ coordination bonds in feedstock powder and coatings, the Raman scattering of all samples were measured (Figure 6). The summary of Raman analysis is displayed for convenience in Table 1.

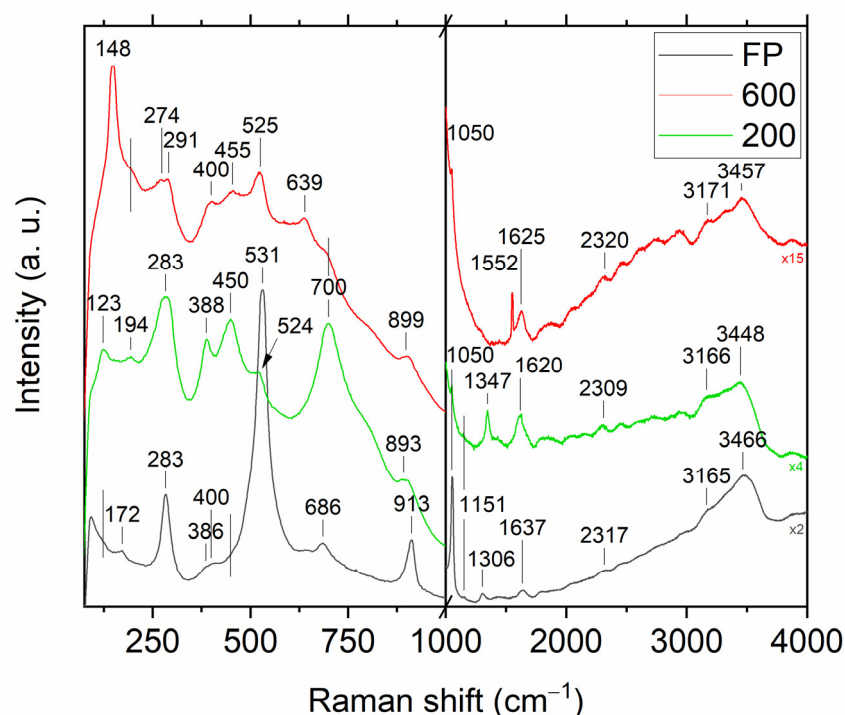


Figure 6. Raman spectra of feedstock powder (black), sample 200 (green) and 600 (red).

Due to omitting the drying step at elevated temperatures, we produced feedstock powder in the amorphous form (Figure 6, black plot). The amorphous structure of the powder has already been proven using XRD measurements (Figure 1), however the Raman spectroscopy is sensitive even to substantial changes in short-range interactions, which allows one to identify individual chemical bonds even in disordered amorphous materials. The low-intensity wide band found at about 400 cm^{-1} was the only common band for the obtained spectra and anatase phase (B_{1g}), yet due to the fact that no stronger anatase vibrational mode (especially E_g mode at 147 cm^{-1} [50]) was observed in the spectrum, the formation of anatase in the feedstock powder was excluded. Furthermore, no characteristic bands for anatase could be found in sample 200 (Figure 6, green plot). The anatase structure ($148, 194, 400, 525, 638\text{ cm}^{-1}$ [50,51]), as identified by XRD (Figure 1), was detected only in a sample sprayed with carrier gas at $600\text{ }^{\circ}\text{C}$ (Figure 6, red plot). If there is no evidence to consider crystal forms of TiO_2 in feedstock powder and given that in the Raman spectra of samples 200 and 600 not every band is explained so far, one may think that other modes originate from the interaction of Ti atoms with different forms of oxygen formed during synthesis [35].

The most intense band of feedstock powder spectra is located at 531 cm^{-1} . The mode observed in the range of $524\text{--}529\text{ cm}^{-1}$ can be connected with the stretching vibration of Ti-O_2^{2-} , in which O_2^{2-} is bound to a single Ti^{4+} center in a side-on bonding configuration [52], which is called a triangular peroxy titanyl group in some works [53]. The presence of a band at this frequency is considered to be evidence of obtaining an oxygen-rich titanium dioxide powder containing O_2^{2-} species incorporated during synthesis. When analyzing the spectrum of sample 200, a decrease in the intensity of this band is noticeable, which may indicate a partial loss of these active oxygen groups in the coating. In the 600 sample, it is not possible to detect the presence of a Ti-O_2^{2-} band, as even if it exists, it overlaps with a relatively intense A_{1g} anatase band at a frequency of 525 cm^{-1} .

In search of further evidence of significant modifications of the structure of titanium dioxide, it is worth looking at the band that appears in the case of feedstock powder at 686 cm^{-1} . This band is ascribed to stretching vibrations of Ti-O-O groups [54] or involving two-fold oxygen [55] in the literature. However, it is still unclear whether the Ti-O-O

vibration describes the vibrations of the peroxide group (i.e., the oxygen bridge --O--O-- , O_2^{2-}) or the superoxide group (i.e., --O--O the end-on configuration, O_2^- , where two oxygen are attached to only one titanium ion). These two types of dioxygen groups differ significantly in the length of O–O bonds, which in Raman spectroscopy should cause a shift of the observed bands. Since the length of O–O bond in superoxides (O_2^-) is smaller than in the peroxide (O_2^{2-}) [56] groups, which corresponds to higher bond strength, a higher frequency of vibrations of the superoxide (O_2^-) groups can be expected. Moreover, in addition to the well-described peroxides and superoxides, there are species that have an intermediate character [56]. Compared to the state observed in feedstock powder, the intensity of the Ti–O–O band visible in the 200 sample significantly increases and shifts toward higher frequencies (700 cm^{-1}), which may indicate an increase in the content of Ti–O–O groups in the coating and, at the same time, reduce the distance between the interconnected oxide atoms, and thus increase the content of superoxide groups (O_2^-) in the coatings at the expense of peroxides (O_2^{2-}). The band at about 700 cm^{-1} is still visible in the coating sprayed at 600°C , although it is not as intense as the bands of anatase.

The Raman spectra of the measured samples contain two more bands in the frequency ranges, which in the literature are ascribed to the vibration of the triangular peroxy titanyl group, in which O–O vibrations [39,52,57] or Ti–O vibrations [53,54] occur. The O–O stretching in the feedstock powder is observed at 913 cm^{-1} , and in coatings, it blueshifts and loses intensity more for coating sprayed at higher temperatures. The intensity of the Ti–O vibrations in triangular titanyl groups (at $\sim 1050\text{ cm}^{-1}$) [53] is also reduced due to spraying. Therefore, all three bands assigned in the powder spectrum to the triangular titanyl groups (531 , 913 and 1054 cm^{-1}) after spraying show a reduced intensity, indicating the thermal instability of the triangular peroxide species, which is consistent with the literature reports [53]. The disintegration of unstable peroxide groups is accompanied by the appearance of superoxide groups in the coatings, which is evidenced by an increase in the intensity of the 700 cm^{-1} band in the spectra of the 200 coating. The second characteristic superoxide band [58] can be found at 1145 cm^{-1} of the 200 spectrum. The superoxides are present also in the spectrum of the feedstock powder ($\sim 1152\text{ cm}^{-1}$), which shows that H_2O_2 treatment forms not only peroxide groups. The typical band for superoxide groups (1145 , $\sim 1152\text{ cm}^{-1}$) is not observed in the 600 coating, however, it is notable that only in the case of the coating sprayed with gas at a temperature of 600°C can a very characteristic, sharp and relatively intense band at 1552 cm^{-1} , attributed to molecular oxygen (O_2) vibrations, be identified [59]. This observation implies that the active and fairly labile superoxide species present in the powder decomposes with the evolution of oxygen during the spraying of the 600 sample.

Since a correlation was found between the presence and number of hydroxyl groups on the TiO_2 surface and the photocatalytic potential (by helping to form radicals) [41], it is worth examining the measured Raman spectra in this regard. In all samples, broad high-frequency bands can be distinguished and usually assigned to OH groups, however, their intensity is the highest in the case of feedstock powder (green and red plots are y-stretched $\times 4$ and $\times 15$ times, respectively). The irregularity of the peaks may indicate several bands that overlap in that energy shift. The Raman spectra of all samples are characterized by the bands of OH group stretching and bending at $\sim 3160\text{--}3450\text{ cm}^{-1}$ (O–H stretching and bending vibrations, [59]) and deformation vibrations at $\sim 1620\text{--}1640\text{ cm}^{-1}$ (chemisorbed and/or physisorbed H–O–H [60]), which is evidence of a large amount of water molecules, adsorbed on the surface of titanium dioxide both in feedstock powder and in coatings. Another band associated with hydroxyl groups can be found at 283 cm^{-1} . It is easy to see that the width and the asymmetry of this band both increase after the spraying. In the literature on oxygen-rich TiO_2 , vibrations in this frequency range are attributed to either Ti–O–H [40,41] or the intrinsic host lattice defects—oxygen vacancies [39,52], which are typical for oxides. Since spraying causes the appearance of two bands in the spectrum of the 600 sample, it can be assumed that the coatings contain both oxygen defects and

Ti–OH groups. Additional evidence of oxygen vacancies (in ordered structure) or oxygen deficiency (in disordered structure) can be found at $\sim 450\text{ cm}^{-1}$ [55,61].

Table 1. Assignments of the Raman bands in feedstock powder (black), sample 200 (green), and 600 (red).

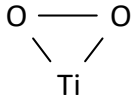
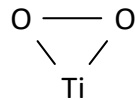
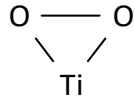
Description	Scheme	Observed Shift (Figure 6) (cm^{-1})			Reported Shift (Literature Data) (cm^{-1})
		FP	200	600	
Anatase E_g mode (symmetric stretching vibration of O–Ti–O)	O — Ti — O			148	147 [50]
O–O vibration involving three- and four-coordinate oxygen	O — O	172	194	194	160–240 [62]
Anatase E_g mode (symmetric stretching vibration of O–Ti–O)	O — Ti — O				198 [50]
Ti–OH vibration	Ti — O — H	283	283	274	282 [41]
Oxygen vacancy (v_O) (consequence of lack of oxygen)	Ti — v_O — Ti			291	284 [40]
Ti–O bending and stretching vibration involving two-fold oxygen (X—unspecified atom)	Ti — O — X	~ 382	388		283 [52]
Anatase B_{1g} mode (anti-symmetric bending vibration of O–Ti–O)	O — Ti — O	~ 400		400	286 [39]
Ti–O bending vibration involving three-fold oxygen (consequence of lack of oxygen)	Ti — O		450	455	380 [55] *
Anatase A_{1g} , B_{1g} mode (symmetric and anti-symmetric bending vibration of O–Ti–O)	O — Ti — O				398 [50]
Ti–O ₂ symmetric stretching vibration of triangular peroxy titanyl group		531	524	525	400–425 [63]
Anatase E_g mode (symmetric stretching vibration of O–Ti–O)	O — Ti — O			639	440 [55] *
Ti–O–O stretching vibration (representing peroxy, superoxy or intermediate groups)	Ti — O — O Ti — O — O — X	686	700	~ 700	440 [61]
O–O stretching vibration of coordinated peroxide (O_2^{2-}) species in triangular peroxy titanyl group		913	~ 903	~ 900	507, 519 [50]
Ti–O ₂ band vibration in triangular peroxy titanyl group		1050	1050	1050	524–529 [52]
O ₂ ^{•−} superoxide vibration	O — O ^{•−}	1152	1145		626–640 [63]
O–O vibration in H ₂ O ₂	H — O — O — H		1347		640 [50]
O–O stretching vibration in O ₂ (molecular oxygen)	O = O			1552	667 [54]

Table 1. Cont.

Description	Scheme	Observed Shift (Figure 6) (cm ⁻¹)			Reported Shift (Literature Data) (cm ⁻¹)
		FP	200	600	
OH bending vibration or scissoring of the chemisorbed and/or physisorbed water	H — O — H	1637	1620	1625	1630 [60]
Precursor residuals vibration	$ \begin{array}{c} \text{CH}_3 \\ \\ \text{C} \\ / \quad \backslash \\ \text{CH}_3 \quad \text{O} \end{array} $	2317	2309	2320	2335 [54]
OH stretching vibration of hydroxyl groups from adsorbed water	H — O — H	~3165	3166	3171	3050–3150 [59]
OH stretching vibration of H-bounded hydroxyl groups	H — O	3332	3340	3315	3150–3500 [59]
OH stretching and bending vibration of surface mixed hydroxyl groups	H — O	3466	3448	3457	3400–3600 [59]

* The referential data can be found in supplementary materials of the cited literature.

Considering the potential use of oxygen-rich TiO₂ coatings in photocatalytic reactors, the Raman measurements showed that the cold spraying process changes the chemical structure of the deposited powder. There is a visible decrease in the number of triangular peroxy titanyl groups and an increase in superoxide species could be crucial regarding the photocatalytic activity of coatings. The measured optical bandgap energy of the feedstock powder increases after the coating is deposited at 200 °C and experiences an even greater increase when the spraying temperature was 600 °C. In the literature [48,49], the differences in the bandgap width of the oxygen-rich and pure TiO₂ without additions are explained as a result of the introduction of oxygen defects into the structure of titanium dioxide, creating additional energy levels above the valence band. The Raman measurements showed that oxygen defects in feedstock powder and coatings have various forms (e.g., of superoxide groups, peroxide groups) and their number and type change depending on the parameters of coating deposition. These changes undoubtedly affect the electronic structure of TiO₂. However, the increase in the TiO₂ bandgap itself in no way determines the changes in photocatalytic activity. That is due to the loss of the peroxy groups in the coatings being considered to be responsible for the activity of the photocatalyst in visible light, which is compensated by the formation of superoxide groups known as oxidizing agents and radical initiators. Unpaired electrons make superoxides highly reactive, allowing them to oxidize various organic pollutants [65]. Many studies have shown that the hydroxyl groups on the metal oxide are responsible for trapping photogenerated charge carriers, resulting in a reduced rate of the recombination of electron-hole pairs [41]. Thus, the optimistic note is that spraying does not appear to significantly alter the level of hydroxylation of the titanium dioxide surface.

3.5. Visible-Light Photocatalytic Activity via Photobleaching of Methylene Blue

The analysis of the Raman spectra revealed that the coatings had a significant number of active oxygen species and hydroxyl groups, which suggests that the coatings should exhibit some photocatalytic activity in visible light. Although the bandgap is not directly connected to photocatalytic performance, it may be useful to select the activation light [41]. The bandgap of 200 sample was 2.8 eV, making the coating a promising candidate. Even if the 600 sample was characterized by a higher bandgap, with its crystal structure (mixed amorphous-anatase phase) it is a good candidate as well. It is important to emphasize that the masses of 200 and 600 coatings were considerably different, which is a result of

the various coating thicknesses (Figures 3 and 4). The 600 coatings weighed 35 ± 9 mg and all 200 coatings—were less than 1 mg. We summarize the results in Table 2. With this information, we performed the methylene blue (MB) degradation experiments under VIS irradiation to investigate the photocatalytic performance of 200 and 600 samples.

Table 2. Summary of the characterization of the samples 200 (green), and 600 (red).

Sample	Phase Composition	Thickness [μm]	Bandgap [eV]	Coating Mass ** [mg]	MB Adsorption in DARK [%]	MB Degradation in VIS [%]
200	Amorphous	2–3	2.83	<1 ***	negligible	3.1
600	Amorphous-anatase	25–50	3.09	35 ± 9	3.95	17.2

** Calculated as the difference between the mass of the coated sample and sample before spraying. *** The differences were lower than 1 mg.

The UV-VIS spectra of methylene blue before and after visible light irradiation (Figure 7a) show that the peak at 667 nm decreased markedly in the presence of the 600 sample (and only slightly in the case of the 200 sample), indicating the degradation of the auxochrome group of methylene blue, and revealing photocatalytic properties of the studied coatings after being irradiated with VIS light in the range of 450–650 nm (Figure 7b). As expected, both coatings exhibit some photocatalytic properties under visible light (Figure 7c,d, full markers). The 200 sample (Figure 7c) with a lower bandgap (2.83 eV) is substantially less active (3.1% MB degradation). The 600 sample (Figure 7d), characterized by the higher bandgap (3.09 eV), shows evident photocatalytic activity under visible light (17.2% MB degradation). To distinguish the adsorptive properties of both coatings from their activity, we performed additional tests in the dark (Figure 7c,d, empty markers). In the absence of the photocatalysts, no degradation of MB under visible light irradiation was observed. The MB adsorption efficiency (in the dark) was negligible for sample 200 and minor for sample 600 (3.95%).

The difference in the MB degradation efficiency and adsorption can be assigned to a substantially lower mass of the 200 sample (<1 mg, thickness 2–3 μm) than the mass of sample 600 (~34 mg, thickness 25–50 μm) and a different spatial structure. As the interfacial surface is primarily responsible for the effectiveness of all surface processes, the limited deposition of TiO_2 in the 200 sample resulted in a lower specific surface area, and finally in much lower photocatalytic activity. Due to the high porosity of both samples, the higher thickness of the 600 sample was more beneficial in terms of providing a higher specific surface area. Moreover, referring to the efficiency of the studied photocatalytic process, one can note that it was conducted under very low irradiance ($0.31 \text{ mW}/\text{cm}^2$; $\lambda > 460 \text{ nm}$), and for a small catalyst area (400 mm^2) immersed in 100 mL of the MB solution. Generally, with an increase in the intensity of radiation, an increase in the number of photons reaching the surface of the photocatalyst can be observed, which in turn causes the increase in the number of decomposed MB molecules. The enhancement of the photocatalytic performance of oxygen-rich TiO_2 can be the surface composition and size distribution rather than the lower bandgaps [41]. Nevertheless, in the presented results, both coatings, which remained mechanically stable after the test, demonstrated the photodegradation of methylene blue. In the case of the 200 sample, it is important to provide an adequate surface specific area, which is also possible using the cold spray method and together with a lower bandgap could impart higher photocatalytic activity. The obtained results reveal the high photocatalytic activity of the 600 sample obtained by the proposed cold spray method and make further research relevant and promising.

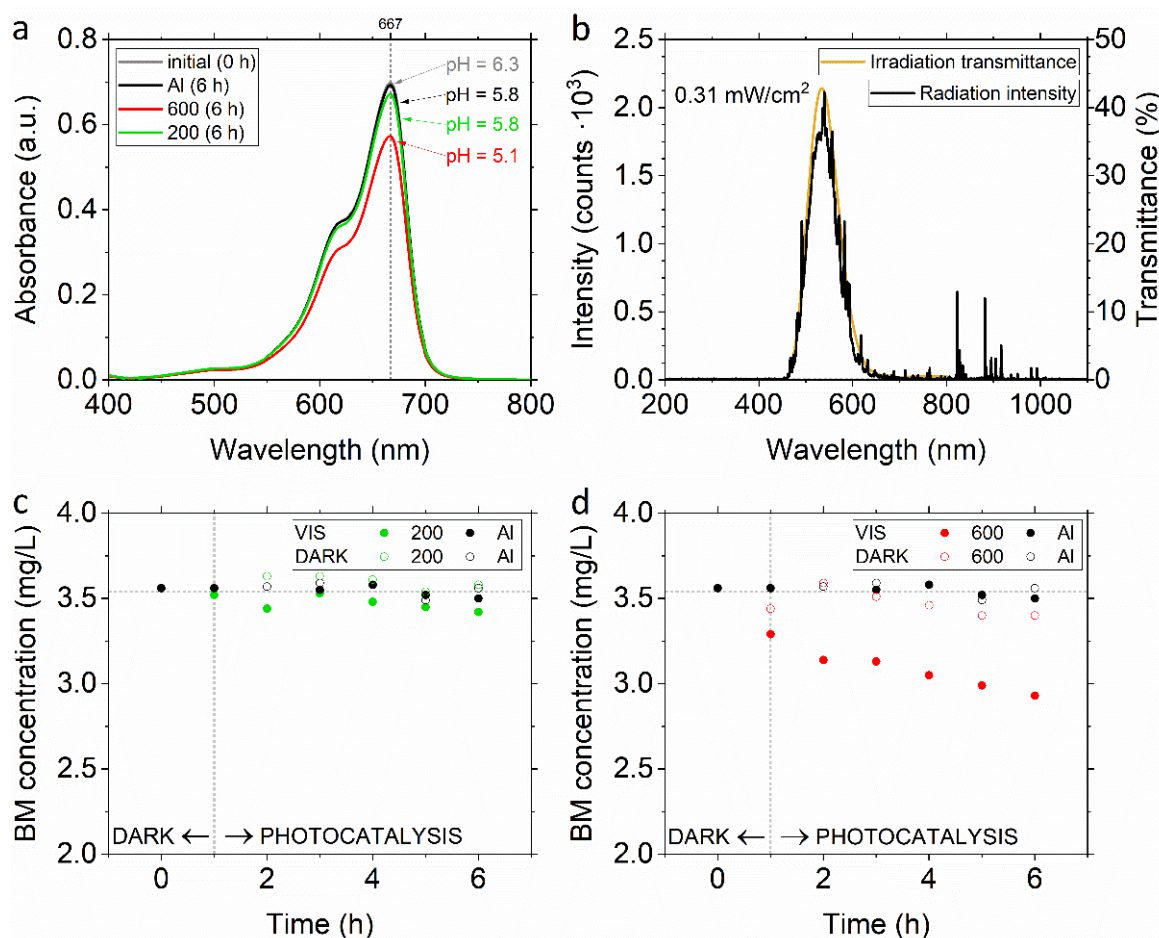


Figure 7. (a) Absorption spectra and (c,d) kinetics of methylene blue (MB) degradation in the presence of sample 200 (green) and 600 (red) and inactive Al substrate (black) under visible light irradiation from Xe lamp equipped with the UV cut-off filter (b) with its characteristics: measured radiation intensity (black), irradiation transmittance through the UV cut-off filter measured spectrophotometrically (yellow).

4. Conclusions

In this study, we low pressure cold sprayed amorphous oxygen-rich titanium dioxide to produce the coatings exhibiting photocatalytic activity in visible light. We analyzed changes in the feedstock powder before and after spraying to understand how the selected parameters influence the efficiency of the heterogeneous TiO₂ photocatalysis process. Using carrier gas at 600 °C, we deposited a thick (25–50 µm), porous coating with a highly developed surface. Spraying with gas preheated to 200 °C led to the formation of a relatively thinner (2–3 µm) coating with a net of discontinuities. We showed that both coatings were effective in the degradation of methylene blue upon the visible light irradiation, and the morphology of both has not changed after the photocatalytic efficiency test. Hence, the chosen powder immobilization method (LPCS) selected as a result of the efficiency of deposition of amorphous materials turned out to be safe for the subtle, yet substantial, physicochemical structure of the oxygen-rich feedstock powder. Consequently, low pressure cold spraying not only represents low-temperature large-scale technology; it also allows for the preservation of the feedstock powder absorption edge extended to visible light.

Author Contributions: Conceptualization, A.G. and A.B.; methodology, A.G., A.B. and D.O.; validation, A.B., M.J., M.W.; formal analysis, A.G., A.B., D.O., M.W. and M.J.; investigation, A.G., A.B., M.J., D.O. and M.W.; resources, M.J., M.W. and D.O.; data curation, A.G., A.B., D.O.; writing—original

draft preparation, A.G., A.B., M.J., M.W. and D.O.; writing—review and editing, A.G. and A.B.; visualization, A.G.; supervision, A.B.; project administration, A.G.; funding acquisition, A.B. and M.J. All authors have read and agreed to the published version of the manuscript.

Funding: This research was funded under statutory activity subsidy from the Polish Ministry of Education and Science for Wrocław University of Science and Technology (K58W10D07, K60W10D07) under grant number 8211104160.

Institutional Review Board Statement: Not applicable.

Informed Consent Statement: Not applicable.

Data Availability Statement: Not applicable.

Acknowledgments: A.G. acknowledges special thanks to Irena Jacukowicz-Sobala, Department of Chemical Technology, Wrocław University of Economics and Business, for her involvement and guidance in UV-VIS measurements.

Conflicts of Interest: The authors declare no conflict of interest.

References

1. Ferreira, V.R.A.; Santos, P.R.M.; Silva, C.I.Q.; Azenha, M.A. Latest developments on TiO₂-based photocatalysis: A special focus on selectivity and hollowness for enhanced photonic efficiency. *Appl. Catal. A Gen.* **2021**, *623*, 118243. [\[CrossRef\]](#)
2. Bideau, M.; Claudel, B.; Dubien, C.; Faure, L.; Kazouan, H. On the “immobilization” of titanium dioxide in the photocatalytic oxidation of spent waters. *J. Photochem. Photobiol. A Chem.* **1995**, *91*, 137–144. [\[CrossRef\]](#)
3. Sundar, K.P.; Kanmani, S. Progression of Photocatalytic reactors and it's comparison: A Review. *Chem. Eng. Res. Des.* **2020**, *154*, 135–150. [\[CrossRef\]](#)
4. Nagasawa, H.; Xu, J.; Kanezashi, M.; Tsuru, T. Atmospheric-pressure plasma-enhanced chemical vapor deposition of UV-shielding TiO₂ coatings on transparent plastics. *Mater. Lett.* **2018**, *228*, 479–481. [\[CrossRef\]](#)
5. Al Mashary, F.S.; Felix, J.F.; Ferreira, S.O.; de Souza, D.; Gobato, Y.G.; Chauhan, J.; Alexeeva, N.; Henini, M.; Albadri, A.M.; Alyamani, A.Y. Investigation of the structural, optical and electrical properties of indium-doped TiO₂ thin films grown by Pulsed Laser Deposition technique on low and high index GaAs planes. *Mater. Sci. Eng. B* **2020**, *259*, 114578. [\[CrossRef\]](#)
6. Badovinac, I.J.; Peter, R.; Omerzu, A.; Salamon, K.; Šarić, I.; Samaržija, A.; Perčić, M.; Piltaver, I.K.; Ambrožić, G.; Petravić, M. Grain size effect on photocatalytic activity of TiO₂ thin films grown by atomic layer deposition. *Thin Solid Films* **2020**, *709*, 138215. [\[CrossRef\]](#)
7. Al-Baradi, A.M. Sputtered and heat-treated TiO₂ electrodes for dye-sensitized solar cells applications. *Results Phys.* **2020**, *17*, 103109. [\[CrossRef\]](#)
8. Simeonov, S.; Szekeres, A.; Covei, M.; Spasov, D.; Kitin, G.; Predoana, L.; Calderon-Moreno, J.M.; Nicolescu, M.; Preda, S.; Stroescu, H.; et al. Inter-trap tunneling in vanadium doped TiO₂ sol-gel films. *Mater. Res. Bull.* **2020**, *127*, 110854. [\[CrossRef\]](#)
9. Pala, L.P.R.; Uday, V.; Gogoi, D.; Peela, N.R. Surface and photocatalytic properties of TiO₂ thin films prepared by non-aqueous surfactant assisted sol-gel method. *J. Environ. Chem. Eng.* **2020**, *8*, 104267. [\[CrossRef\]](#)
10. Doubi, Y.; Hartiti, B.; Hicham, L.; Fadili, S.; Batan, A.; Tahri, M.; Belfhaili, A.; Thevnin, P. Effect of annealing time on structural and optical proprieties of TiO₂ thin films elaborated by spray pyrolysis technique for future gas sensor application. *Mater. Today Proc.* **2020**, *30*, 823–827. [\[CrossRef\]](#)
11. Agrawal, A.; Siddiqui, S.A.; Soni, A.; Khandelwal, K.; Sharma, G.D. Performance analysis of TiO₂ based dye sensitized solar cell prepared by screen printing and doctor blade deposition techniques. *Sol. Energy* **2021**, *226*, 9–19. [\[CrossRef\]](#)
12. Roata, I.C.; Croitoru, C.; Pascu, A.; Stanciu, E.M. Photocatalytic coatings via thermal spraying: A mini-review. *AIMS Mater. Sci.* **2019**, *6*, 335–353. [\[CrossRef\]](#)
13. Nawi, M.A.; Zain, S.M. Enhancing the surface properties of the immobilized Degussa P-25 TiO₂ for the efficient photocatalytic removal of methylene blue from aqueous solution. *Appl. Surf. Sci.* **2012**, *258*, 6148–6157. [\[CrossRef\]](#)
14. Moridi, A.; Hassani-Gangaraj, S.M.; Guagliano, M.; Dao, M. Cold spray coating: Review of material systems and future perspectives. *Surf. Eng.* **2014**, *36*, 369–395. [\[CrossRef\]](#)
15. Gardon, M.; Guilemany, J.M. Milestones in Functional Titanium Dioxide Thermal Spray Coatings: A Review. *J. Therm. Spray Technol.* **2014**, *23*, 595. [\[CrossRef\]](#)
16. Winnicki, M. Advanced functional metal-ceramic and ceramic coatings deposited by low-pressure cold spraying: A review. *Coatings* **2021**, *11*, 1044. [\[CrossRef\]](#)
17. Liu, J.; Liu, Y.; Suo, X.; Latka, L.; Małachowski, A.; Lu, D.; Li, H. Cold Spray Construction of Nanostructured Titania Coatings for Photocatalytic Applications. *J. Therm. Spray Technol.* **2021**, *30*, 918–925. [\[CrossRef\]](#)
18. Rokni, M.R.; Nutt, S.R.; Widener, C.A.; Champagne, V.K.; Hrabe, R.H. Review of Relationship Between Particle Deformation, Coating Microstructure, and Properties in High-Pressure Cold Spray. *J. Therm. Spray Technol.* **2017**, *26*, 1308–1355. [\[CrossRef\]](#)
19. Yamada, M.; Isago, H.; Nakano, H.; Fukumoto, M. Cold spraying of TiO₂ photocatalyst coating with nitrogen process gas. *J. Therm. Spray Technol.* **2010**, *19*, 1218–1223. [\[CrossRef\]](#)

20. Omar, N.; Yamada, M.; Yasui, T.; Fukumoto, M. Bonding Mechanism of Cold-Sprayed TiO₂ Coatings on Copper and Aluminum Substrates. *Coatings* **2021**, *11*, 1349. [\[CrossRef\]](#)
21. Chakrabarty, R.; Song, J. Numerical modeling of fracture in ceramic micro-particles and insights on ceramic retention during composite cold spray process. *Surf. Coat. Technol.* **2021**, *409*, 126830. [\[CrossRef\]](#)
22. Kliemann, J.O.; Gutzmann, H.; Gärtner, F.; Hübner, H.; Borchers, C.; Klassen, T. Formation of cold-sprayed ceramic titanium dioxide layers on metal surfaces. *J. Therm. Spray Technol.* **2011**, *20*, 292–298. [\[CrossRef\]](#)
23. Baszczuk, A.; Jasiorski, M.; Winnicki, M. Low-Temperature Transformation of Amorphous Sol–Gel TiO₂ Powder to Anatase during Cold Spray Deposition. *J. Therm. Spray Technol.* **2018**, *27*, 1551–1562. [\[CrossRef\]](#)
24. Seremak, W.; Baszczuk, A.; Jasiorski, M.; Gibas, A.; Winnicki, M. Photocatalytic Activity Enhancement of Low-pressure Cold-Sprayed TiO₂ Coatings Induced by Long-term Water Vapor Exposure. *J. Therm. Spray Technol.* **2021**, *30*, 1827–1836. [\[CrossRef\]](#)
25. Schmidt, T.; Gärtner, F.; Assadi, H.; Kreye, H. Development of a generalized parameter window for cold spray deposition. *Acta Mater.* **2006**, *54*, 729–742. [\[CrossRef\]](#)
26. Champagne, V.K.; Helfritsch, D.J.; Dinavahi, S.P.G.; Leyman, P.F. Theoretical and Experimental Particle Velocity in Cold Spray. *J. Therm. Spray Technol.* **2011**, *20*, 425–431. [\[CrossRef\]](#)
27. Yin, S.; Suo, X.; Liao, H.; Guo, Z.; Wang, X. Significant influence of carrier gas temperature during the cold spray process. *Surf. Eng.* **2014**, *30*, 443–450. [\[CrossRef\]](#)
28. Akpan, U.G.; Hameed, B.H. The advancements in sol-gel method of doped-TiO₂ photocatalysts. *Appl. Catal. A Gen.* **2010**, *375*, 1–11. [\[CrossRef\]](#)
29. Rajaramanan, T.; Kumara, G.R.A.; Velauthapillai, D.; Ravirajan, P.; Senthilnathanan, M. Ni/N co-doped P25 TiO₂ photoelectrodes for efficient Dye-Sensitized Solar Cells. *Mater. Sci. Semicond. Process* **2021**, *135*, 106062. [\[CrossRef\]](#)
30. Chang, C.Y.; Wu, N.L. Process analysis on photocatalyzed dye decomposition for water treatment with TiO₂-coated rotating disk reactor. *Ind. Eng. Chem. Res.* **2010**, *49*, 12173–12179. [\[CrossRef\]](#)
31. Wang, T.; Zhang, Y.; Pan, J.; Li, B.; Wu, L.; Jiang, B. Hydrothermal reduction of commercial P25 photocatalysts to expand their visible-light response and enhance their performance for photodegrading phenol in high-salinity wastewater. *Appl. Surf. Sci.* **2019**, *480*, 896–904. [\[CrossRef\]](#)
32. Janczarek, M.; Kowalska, E. Defective Dopant-Free TiO₂ as an Efficient Visible Light-Active Photocatalyst. *Catalysts* **2021**, *11*, 978. [\[CrossRef\]](#)
33. Su, J.; Zou, X.; Chen, J.S. Self-modification of titanium dioxide materials by Ti³⁺ and/or oxygen vacancies: New insights into defect chemistry of metal oxides. *RSC Adv.* **2014**, *4*, 13979–13988. [\[CrossRef\]](#)
34. Chen, X.; Liu, L.; Huang, F. Black titanium dioxide (TiO₂) nanomaterials. *Chem. Soc. Rev.* **2015**, *44*, 1861–1885. [\[CrossRef\]](#)
35. Wu, Q.; Cheng, Y.; Huang, F.; Li, X.; Cui, X.; Xu, J.; Wang, Y. In-situ creating elastic lattice O–O bonds over semicrystalline yellow TiO₂ nanoparticles for significantly enhanced photocatalytic H₂ production. *J. Hazard. Mater.* **2019**, *374*, 287–295. [\[CrossRef\]](#) [\[PubMed\]](#)
36. Randorn, C.; Irvine, J.T.S.; Robertson, P. Synthesis of visible-light-activated yellow amorphous TiO₂ photocatalyst. *Int. J. Photoenergy* **2008**, *2008*, 426872. [\[CrossRef\]](#)
37. Wang, Y.; Ganeshraja, A.S.; Jin, C.; Zhu, K.; Wang, J. One-pot synthesis visible-light-active TiO₂ photocatalysts at low temperature by peroxotitanium complex. *J. Alloys Compd.* **2018**, *765*, 551–559. [\[CrossRef\]](#)
38. Zou, J.; Gao, J.; Xie, F. An amorphous TiO₂ sol sensitized with H₂O₂ with the enhancement of photocatalytic activity. *J. Alloys Compd.* **2010**, *497*, 420–427. [\[CrossRef\]](#)
39. Lee, J.W.; Jeong, R.H.; Kim, D.I.; Yu, J.-H.; Nam, S.-H.; Boo, J.-H. Facile synthesis of amorphous Ti-peroxo complex for photocatalytic activity under visible-light irradiation. *J. Clean. Prod.* **2019**, *239*, 118013. [\[CrossRef\]](#)
40. Vijayarangamuthu, K.; Youn, J.S.; Park, C.M.; Jeon, K.J. Facile synthesis of core-shell-structured rutile TiO₂ with enhanced photocatalytic properties. *Catal. Today* **2020**, *347*, 18–22. [\[CrossRef\]](#)
41. Han, E.; Vijayarangamuthu, K.; Youn, J.-S.; Park, Y.K.; Jung, S.C.; Jeon, K.J. Degussa P25 TiO₂ modified with H₂O₂ under microwave treatment to enhance photocatalytic properties. *Catal. Today* **2018**, *303*, 305–312. [\[CrossRef\]](#)
42. Hirakawa, T.; Yawata, K.; Nosaka, Y. Photocatalytic reactivity for O₂– and OH radical formation in anatase and rutile TiO₂ suspension as the effect of H₂O₂ addition. *Appl. Catal. A Gen.* **2007**, *325*, 105–111. [\[CrossRef\]](#)
43. Gehrke, S.A.; Taschieri, S.; Del Fabbro, M.; Coelho, P.G. Positive Biomechanical Effects of Titanium Oxide for Sandblasting Implant Surface as an Alternative to Aluminium Oxide. *J. Oral Implantol.* **2015**, *41*, 515–522. [\[CrossRef\]](#) [\[PubMed\]](#)
44. Ahmad, R.; Lee, C.S.; Kim, J.H.; Kim, J. Partially coated TiO₂ on Al₂O₃ membrane for high water flux and photodegradation by novel filtration strategy in photocatalytic membrane reactors. *Chem. Eng. Res. Des.* **2020**, *163*, 138–148. [\[CrossRef\]](#)
45. Hanft, D.; Exner, J.; Schubert, M.; Stöcker, T.; Fuierer, P.; Moos, R. An overview of the Aerosol Deposition method: Process fundamentals and new trends in materials applications. *J. Ceram. Sci. Technol.* **2015**, *6*, 147–181. [\[CrossRef\]](#)
46. Özdemir, O.Ç.; Conahan, J.M.; Müftü, S. Particle Velocimetry, CFD, and the Role of Particle Sphericity in Cold Spray. *Coatings* **2020**, *10*, 1254. [\[CrossRef\]](#)
47. Kang, X.; Berberidou, C.; Galeckas, A.; Bazioti, C.; Sagstuen, E.; Norby, T.; Poullos, I.; Chatzidakis, A. Visible Light Driven Photocatalytic Decolorization and Disinfection of Water Employing Reduced TiO₂ Nanopowders. *Catalysts* **2021**, *11*, 228. [\[CrossRef\]](#)

48. Verma, R.; Samdarshi, S.K.; Singh, J. Hexagonal Ceria Located at the Interface of Anatase/Rutile TiO₂ Superstructure Optimized for High Activity under Combined UV and Visible-Light Irradiation. *J. Phys. Chem. C* **2015**, *119*, 23899–23909. [[CrossRef](#)]
49. Choudhury, B.; Dey, M.; Choudhury, A. Defect generation, d-d transition, and bandgap reduction in Cu-doped TiO₂ nanoparticles. *Int. Nano Lett.* **2013**, *3*, 25. [[CrossRef](#)]
50. Balachandran, U.; Eror, N.G. Raman Spectra of Titanium Dioxide. *J. Solid State Chem.* **1982**, *42*, 276–282. [[CrossRef](#)]
51. Bi, X.; Du, G.; Sun, D.; Zhang, M.; Yu, Y.; Su, Q.; Ding, S.; Xu, B. Room-temperature synthesis of yellow TiO₂ nanoparticles with enhanced photocatalytic properties. *Appl. Surf. Sci.* **2020**, *511*, 145617. [[CrossRef](#)]
52. Tengvall, P.; Vikinge, T.P.; Lundström, I.; Liedberg, B. FT-Raman Spectroscopic Studies of the Degradation of Titanium Peroxy Gels Made from Metallic Titanium and Hydrogen Peroxide. *J. Colloid Interface Sci.* **1993**, *160*, 10–15. [[CrossRef](#)]
53. Patel, C.C.; Jere, G.V. Nature, stability and bonding of the peroxy group in peroxy titanium compounds. *J. Inorg. Nucl. Chem.* **1963**, *25*, 1155–1159. [[CrossRef](#)]
54. Gyulavári, T.; Veréb, G.; Pap, Z.; Dombi, A.; Hernádi, K. Associating low crystallinity with peroxo groups for enhanced visible light active photocatalysts. *Catal. Today* **2018**, *313*, 231–238. [[CrossRef](#)]
55. Ren, N.; Li, R.; Chen, L.; Wang, G.; Liu, D.; Wang, Y.; Zheng, L.; Tang, W.; Yu, X.; Jiang, H.; et al. In situ construction of a titanate–silver nanoparticle–titanate sandwich nanostructure on a metallic titanium surface for bacteriostatic and biocompatible implants. *J. Mater. Chem.* **2012**, *22*, 19151. [[CrossRef](#)]
56. Cramer, C.J.; Tolman, W.B.; Theopold, K.H.; Rheingold, A.L. Variable character of O—O and M—O bonding in side-on (η^2) 1:1 metal complexes of O₂. *Proc. Natl. Acad. Sci. USA* **2003**, *100*, 3635–3640. [[CrossRef](#)]
57. Chaudhuri, M.K.; Das, B. Direct synthesis of alkali-metal and ammonium pentafluoroperoxytitanates(IV), A₃[Ti(O₂)F₅], and first synthesis and structural assessment of alkali-metal and ammonium difluorodiperoxytitanates(IV), A₂[Ti(O₂)₂F₂]. *Inorg. Chem.* **1986**, *25*, 168–170. [[CrossRef](#)]
58. Eysel, H.H.; Thym, S. RAMAN Spectra of Peroxides. *ZAAC J. Inorg. Gen. Chem.* **1975**, *411*, 97–102. [[CrossRef](#)]
59. Levanov, A.V.; Sakharov, D.V.; Dashkova, A.V.; Antipenko, E.E.; Lunin, V.V. Synthesis of Hydrogen Polyoxides H₂O₄ and H₂O₃ and Their Characterization by Raman Spectroscopy. *Eur. J. Inorg. Chem.* **2011**, *2011*, 5144–5150. [[CrossRef](#)]
60. Šćepanović, M.; Grujić-Brojčin, M.; Abramović, B.; Golubović, A. Structural, morphological, and optical study of titania-based nanopowders suitable for photocatalytic applications. *J. Phys. Conf. Ser.* **2017**, *794*, 012003. [[CrossRef](#)]
61. Kim, H.-M.; Miyaji, F.; Kokubo, T.; Nakamura, T. Apatite-Forming Ability of Alkali-Treated Ti Metal in Body Environment. *J. Ceram. Soc. Jpn.* **1997**, *105*, 111–116. [[CrossRef](#)]
62. Hardcastle, F. Raman Spectroscopy of Titania (TiO₂) Nanotubular Water-Splitting Catalysts. *J. Ark. Acad. Sci.* **2011**, *65*, 43–48.
63. Savinkina, E.V.; Obolenskaya, L.N.; Kuzmicheva, G.M.; Kabachkov, E.N.; Gainanova, A.A.; Zubavichus, Y.V.; Murzin, V.Y.; Sadovskaya, N.V. Introduction of peroxo groups into titania: Preparation, characterization and properties of the new peroxo-containing phase. *CrystEngComm* **2015**, *17*, 7113–7123. [[CrossRef](#)]
64. Gardner, R.A. Intermediates in catalysis, spectroscopy and electron distribution. Part I. Hydrogen peroxide. *J. Mol. Catal.* **1986**, *34*, 85–94. [[CrossRef](#)]
65. Hayyan, M.; Hashim, M.A.; AlNashef, I.M. Superoxide Ion: Generation and Chemical Implications. *Chem. Rev.* **2016**, *116*, 3029–3085. [[CrossRef](#)] [[PubMed](#)]



H₂O₂-sensitized titania with activity under visible light and in the dark

Anna Gibas^{a,*}, Agnieszka Baszczuk^a, Irena Jacukowicz-Sobala^b, Agnieszka Ciechanowska^b, Marek Jasiorski^a, Ewa Dworniczek^c, Alicja Seniuk^c, Agnieszka Lewińska^d

^a Department of Mechanics, Materials and Biomedical Engineering, Wrocław University of Science and Technology, 25 Smoluchowskiego Street, Wrocław 50-370, Poland

^b Department of Chemical Technology, Wrocław University of Economics and Business, Komandorska St., Wrocław 53-345, Poland

^c Department of Microbiology, Faculty of Medicine, Wrocław Medical University, Wrocław 50-368, Poland

^d Faculty of Chemistry, University of Wrocław, 14 Joliot-Curie Street, Wrocław 50-383, Poland

ARTICLE INFO

Keywords:

Yellow TiO₂
Hydrogen peroxide
Peroxo-titanium complexes
Oxidation
Dark
Catalysis

ABSTRACT

The development of visible-light photoactive materials decomposing pollutants and removing bacteria is a frequent motivation for scientific research. However, the reliance on light to sustain the degradation process restricts the practical application of photocatalysts. In this paper, titania was sensitized with H₂O₂ to overcome this problem and exhibit photocatalytic and dark activity. Efficiency of degradation of standard pollutant (methylene blue) and antibacterial properties (tested on two strains of bacteria: *Enterococcus faecalis* and *Escherichia coli*) were assessed. The comprehensive effect of this material is a result of the peroxide-assisted sol-gel method, without heat treatment, which allows obtaining titanium dioxide with hydroxy and adoxygen groups on the surface and in the volume. The presence of the peroxo and superoxo groups was confirmed using Raman, IR and EPR spectroscopies. The thermal stability of the adoxygen groups was analysed by TG/DSC analysis. X-ray diffraction indicated the formation of an amorphous layered structure. The Tauc plot revealed midgap states which reduced the band gaps towards visible light. The H₂O₂-sensitized TiO₂ was characterized by negative surface potential (pH_{PZC}=3.2) which improved adsorption. The study provides insight for the development of self-cleaning and antibacterial surfaces.

1. Introduction

Titanium dioxide, a versatile semiconductor known for its low cost, high chemical stability and photocatalytic activity, finds applications in diverse fields such as photocatalysis, dye-sensitization, Li-ion batteries, solar cells, self-cleaning surfaces and medical devices [1]. Despite being the most common photocatalyst, its photocatalytic performance faces challenges due to a large band gap (3.0–3.2 eV, requiring irradiation with ultraviolet light) and the rapid recombination of photoexcited electron-hole pairs. To unlock its visible-light-driven potential and reduce the recombination rate, researchers have investigated innovative modifications, including doping TiO₂ with metals, especially noble ones; and nonmetals, as well as employing dual cocatalysts [1,2]. Within the group of doping strategies, a unique dopant-free approach stands out - self-doping using benign oxidants (e.g., H₂O₂ and O₂). By treating TiO₂ with hydrogen peroxide it is possible to create new surface titanium-oxygen groups, such as peroxo-complexes (Ti O O) [3–7]. Peroxide species, which appear yellow to the naked eye, are great

precursors for hydroxy groups, while simultaneously extending the light absorption of H₂O₂-treated TiO₂ (2.2 eV), thereby reinforcing its effective visible-light-driven photocatalytic properties [5,6]. This type of H₂O₂-sensitized Ti-based oxides have recently been shown to exhibit photocatalytic activity in the reactions involved in: degradation of organic pollutants such as methylene blue (MB) [7–10], rhodamine B [5, 11–14], or sulforhodamine B [15] or other organic compounds [16]; water splitting [5]; reduction of carbon dioxide [17]; formaldehyde production [15,18]; and hydrogen production [6,7].

The sensitization of Ti-based oxides with H₂O₂ to obtain visible light activity may proceed in two ways: via top-down modification [7,9,12, 13,15,18] or bottom-up synthesis [5,6,8,10,11,14,16,17]. Irrespective of the approach to H₂O₂ sensitization of TiO₂ synthesis, thermal treatment is used to provide intended phase composition on the basis of the assumption that anatase and rutile are considered superior polymorphs for photocatalysis and sensitization with H₂O₂ provides certain defects upon heating [8,10,17]. The top-down approach consists of simple soaking of crystalline TiO₂ in the H₂O₂ solution inducing massive

* Corresponding author.

E-mail address: anna.gibas@pwr.edu.pl (A. Gibas).

<https://doi.org/10.1016/j.jece.2024.113975>

Received 10 June 2024; Received in revised form 25 August 2024; Accepted 26 August 2024

Available online 30 August 2024

2213-3437/© 2024 The Author(s). Published by Elsevier Ltd. This is an open access article under the CC BY license (<http://creativecommons.org/licenses/by/4.0/>).

surface hydroxylation [7,12,13,15] and the reduction of crystallite size via titania dissolution [7,12,15], reaggregation [12,15] or partial surface amorphization [7,13] upon sensitization. Meanwhile, the bottom-up approach facilitates comprehensive defect engineering at every stage of the newly formed amorphous phase (in the whole volume) [6,11]. The positioning of O–O groups in the hydrated titania hampers crystallisation and arranges the newly synthesised atoms into layers [5, 14,19,20]. In both syntheses, the surface of the TiO₂ modified with H₂O₂ may be highly disordered, containing oxygen vacancies and titanium in various oxidation states (Ti⁴⁺, Ti³⁺, Ti²⁺) [8,11], as well as different types of oxygen-rich groups (Ti–O–O, Ti–O–OH, Ti–O–O–Ti, and triangular TiO₂) and their concentrations [8,11,21]. In top-down processes, peroxy groups are predominantly generated on the surface of the material [7,12,13], whereas in the bottom-up strategy [11], based on the so-called peroxide-assisted sol-gel method, peroxy groups appear in the whole volume and are part of the formed, water-soluble amorphous peroxotitanium complex [5,11,19,21]. It was also reported that alongside peroxy complexes, stable superoxy radicals (O₂^{•−}) that may initiate oxidation reactions [6,22] can also be found in bottom-up materials [6]. Peroxy and superoxy complexes, which together can be called adoxygen groups, exhibit thermal sensitivity [16,23] and frequently decompose when TiO₂ is annealed. Low-temperature drying causes the dissociation of hydroperoxy groups (Ti–O–OH) to the form of hydroxyl groups (–OH) [7,13]. Meanwhile, high temperature treatment of anatase hinders rutile formation, reduces surface area and pore volume [9,10] or in the rutile-containing samples induces the formation of defects, such as Ti³⁺ and oxygen vacancies [8,12]. Although an increase in visible light activity can be observed despite the elimination of oxygen-rich groups [7–10,12,13], it would be interesting to retain the amorphous peroxotitanate gel with all thermal-sensitive groups and explore its photocatalytic properties.

The benefits of the elimination of the thermal treatment for H₂O₂-sensitized TiO₂ can be observed in photocatalytic systems for the degradation of organic dyes, where TiO₂ is used as a heterogeneous catalyst and H₂O₂ as an oxidant [24–27]. Following the pattern of top-down syntheses, the contact of TiO₂ powders with the H₂O₂ solution induces the formation of adoxygen groups on the surface of the titania [26,28]. Interestingly, the oxygen-rich groups also prove advantageous for the non-light-driven catalytic degradation of organic contaminants [27–31]. The causes of the phenomenon called "dark catalysis" are, however, ambiguous. Attempts to explain the activity in the dark most often lead to the conclusion that the enhancement of the TiO₂ catalysis in the dark upon H₂O₂ addition induces the above-mentioned changes in the surface of the TiO₂ particles, thus enabling the formation of free radicals including HO[•], O₂^{•−} and HOO[•] [25,27]. Some authors also emphasise the role in the process of surface defects, such as Ti³⁺ or oxygen vacancies [30,31]. According to Wiedmer et al. [31], the mechanism of dark catalysis is a Fenton-reaction-like superoxide-driven process and must involve Ti³⁺/Ti⁴⁺, where the Ti³⁺ donates electrons to the H₂O₂ and generates O₂^{•−}/HOO[•] and HO[•] in the process. Meanwhile, Wu et al. [30] suggest that activity in the dark is associated with internal defects in the TiO₂ structure - single-electron-trapped oxygen vacancy. The role of the vacancy is to activate H₂O₂ in the dark by a direct contribution of electrons, which in the process form both O₂^{•−}/HOO[•] and HO[•] radicals [30]. Apart from catalysing reactions, the generation of radicals within such systems also demonstrates bactericidal properties [32]. Additionally, some other works draw attention to the higher dark activity of amorphous hydrated titanium dioxide compared to its crystalline version, commercially available P25 [29].

The process of sensitizing titanium dioxide with hydrogen peroxide leads to several physicochemical changes that are interesting from the point of view of its catalytic activity. The various sensitization effects with details of Ti-based oxides preparation together with the activity investigated are summarized in the [Supplementary Materials 2](#). The most comprehensive approach for the formation of oxygen-rich groups seems to be bottom-up synthesis, in which adoxygen groups are

generated in the whole volume of hydrated titanium dioxide. Given the thermal sensitivity of both peroxy and superoxy complexes, this paper aims to assure their presence and stability after powder drying by using the peroxide-assisted sol-gel method to prepare TiO₂ without subsequent high temperature or pressure post-treatments. Simultaneously, lack of annealing sustains the produced powder in an amorphous state, which in combination with low-temperature low-energy coating methods can be beneficial for depositing yellow self-cleaning surfaces [33,34]. In the present study, we intend to recognise the role of the chemical composition changes introduced by H₂O₂ treatment in both photocatalytic and non-light-driven catalytic processes of methylene blue degradation. Finally, to fully display the versatility of H₂O₂-sensitized TiO₂, we also tested its antimicrobial activity against the opportunistic bacteria *Enterococcus faecalis* and *Escherichia coli*. The visible active photocatalyst, which also generates oxidative stress in the dark, is a promising material that could be deemed to follow a secure and environmentally friendly self-cleaning and antibacterial strategy.

2. Materials and methods

2.1. Synthesis

In a single synthesis, the reagents were employed as follows: 1 mL of nitric acid (HNO₃, 65 %, Chempur, Karlsruhe, Germany), 100 mL of demineralized water, 10 mL of titanium (IV) isopropoxide (Ti[OCH(CH₃)₂]₄, 97 %, Sigma-Aldrich, St. Louis, MO, USA) and 20 mL of hydrogen peroxide (H₂O₂, 30 %, Stanlab, Ltd., Lubin, Poland). No expensive instruments, specialized atmospheres or intricate glassware are needed for any step of the synthesis. The one-pot synthesis was divided into two subsequent steps: hydrolysis of the Ti-precursor, and oxidation of Ti(OH)₄ precipitates developing peroxy complexes (reaction 1). The first step included adding a dropwise titanium precursor to the water-acid solution to receive an opaque white mixture. Then, the H₂O₂ was added dropwise, immediately changing the colour of the mixture to dark orange.



The specific volumes of the reactants were selected based on the [6] to provide the amorphous structure of the powder with adoxygen groups (peroxy and superoxy). After drying, the sample was sieved through 32 and 63 μm sieves to obtain powder that can be used for cold spraying [35]. The particle size distribution can be found in the [Supplementary Materials \(Figure S1\)](#). Based on 34 quadruple syntheses, the average single TiO₂-yellow portion weighted 3.66±0.16 g, with the sieved fraction constituting approximately 55 % of the total. The repeatability control was assured using Raman spectroscopy and XRD. The as-synthesized sample is called TiO₂-yellow because of the coloration of the powder. For comparison, two powders are used: the self-synthesized powder without the addition of H₂O₂ (TiO₂-white), and the commercially available TiO₂ (P25).

2.2. Photocatalytic activity testing

The photocatalytic activity was evaluated based on methylene blue (analytical grade, Eurochem BGD Sp. z o.o., Poland) degradation in an aqueous solution, conducted in a modified photocatalytic reactor TOPT-V 8-parallel sample type (Toption Instruments Co., China) equipped with sample quartz vessels and magnetic stirrers. LEDs were used as a light source – Thorlabs M455L4 (visible light range with maximum irradiation at 455 nm) and Thorlabs M365L3 (UV light range with maximum irradiation at 365 nm) with controllable irradiance which was set at the same value - 1.62 mW/cm² (measured with Thorlabs optical power monitor and standard photodiode power sensor S120VC). The spectral characteristics of the lamps is included in the [Supplementary Materials \(Figure S4\)](#). Due to the observed activity of the powder in

the dark, the tests were conducted without any conditioning period. After optimisation of a powder dose in the range 0.25–2.00 g/L (Figure S2), further photocatalytic tests were conducted using a dose of 0.5 g/L, in detail a 50 mg sample was treated with 100 mL of MB solution with a concentration 3.6 mg/L or 16.0 mg/L, under different conditions – dark, VIS light and UV light illumination. All tests were conducted without pH correction (at pH = 3.6) except the studies of the pH influence. In this case, the MB solutions were prepared using an HCl solution with a concentration of 5.0 mM, an NaOH solution with a concentration of 5.0 mM, or a citrate-phosphate buffer with a pH = 7.6. The solution samples were collected after time intervals (from 0.5 to 12 h, in the kinetic regime or equilibrium regime). The powders were filtered from the solution using a syringe filter with a pore size of 0.2 µm. The residual MB concentration with UV-Vis spectrophotometer (Specord 210 Plus, Analytik Jena, Jena, Germany) at $k_{\max} = 664$ nm (the detection limit was 0.25 mg/L with a relatively standard deviation ≤ 6 %). The efficiency of MB degradation in the equilibrium regime (after 12 h duration) was also confirmed by total organic carbon (TOC) determination, conducted in a certified laboratory using an Enviro TOC analyser (Elementar, Germany). The samples in the experiments conducted under an inert atmosphere were prepared and collected in a Siccio PC ESD glove box with a transfer chamber under a nitrogen atmosphere. All experiments were carried out in duplicate.

2.3. Physicochemical characterization

The crystal structure of the materials was examined using an Ultima IV X-ray diffractometer (Rigaku, Tokyo, Japan), equipped with a CuK α source ($\lambda = 1.54056$ Å) for 2θ in the range from 5° to 75° in steps of 0.05° and 3 s for each measurement point. The morphologies and microstructures were characterized with a TEM microscope FEI Tecnai G2 20 X-TWIN (FEI, Hillsboro, USA) operating at 200 kV along with associated selected area diffraction patterns. The particle size distribution (PSD) was measured with HELOS H3776, RODOS/T4/R4 laser diffraction modules and a VIBRI dispersion unit (Sympatec GmbH, Germany). The statistical analysis of the obtained PSD results proceeded automatically using PAQXOS 3.1 software following the Fraunhofer procedure (ISO 13320:2009). Thermogravimetric analysis (TG) and differential scanning calorimetry (DSC) were performed using an STA 449 F1 Jupiter instrument (Netzsch, Germany) from room temperature (RT) to 800°C in an Al_2O_3 crucible in a nitrogen atmosphere at a heating rate of 10 K min^{-1} . The diffuse reflectance spectra were measured using a UV-VIS spectrophotometer equipped with a 75 mm integrating sphere (Specord 210, Analytik Jena, Jena, Germany) in the range from 200 to 800 nm with a Spectralon® as the reference material. The recorded reflectance (R) was recalculated into the absorption coefficient ($F(R)$) using the Kubelka–Munk function (Eq. 2), and a Tauc plot ($F(R)h\nu^{0.5}$ vs. $h\nu$) was used to determine the band gap energies.

$$F(R) = (1 - R)^2 / 2R \quad (2)$$

The Raman spectra were collected using a Raman spectrophotometer LabRam HR800 (Horiba/Jobin-Yvon, Kyoto, Japan) within the spectral range from 50 to 1200 cm^{-1} upon an argon 50 mW laser excited at 514.55 nm. Mid infrared (MIR) spectra were measured on a Bruker VERTEX 70 V spectrometer equipped with a diamond ATR accessory and air-cooled DTGS detector.

The EPR spectra were recorded at room temperature using an Elexsys 500 CW-EPR (Bruker, Billerica, USA) spectrometer operating at the X-band frequency ($\sim 9.7\text{ GHz}$), and equipped with a frequency counter (E41 FC) and an NMR teslameter (ER 036TM). The spectra were obtained with a modulation frequency of 100 kHz, microwave power set at 10 mW, modulation amplitude of 0.5 G, a time constant of 40 ms, and a conversion time of 160 ms. The first derivative of the absorption power was recorded as a function of the magnetic field value. Subsequent analysis of the EPR spectra was performed using the WinEPR software

package, version 1.26b.

X-ray photoelectron spectroscopy (XPS) investigations were conducted with a multi-chamber ultrahigh vacuum (UHV) system from PREVAC (Rogów, Poland) using a hemispherical Scienta R4000 electron analyser. Complementary equipment included Scienta SAX-100 X-ray sources (Al-K α , 1486.6 eV) equipped with a Monochromator VG Scienta XM 780. Instrument base pressure was kept to under 10^{-8} mbar. The spectra processing and composition calculations were carried out with CasaXPS v. 2.3.25 PR1 software.

The point of zero charge (pH_{PZC}) was determined by the drift method [36]. The 0.05 g samples were treated with 100 mL of 0.1 M KCl solution with a different initial pH (from 1.1 to 9.0) adjusted using a 0.1 M HCl or KOH solution. After 8 hours the final pH of the solution was measured. From the plot of the initial pH versus ΔpH , the point at which the curve crossed the pH axis determined the pH_{PZC} of the powder.

2.4. Antimicrobial activity testing

Bacterial strains of *Enterococcus faecalis* (*E. faecalis*) VRE1 and *Escherichia coli* (*E. coli*) PA170 were used respectively as representative Gram-positive and Gram-negative microorganisms to measure the antimicrobial properties of TiO_2 -yellow and P25. The bacterial suspensions (1.0×10^6 CFU/mL; colony forming unit per one millilitre) were mixed with TiO_2 -yellow and P25 in 0.85 % NaCl to achieve final concentrations of 1500 µg/mL, 750 µg/mL, 375 µg/mL, 188 µg/mL, and 94 µg/mL. H_2O_2 suspensions with concentrations ranging from 1.88 % to 0.015 % were also tested in the dark. Before the test, the reaction suspension was continually stirred in the dark for 30 min at room temperature (RT) kept constant by using a cooling system (VIBRAX, OVAN VX43 E, Spain). Then, half of the samples, stirred and cooled in the same way, were exposed to solar-like (UV+VIS) illumination using a broad emission spectrum XENON lamp (70 W, 100 mW/cm 2 , OPTTEL, Poland) mounted perpendicular to the samples. After 60 min of XENON and DARK treatment, 100 µL aliquots of each reaction suspension were withdrawn and diluted and a 50 µL aliquot was spread onto Tryptic Soy agar (TSA, Biomaxima, Poland) plates. After 24–48 h incubation of the inoculated plates at 37°C , the number of colonies was counted. The bactericidal activity of TiO_2 -yellow and P25 was evaluated by comparing the value of \log_{10} CFU/mL. The data and conclusions were confirmed by at least 3 replicate experiments.

3. Results and discussion

3.1. Characterization of studied materials

The initial investigation of the properties of the H_2O_2 -sensitized sample (TiO_2 -yellow) involved analysis of the crystal structure, morphology, content of OH groups, and optical band gap. The obtained results were compared with the those for sample synthesized by the same method but without H_2O_2 -sensitization (TiO_2 -white) and the commercial P25 Degussa powder (P25).

First, the crystal structure of TiO_2 -yellow was measured and compared with TiO_2 -white and P25 (Fig. 1). The diffractogram of TiO_2 -yellow indicates an amorphous structure of the powder. Five broad humps in the pattern of TiO_2 -yellow indicate a preference for arrangement into anatase only. A similar level of amorphicity was detected in acid [6] and base-catalysed [18] syntheses of H_2O_2 -sensitized powders. Without H_2O_2 addition, acidic reaction conditions contribute to the formation of a mixed anatase-rutile structure [18]. No surprise then that the diffraction peaks of TiO_2 -white match well with the standard peaks of anatase and rutile. The broadening of TiO_2 -white peaks indicates a lower degree of crystallinity than in the case of the sharp peaks of P25.

The low-angle peak at $\sim 6.00^\circ$ in the diffractogram of TiO_2 -yellow indicates interlayer diffraction typical for titanates with layered structures [14,20]. The formation of titanates instead of titanium oxide are commonly observed in the peroxide-assisted sol-gel method, where

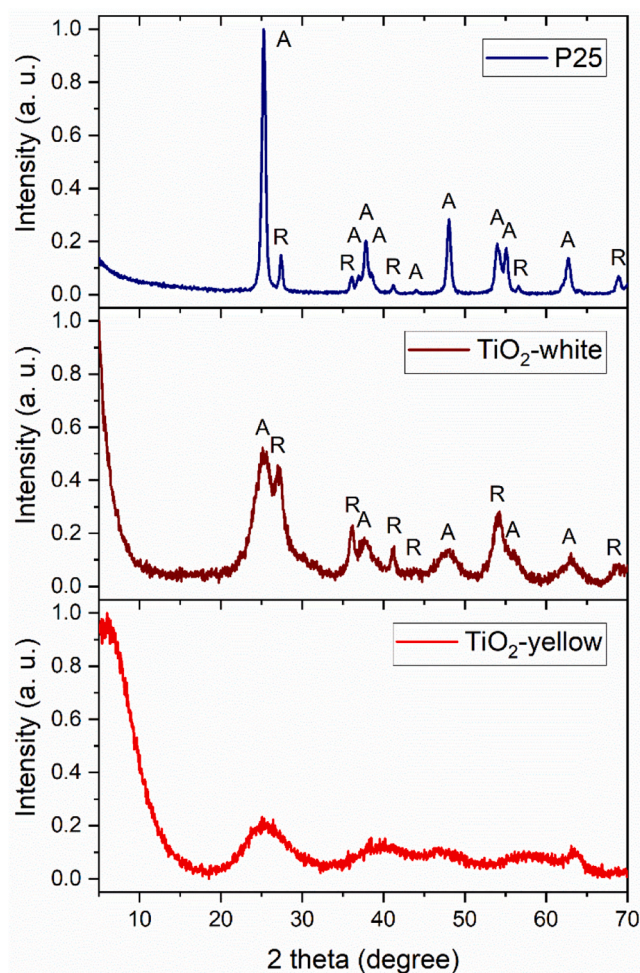


Fig. 1. XRD patterns of TiO₂-yellow (red), TiO₂-white (white) and P25 (navy). A and B denote anatase and rutile, respectively.

hydrogen peroxide is added to hydrolysed titanium precursors, such as Ti, TiH₂, TiOSO₄, TiCl₄, TiOCl₂ or alkoxides [18–20,37,38]. The low-angle characteristic diffraction peak indicates material composed of alternating layers built by TiO₆ octahedra that share corners and/or edges interrupted by ions (such as sodium or protons) [38,39] or water molecules [20]. For peroxide-assisted sol-gel method titanium dioxide, two-dimensional structural channels may be formed due to the peroxo groups separating them [5,14]. The formed peroxide groups block the progress of the formation of a three-dimensional oxide network, predisposing the formation of so-called peroxo-titanate complexes. When crystalline TiO₂ is treated with hydrogen peroxide, peroxo-titanate complexes do not form because H₂O₂ cannot penetrate the interior of the crystal [5].

The bright-field TEM image shows that nanosheets dominate the morphology of the TiO₂-yellow powder (Fig. 2a). Some of the sheets fold to irregular nanorolls of 60 nm diameter (Fig. 2b). The nanosheets are surrounded by ultrafine particles with an amorphous structure (Fig. 2c, Figure S2). The results of the XRD analysis correlate well with the TEM dark mode images (Figure S2), which confirms the low crystallinity of the nanosheets. The presence of differently oriented crystalline regions in a single nanoparticle is reflected as a variety of facets appearing at different positions around the diffraction ring (Figure S2). The very weak signal from selected-area diffraction (Fig. 2d) indicates d-spacing of the nanocrystal to be $5.49 \pm 0.25 \text{ nm}^{-1}$ which belongs to the inter-distance of the (101) crystal plane of the anatase (XRD peak position $24.23 \pm 1.12^\circ$) [40,41].

Because the TiO₂-yellow is partially amorphous and contains thermally sensitive adoxygen groups, its thermal stability was investigated next (Figure S3). For both samples, the weight loss proceeded up to 400 °C in two stages: evaporation of adsorbed water and the loss of structural water together with residual organic compounds, as both powders were synthesized using the wet chemical method. Taking into account the fact that the same amounts of reagents were used for both syntheses, the higher mass losses detected in TiO₂-yellow when compared to TiO₂-white in both regions show that the TiO₂-yellow sample has more hydroxy (OH) and adoxygen groups [15]. For the DSC curve of TiO₂-yellow, two thermal effects are detected; an endothermic peak at 130 °C and a broad exothermic peak centred at 257 °C, which was recognized as the start of anatase-to-rutile transformation. The peak of rutile crystallization is not detected in the measured range. The small exothermic effect may be the result of crystallisation counteracting with the removal of water and adoxygen groups. No exothermic peak in TiO₂-white is detected, indicating that the sample already consists of crystalline phases (anatase and rutile).

The mixed amorphous-crystalline structure enriched with hydroxy and adoxygen groups may indicate a change in optoelectric properties. For all samples in the ultraviolet range, almost all incident UV light is absorbed (Fig. 3). Despite similar mixed anatase-rutile phase composition, the band gap of TiO₂-white (3.0 eV) is only slightly narrower than P25, which may be explained by the hydroxylation of the TiO₂-white surface obtained on the sol-gel route. Such band gaps are typically obtained for H₂O₂-sensitized TiO₂ samples after heat treatment during which OOH groups are replaced with OH groups [7,9,10,13]. Meanwhile, a remarkable red-shift is observed for TiO₂-yellow. A large Urbach tail is present in the spectrum of the H₂O₂-sensitized sample (~2.3 eV) resulting from the presence of adoxygen groups [28] which, due to enhanced sub-band gap absorption, can contribute significantly to the absorption of photons with energies lower (longer wavelength of ~540 nm) than the optical gap (2.8 eV, which correlates with absorption of light with a wavelength shorter than 443 nm). Hence, compared to the adsorption edge of typical P25, the band gap of TiO₂-yellow is substantially narrowed by the formation of mid-band gap states. As other oxygen-rich titania samples had similar band gaps and exhibited photocatalytic properties in the visible light [5,6], our H₂O₂-sensitized titania (TiO₂-yellow) with a reduced band gap therefore remains promising for further studies.

3.2. Photocatalytic activity studies

Considering the large number of studies and developed standardised methods of determining photocatalytic activity (ISO 10678:2010), methylene blue was chosen as a model compound despite its other disadvantages such as absorption of the part of visible light spectrum mainly in the range of 600–700 nm. To overcome this obstacle as a source of irradiation, LEDs with a narrow irradiation spectrum and controllable irradiation energy was used. In consequence, the experiments in the UV and VIS range were conducted with the same irradiance - 1.62 mW/cm^2 - which is not possible when using cut-off filters. Simultaneously, the samples under VIS light conditions were irradiated with a source with maximum emission within the range of 420–500 nm, that is below the maximum absorption of MB (Figure S4). A control experiment with only methylene blue and no catalyst was conducted (Fig. 4), and no MB degradation was observed under visible light illumination, which precluded the self-photosensitization possibility.

Comparison of the physicochemical properties (crystalline structure and band gap) of commercial - P25, self-made TiO₂-white and H₂O₂-sensitized TiO₂-yellow suggest their different susceptibility to visible light and varied activation of a photocatalytic reaction. The preliminary test of methylene blue removal (Fig. 4) shows that under visible light irradiation, only the TiO₂-yellow exhibited a measurable reduction of MB concentration.

Photocatalytic tests of TiO₂-yellow (Fig. 5) were carried out under

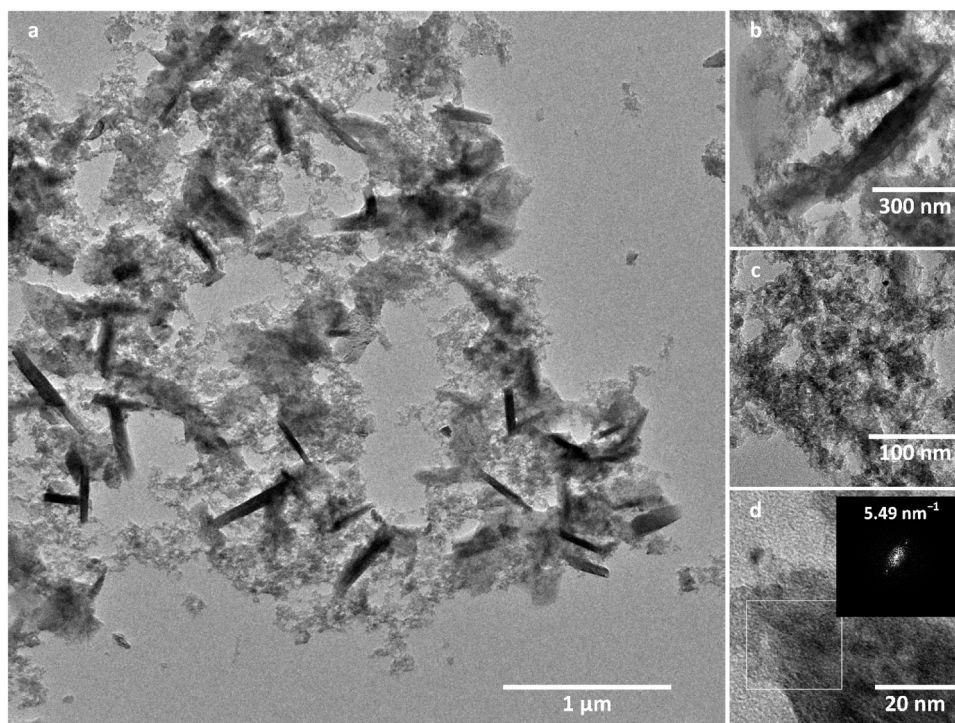


Fig. 2. (a,b,c) Bright field TEM image of TiO₂-yellow and (d) selected area diffraction.

Table 1

TG mass losses up to 800 °C for TiO₂-yellow and TiO₂-white, calculated based on Figure S3.

Sample	m _{loss} (50–130 °C) [%]	m _{loss} (130–400 °C) [%]	m _{loss} total [%]
TiO ₂ -white	8.3	10.8	19.1
TiO ₂ -yellow	13.5	13.2	26.5

the recommended concentration of MB at 3.6 mg/L [ISO 10678:2010], and an optimized photocatalyst dose of 0.5 g/L (optimization in the range 0.25–2.00 g/L is shown in Figure S5). The removal of MB without pH correction (Fig. 5a) was efficient since MB was completely removed, but the degradation time of 3 hours indicates a low rate of the process. The results for all samples (UV, VIS and DARK) are similar, which suggests that adsorption is the basic mechanism of methylene blue removal. A subsequent set of tests conducted at various pH conditions confirmed this assumption (Fig. 5b,c,d). Methylene blue, as a cationic dye, was adsorbed at a higher rate in alkaline conditions (Fig. 5d) when the surface of TiO₂-yellow (with p*H*_{pzc}=3.2) exhibited a negative charge which electrostatically attracted MB molecules – the adsorption

equilibrium was reached within 1 hour and the removal efficiency was between 75 % and 91 %. In contrast, at neutral (Fig. 5c) and acidic conditions (Fig. 5b), due to the lower rate, the process did not reach equilibrium within 4 hours. However, in acidified solutions, after 4 hours the process efficiency reached efficiency values of 78–88 %, comparable to alkaline solution efficiency. Interestingly, in each case, the efficiency of the tests conducted at a modified pH was lower than the efficiency of the process studied in the pure methylene blue solution without the addition of pH-correcting reagents such as HCl, NaOH and more significantly a citrate-phosphate buffer. Literature sources show that both citrate and phosphate anions show high complexing affinity towards surface hydroxy groups of metal oxides by forming strong surface complexes [42]. By competing and occupying part of the active sites on the TiO₂-yellow surface, these additives impeded methylene blue removal.

Adsorption is the first step in the heterogeneous photocatalytic process, therefore, in photocatalytic studies, before light irradiation, the surface of the photocatalyst requires surface preconditioning by adsorption of the removed compound on the surface under dark conditions. Usually, an equilibrium in this process is reached within 0.5–1.0 h [31,43], which is not reflected in our study. The slow but

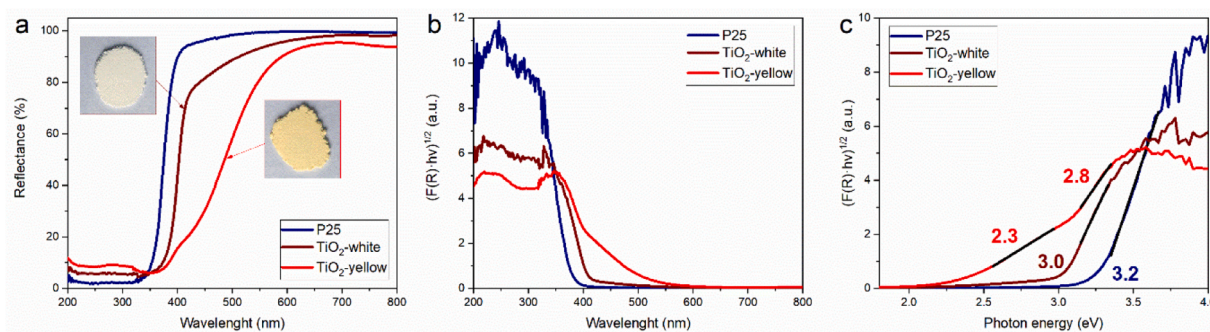


Fig. 3. (a) Diffuse reflectance spectra, (b) Kubelka–Munk function spectra with (c) the corresponding Tauc plot assuming indirect (allowed) transitions for TiO₂-yellow (red), TiO₂-white (white) and P25 (navy).

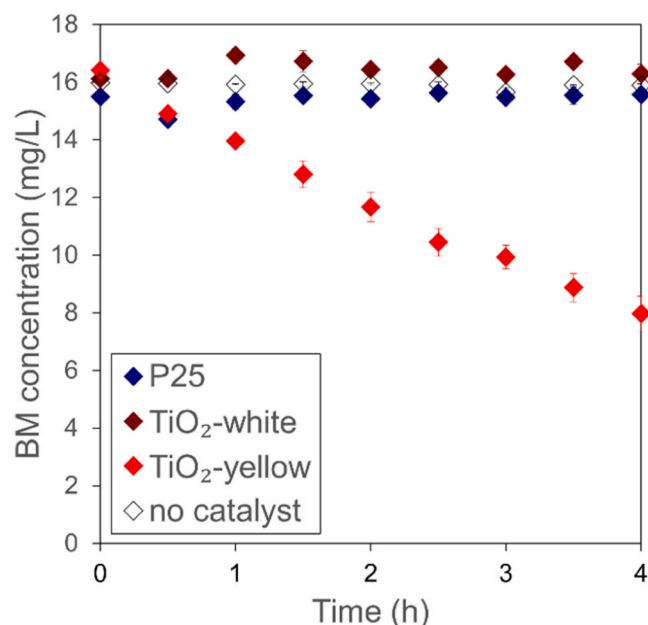


Fig. 4. Kinetics of methylene blue removal using TiO₂-yellow (red), TiO₂-white (white) and P25 (navy) and control experiments of methylene blue without catalyst (hollow black) under visible light (MB initial concentration 16.0 mg/L, photocatalyst dose 0.5 g/L, solution volume 100 mL, error bars represent the standard deviation of the mean).

ongoing MB removal suggests the adsorption of MB molecules on a restricted number of active centres, and their subsequent slow recovery by the adsorbed MB degradation. As this phenomenon is observed in both dark and light irradiation conditions, the next step of the study aimed to determine the maximal potential of TiO₂-yellow in the degradation of an excess of methylene blue with and without light activation over an extended reaction time.

To see the differences between the UV/VIS/ DARK conditions the initial concentration of the methylene blue was increased 5 times, and a longer reaction time was set (Fig. 6). The illumination improved the removal of MB in comparison to dark conditions. The efficiency of the process under visible light irradiation reached a value of 75 % after 8 hours, while in the dark this value only attained 36 % over the same process duration. Similarly to previous tests, after 8 hours the process was still in progress and had not reached equilibrium. After the test had run for 24 hours, no traces of MB were found in the VIS and UV-activated samples, and an efficiency of 80 % was recorded for dark conditions. These results may lead to different interesting conclusions. The slow progressive adsorption in the dark onto TiO₂-yellow was combined with the degradation of MB on the surface. Whereas the increase of the process efficiency by irradiation suggests switching on the photocatalytic mechanism of MB decomposition. However, in both cases, the rate of the process is severely limited by the restricted number of active centres and the slow decomposition reaction, leading to their restoration for adsorption of further MB molecules. The kinetic analysis to determine reaction order showed the good fit of the zero-order model:

$$C_t - C_0 = -kt \quad (3)$$

where C_0 represents the initial concentration, C_t - concentration at variable time t and k denotes reaction rate constant.

The plot of C_t versus time yielded a straight line with correlation coefficients from 0.980 to 0.998 (Fig. 6b). As Ollis [44] concluded, the zero-order behaviour of the photocatalytic reaction may result from the saturated surface of the photocatalyst in the organic reactant, in this case, methylene blue, which is in agreement with our previous considerations. The calculated reaction rate under dark, VIS, and UV

illumination increased from 0.014 to 0.027 and 0.024 (mg/L) min⁻¹, respectively. The visible light activity is better than reported by Li et al. [45] who also reported zero-order kinetics model. Other researchers investigating H₂O₂ sensitized Ti-based oxides claimed activity following rather pseudo-first-order kinetics [9–12,15,16,26].

To confirm our suppositions on the photocatalytic mechanism, another test was conducted with the same methylene blue concentrations and prolonged duration time – 12 h. In this experiment, only the final MB concentration was recorded using two different methods – spectrophotometric and total organic carbon (TOC) (Fig. 7a). VIS and UV light significantly increased the efficiency of MB removal. However, the efficiency of the process calculated from the two methods shows different values under illumination. Based on the spectrophotometric method, the MB concentration was decreased by 79 % while TOC was reduced by only 40 %. A similar relation was observed under UV light irradiation - 88 % and 50 % respectively, while in the dark both methods show a similar efficiency of 37 % and 36 % respectively. Supposedly, the process of photocatalytic methylene blue degradation also occurred in the solution leading to smaller organic compounds – products of incomplete MB decomposition. As a result, their presence was reflected in the elevated TOC values and also in the colour change since after the process the solution showed more purple shades (Fig. 7b). In contrast, the process in the dark solely occurred on the photocatalyst surface, however, due to slow kinetics its nature is still unknown.

3.3. Spectroscopic analyses for recognizing the mechanism of TiO₂-yellow activity

The modification of TiO₂ synthesis with H₂O₂ not only produced an amorphous hydroxylated titania with narrowed band gap providing activity in the visible light, but also led to additional dark activity likely beyond the adsorption. Spectroscopic investigations aimed to reveal the chemical composition of the TiO₂-yellow after methylene blue degradation under various conditions. The results were compared to those for the initial TiO₂-yellow, TiO₂-white and P25.

3.3.1. Raman and FTIR analyses

The Raman spectrum of TiO₂-white contains bands corresponding to the vibration's characteristic of anatase (159 cm⁻¹) and rutile (247, 452, 611 cm⁻¹) (Figure S6a). The spectrum of the TiO₂-yellow (Fig. 8a, Figure S6a) is completely different to typical TiO₂ spectra and does not contain any bands that could be attributed to anatase or rutile. Few researchers have obtained an identical TiO₂-yellow Raman spectrum containing bands at 283, 528 and 910 cm⁻¹ [11,46]. Savinkina et al. [46] ascribe it to the [TiO_x(O₂)_{2-x}(H₂O)_m] phase, which is explained as “an ordered substitutional solid solution with replacement of some oxide ions with peroxide ions”. The particular bands, however, are not assigned. However, as previously confirmed by XRD studies (Fig. 1), a resemblance to the Raman spectra of layered titanates appears [20,38,39]. Three of the four bands observed in the TiO₂-yellow spectra align with frequencies typical of layered titanates (283 cm⁻¹, 685 cm⁻¹ and 910 cm⁻¹). According to the literature [47], two of these bands (283 cm⁻¹, 685 cm⁻¹) are attributed to the skeletal vibrations of Ti O bonds (bridging oxygen atoms). Among them, the Ti O vibration connected with the band at 685 cm⁻¹ is not changed by the composition of the titanate interlayer. Meanwhile, the 283 cm⁻¹ band may be changed or even totally lost by ion exchange in the interlayer [47]. The last band of layered titanates at 910 cm⁻¹ is attributed to the stretching vibration of terminal Ti O X bonds in the interlayers (non-bridging oxygen atoms) [48]. In sodium titanates [47], this band shifts towards higher frequencies after the ion exchange with lighter hydrogen. This may suggest that the band at 910 cm⁻¹ in yellow TiO₂ originates from the vibrations of terminal Ti O O species. The only band of TiO₂-yellow that does not find a counterpart in the spectra of titanates is the most intense band of 528 cm⁻¹. Some papers have assigned this band specifically to triangular Ti O O moieties [49]. Griffith et al. [49] give a

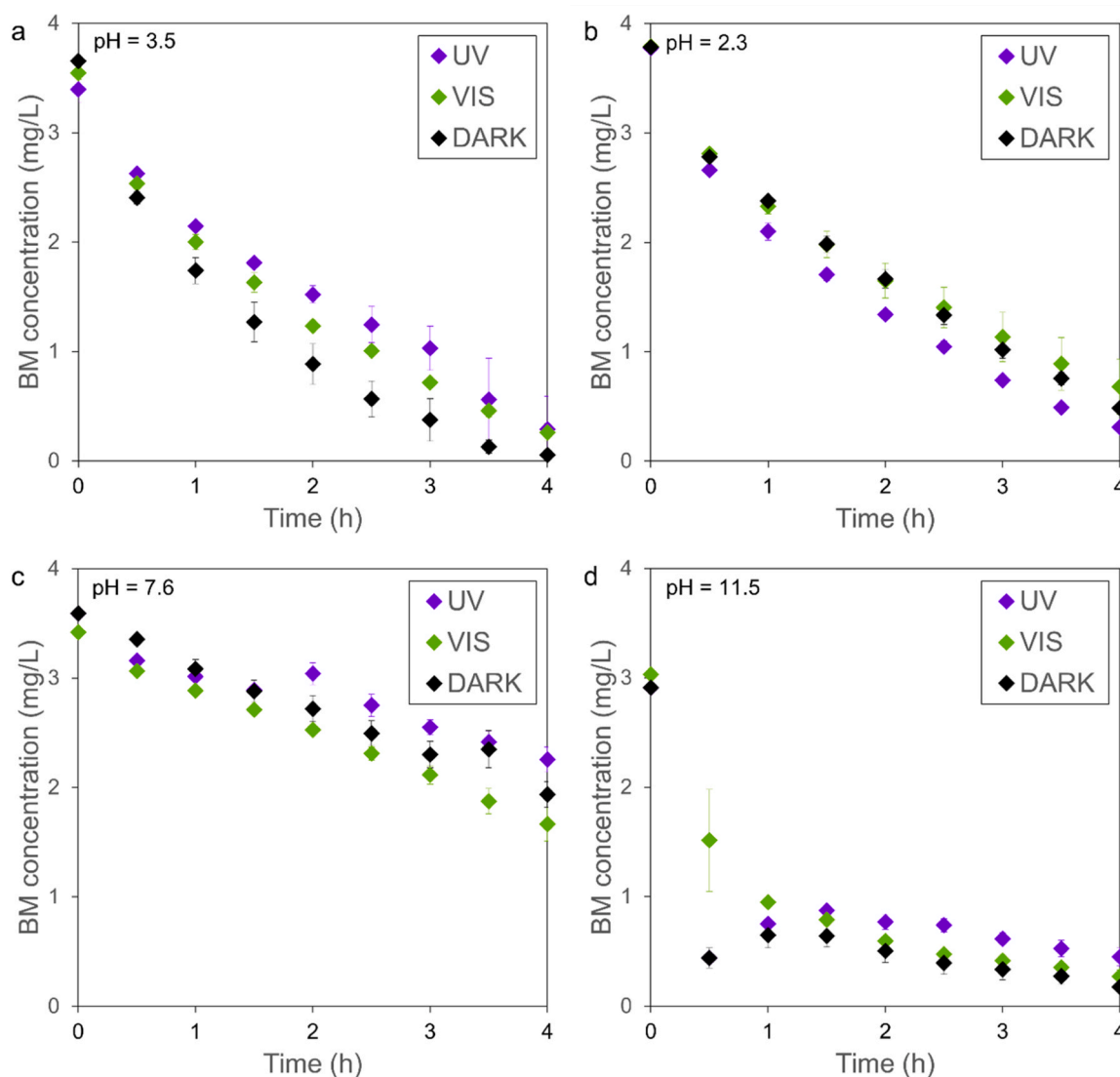


Fig. 5. Kinetics of methylene blue removal using TiO_2 -yellow at different pH conditions (a) not corrected – pH = 3.5, (b) acidified with HCl pH = 2.3, (c) buffered with citrate-phosphate buffer pH = 7.6, (d) alkalinized with NaOH pH = 11.5 (MB initial concentration 3.6 mg/L, photocatalyst dose 0.5 g/L, solution volume 100 mL, error bars represent the standard deviation of the mean).

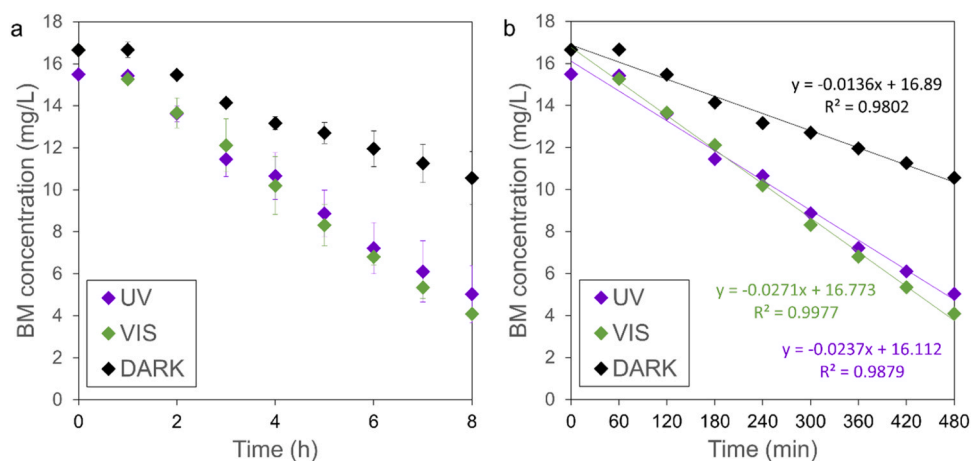


Fig. 6. Kinetics of methylene blue removal using TiO_2 -yellow at higher MB concentration and prolonged process duration – 8 h with (b) zero-order kinetics rate constants (MB initial concentration 16.0 mg/L, photocatalyst dose 0.5 g/L, solution volume 100 mL, error bars represent the standard deviation of the mean).

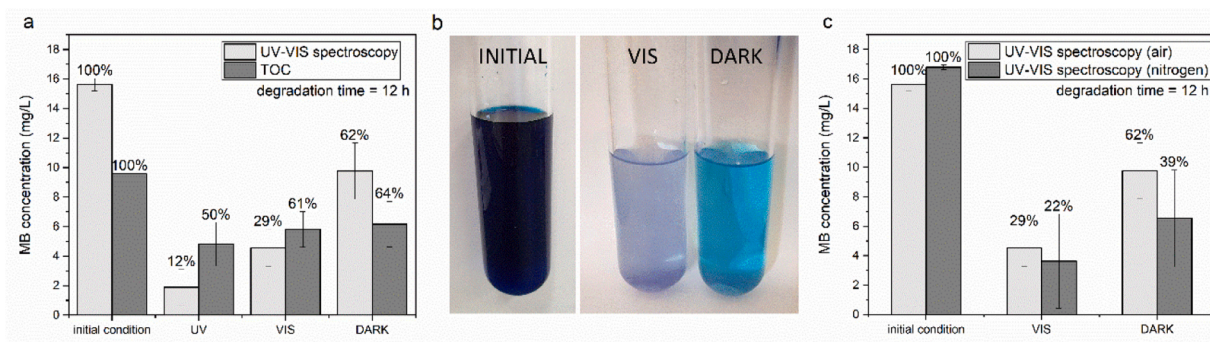


Fig. 7. Methylene blue removal using TiO_2 -yellow at a higher concentration and prolonged process duration – 12 h (a) comparison of final concentration determined by spectrophotometric method and total organic carbon, (b) pictures of solutions before and after removal process, (c) comparison of final concentration determined by spectrophotometric method in air and in nitrogen atmosphere (MB initial concentration 16.0 mg/L, photocatalyst dose 0.5 g/L, solution volume 100 mL, error bars represent the standard deviation of the mean).

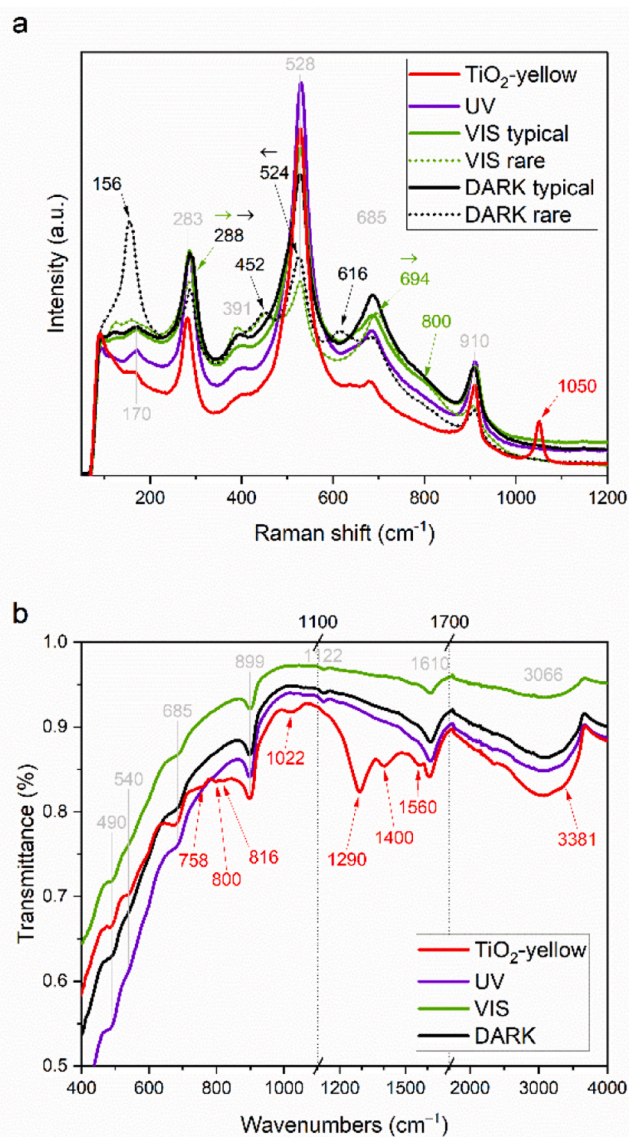


Fig. 8. (a) Raman spectra and (b) FTIR spectra of TiO_2 -yellow before (red) and after photocatalytic process (UV (violet), VIS (green), DARK (black)) (methylene blue removal not corrected – pH=3.5, MB initial concentration 3.6 mg/L, photocatalyst dose 0.5 g/L, solution volume 100 mL, Fig. 5a).

more precise assignment of the triangular group that appears as three Raman-active vibrations near 500, 600 and 900 cm^{-1} , as connected with asymmetric Ti O, symmetric Ti O and O O stretching, respectively.

Generally, the Raman spectra after the degradation of methylene blue shows minor changes to the TiO_2 -yellow structure. The only band present in the spectra of TiO_2 -white and TiO_2 -yellow is the 1050 cm^{-1} band corresponding to the NO_3 vibration, associated with residues of nitric acid used in the synthesis that is lost after degradation of MB (Fig. 8). As Raman spectroscopy is a tool for spot measurement, apart from the typical structures (solid lines) some rare exemptions (dotted lines) are also shown. Alongside the loss of synthesis remains, the Raman spectra of samples after degradation of MB (Fig. 8) reveal the local formation of bands typical of anatase (156 cm^{-1}) and rutile (452 cm^{-1} , 612 cm^{-1}). Usually, a skeletal vibration at 685 cm^{-1} is clearer. However, rare losses of intensity in triangular group bands (528, 685 and 910 cm^{-1}) with respect to skeletal vibrations (283 cm^{-1}) may reflect their local consumption or usage upon MB degradation processes in DARK and VIS.

The IR spectra were also measured (Fig. 8b) as some researchers recognize IR spectroscopy as an efficient tool not only to identify peroxo groups, but also to distinguish their different geometries [50]. By that logic, side-on/triangular groups (denoted as η) are expected to have absorption bands in the range 800–950 cm^{-1} [50,51], and end-on/linear groups (denoted as μ) - in the range 700–770 cm^{-1} [50, 51]. The presence of peroxo groups is also associated with the Ti O O vibration that can be found at 690 cm^{-1} [10,52]. However, their definite assignment is inconclusive in the literature, and discrepancies in the reported values complicate the process of band assignment [53]. There is no doubting that in comparison to the TiO_2 -white record (Figure S6b), the spectrum of TiO_2 -yellow contains more bands characteristic for oxygen groups formed as a result of H_2O_2 modifications in the spectral range from 700 cm^{-1} to 1000 cm^{-1} . The spectrum of TiO_2 -yellow displays the presence of both linear and triangular peroxide groups, although the distinctive band at 899 cm^{-1} indicates the predominance of triangular groups. In the remaining spectral range (above 1000 cm^{-1}), the spectra of TiO_2 -white and TiO_2 -yellow are similar in terms of the position of the bands, with only differences in their relative intensities visible (Figure S6b). Bands at 1022 cm^{-1} and 1290 cm^{-1} may be assigned to C O stretching vibration and C H deformation vibration due to remains of iso-propanol [54]. Also, the bands at 1410 cm^{-1} are associated with the residues after synthesis, in this case with the characteristic vibrations of nitrate ions [55]. The broad peaks centred approximately at 3066 cm^{-1} can be assigned to the fundamental stretching vibration of hydroxyl groups (free or bonded), which is further confirmed by the sharp bands at about 1610 cm^{-1} . Since absorption band 3066 cm^{-1} is caused by the bending vibration of coordinated H_2O as well as Ti OH, the shoulder on the spectrum at 3381 cm^{-1} may be the result of the bending vibrational mode of water [52].

The IR spectra test after MB removal is more detailed in determining the type of synthesis residues lost, such as nitrate groups or iso-propanol. In the range of peroxo group vibrations, only the band at 899 cm^{-1} remains unchanged, while the others at lower frequencies become imperceptible. The low intensity band connected with linear groups (758 cm^{-1}) also disappears. Very careful inspection of the IR spectra recorded for samples after testing identifies new bands of very low intensity at 1222 cm^{-1} that can be associated either with oxygen interstitial [10] that was only visible when the adjacent high intensity band was removed.

The Raman band at 286 cm^{-1} (Fig. 8a) is often claimed to be a defect mode related to oxygen vacancies [11], which can certainly be verified using EPR spectroscopy. The X-band EPR spectra of samples measured in the 0–5000 G field recorded at room temperature exclude the possibility of the presence of oxygen vacancy, however, they show a characteristic signal with rhombic g-tensor (Fig. 9). The g tensor principal components from spectrum of TiO₂-yellow are $g_{zz} = 2.0023$, $g_{yy} = 2.0084$, $g_{xx} = 2.0209$. This result strongly suggests the presence of a stable superoxide radical anion generated by the modification of TiO₂ with H₂O₂.

The g_{zz} values in the range between 2.019 and 2.026 are usually reported for superoxide on TiO₂ surfaces, which are consistent with those expected for O₂^{•−} stabilized at Ti⁴⁺ site (O₂^{•−}—Ti⁴⁺) [23,56]. In the spectra after MB removal (Fig. 9), the g parameters are similar, which evidences no change in the structural environment of the superoxide species ($g_{zz} = 2.0024$, $g_{yy} = 2.0085$, $g_{xx} = 2.0206$; $g_{zz} = 2.0023$, $g_{yy} = 2.0085$, $g_{xx} = 2.0206$ for samples activated by visible light and in the dark, respectively). Use of the excess of MB does not create any difference (Table S1). As superoxo species are sensitive to temperature, annealing of the samples was performed (Figure S9). The superoxide groups are lost below $300\text{ }^{\circ}\text{C}$ (Figure S9a), which is connected with the crystallisation to the anatase confirmed by Raman spectra (Figure S9b) and is consistent with the previous DSC-TG analysis revealing the start of crystallization to be $257\text{ }^{\circ}\text{C}$ (Figure S3). What is more, the partial crystallization upon storage (visible as the occurrence of an anatase peak, Figure S10) causes the shift in g values (Table S1).

3.3.2. XPS studies

Yet another surface defect produced upon titanium dioxide sensitization with H₂O₂ is titanium ion at lower oxidation states Ti²⁺ and Ti³⁺ [11,30], the presence of which can be confirmed by surface X-ray photoelectron spectroscopy. The analysis of the Ti 2p high-resolution spectra of TiO₂-yellow before and after methylene blue degradation and commercial TiO₂ - Degussa P25 (Fig. 10a, Figure S11, Table S3) showed only two peaks at binding energies of 459.3 and 465.1 eV corresponding to 2p_{3/2} and 2p_{1/2} of Ti⁴⁺ respectively, which ensures the

presence of Ti⁴⁺ only.

The deconvolution of the C 1 s spectrum can be helpful in the identification of the distribution of organic functional groups adsorbed on the surface of the studied materials. To resolve the C 1 s peak (Figure S12, Table S2), the reference binding energies were taken from studies by M. Koinuma et al. [57] and M. Rabchinskii et al. [58]. The spectra of all samples both before and after the MB degradation process (Figure S12), including TiO₂-white and Degussa P25, were resolved to the same peaks with similar contributions of each component. In each case, the dominant carbon forms were due to C-H and C=O bonded atoms, regardless of whether the samples were measured before or after the MB degradation. Supposedly, the presence of carbon compounds in the outermost layer of all the studied samples resulted mainly from their contamination, which occurs in all XPS-measured samples [59], therefore, no additional information about organic residuals from methylene blue degradation could be obtained from this analysis.

More informative is the analysis of O 1 s peaks of the studied samples (Fig. 10b-f, Table S4). The spectra were resolved to four components arising from skeletal oxygen atoms O^{2−} at 531 eV, oxygen in Ti OH surface groups at 532 eV, adoxygen atoms attributed to superoxo and peroxo groups at 533.1 eV and oxygen corresponding to physisorbed water molecules at 533.9 eV [11,60]. Comparison of the O 1 s spectra of TiO₂-yellow and Degussa P25 shows distinctive differences in the chemical character of the oxygen groups on their surface. Whereas the oxygen peak of P25 is composed solely of bulk oxygen and surface hydroxy groups, the main constituents of the yellow TiO₂ are adoxygen groups – 40.5 % (Table S4). This confirms our previous verification of the adoxygen group from FTIR and Raman analyses, which correlates with the changes in the width of the band gap that explains the activity in the visible light region [5,6,8,9,11–13,17,18,21].

The process of methylene blue degradation caused significant changes in the O 1 s spectra composition of TiO₂-yellow, which were different when the process was conducted in the dark and under illumination. In both cases, the share of components attributing to adoxygen groups significantly decreased from 40.5 % to 10.1 % and 23.3 % respectively, identifying their involvement in the process of MB decomposition. Simultaneously, there could also be seen a substantial increase in the share of oxygen contributing to physisorbed water on the surface of the visible light-illuminated sample - from 15.3 % to 30.4 %, which was not observed when the process was conducted in the dark. The differences in the surface composition of our samples with/without light activation are visible not only in XPS spectra (Fig. 10) but they are also reflected in the behaviour of the samples upon switching of the magnetic stirrer. The VIS-illuminated TiO₂-yellow form a stable suspension in the purified MB illuminated solution, which may be connected with the increase of water adsorbed on the surface that improves water-dispersibility [15], while samples after the dark process immediately sank gravitationally. Apparently, the MB degradation on the surface of TiO₂-yellow occurring through different mechanisms depending on the contribution of irradiation changed the surface properties, reflecting the different behaviours of the powder samples after the process. The significantly larger consumption of adoxygen groups in the dark may indicate non-catalytic oxidation of methylene blue. Whereby the contribution of irradiation enabled the switching of additional photocatalytic mechanisms in its degradation. In this case, the increased presence of water molecules on the photocatalyst surface may result from complete MB mineralization to water and carbon dioxide.

3.4. Discussion on the mechanism of organic compound degradation

The discussion of mechanisms begins with a summary of literature studies revealing that the factors contributing to visible light and dark activity of H₂O₂-sensitized Ti-based oxides are generally similar (Table 2). Typical materials features providing activity are as follows: surface hydroxylation [7,12,13,15], the presence of adoxygen groups (peroxo

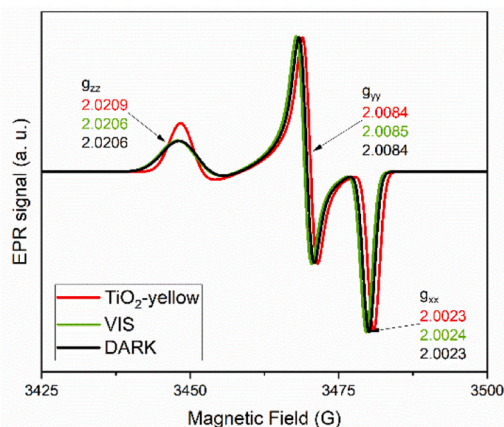


Fig. 9. EPR of TiO₂-yellow before and after photocatalytic process (methylene blue removal not corrected – pH=3.5, MB initial concentration 3.6 mg/L, photocatalyst dose 0.5 g/L, solution volume 100 mL, Fig. 5a).

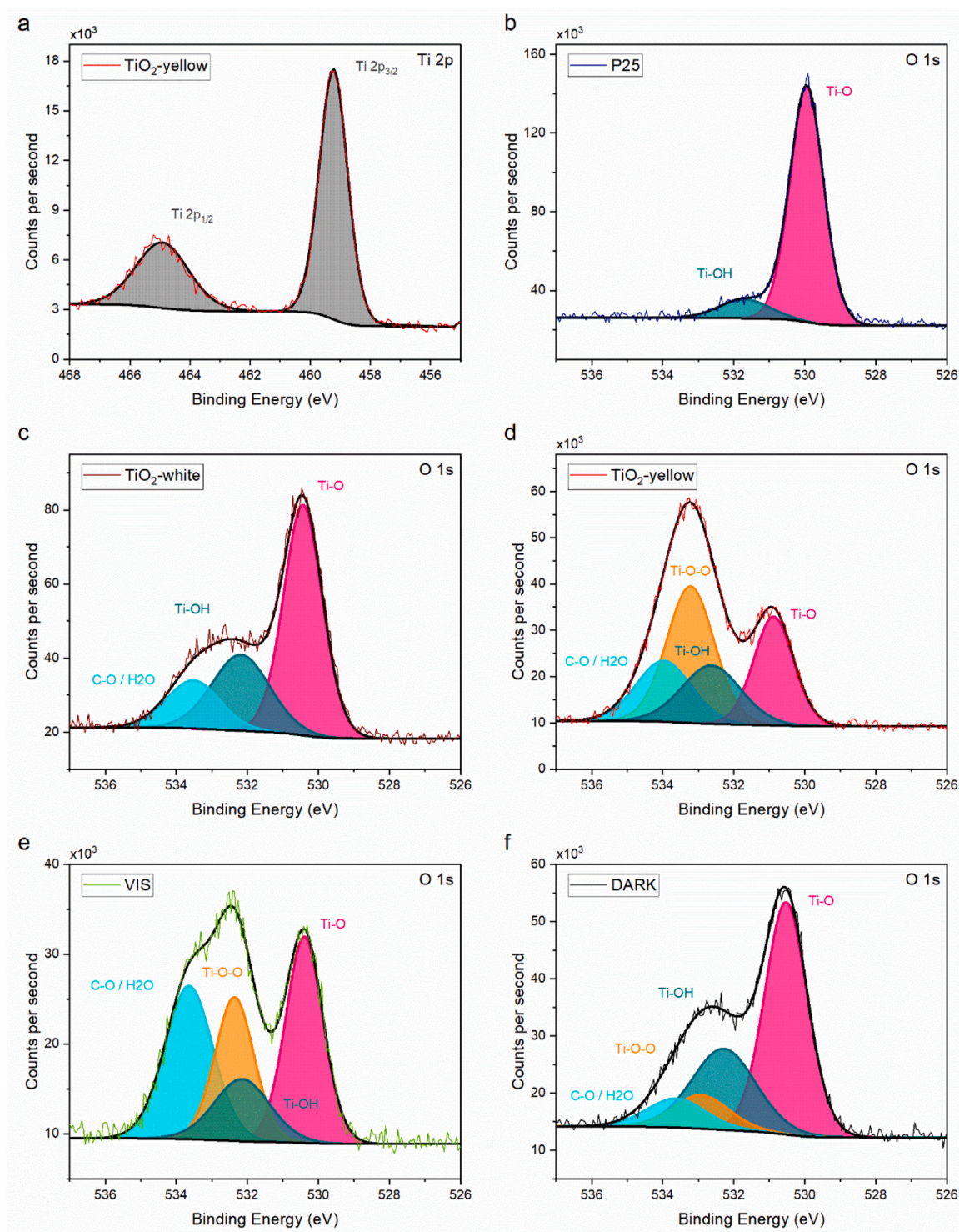


Fig. 10. High-resolution Ti 2p XPS spectra of TiO₂-yellow (no indication for formation of a Ti³⁺) and high-resolution O 1s XPS spectra of (b) Degussa P25 (c) TiO₂-white (d) TiO₂-yellow before MB degradation and after MB degradation (e) under visible light irradiation and (f) in the dark.

and superoxo) [4–6,8,9,11–13,17,18,21], phase composition (anatase to rutile content: [10,17,20,25], amorphous phase content [11,16] or surface amorphization [7,13]), or defects in the crystal structure, being mainly Ti³⁺ or oxygen vacancies [1,4,27]. The activity gained during the activity test bases on radicals' formation [9,11,12,14–16,26,30–32].

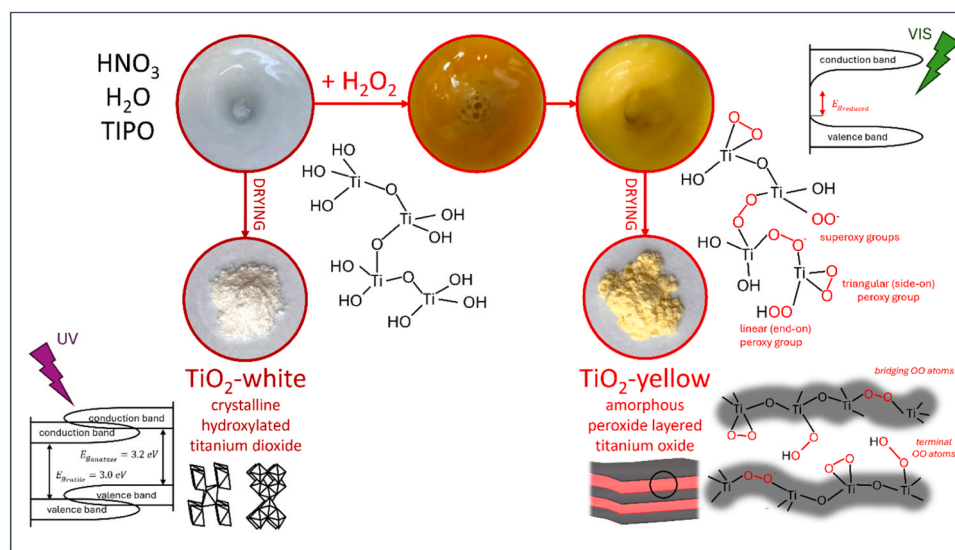
Comparison of our results with literature studies rules out the high crystallinity (Fig. 1), the presence of Ti³⁺ (Fig. 10a, Table S3) and oxygen vacancies (Fig. 9) as possible cause of catalytic performance. Among other features typically listed as positively affecting activity our

material has are: formation of oxygen-rich O–O groups: peroxy (Fig. 8) and superoxo (Fig. 9) groups; narrowed band gap (Fig. 3); surface hydroxylation (Fig. 8, Figure S3, Figure S6); and amorphous layered structure (Fig. 1). These features depending on H₂O₂-sensitization are schematically summarized in Fig. 11.

The observed methylene blue degradation is a multistep process, including adsorption and likely radical decomposition on the H₂O₂-sensitized TiO₂ surface, proceeding differently in the dark and under visible light irradiation. The adsorption efficiency strongly depends on a

Table 2List of photocatalytic and dark activity studies in Ti-based oxides (detailed information available in [Supplementary Materials 2](#)).

No.	Sensitization method	Tested activity	Materials factors	Factors appearing during activity test	Source
1	bottom-up synthesis	VIS and DARK dye degradation	adsorption peroxo groups superoxide radical		this work
2	bottom-up synthesis	VIS organic compounds degradation	peroxo group lack of heating	$[\equiv \text{Ti}^{\text{IV}} \bullet \text{OOH}]^+ [\equiv \text{Ti}^{\text{III}} \text{OOH}]$	[16]
3	bottom-up synthesis	VIS hydrogen production	O O lattice bonds formed from superoxide ions		[6]
4	bottom-up synthesis	VIS dye degradation	negative surface potential band gap narrowing	ROS (HO^\bullet , $\text{O}_2^{\bullet -}$)	[14]
5	bottom-up synthesis	VIS dye degradation	peroxo groups oxygen vacancies amorphous structure	ROS (HO^\bullet , $\text{O}_2^{\bullet -}$)	[11]
6	bottom-up synthesis	VIS dye degradation	peroxo groups band gap narrowing phase composition	ROS ($\text{HO}^\bullet > \text{h}^+ > \text{O}_2^{\bullet -} > \text{e}^-$)	[9]
7	bottom-up synthesis	solar methane production	anatase phase stability textural properties		[17]
8	bottom-up synthesis	VIS dye degradation	band gap narrowing		[10]
9	bottom-up synthesis	VIS dye degradation	band gap narrowing Ti^{3+}		[8]
10	top-down modification	DARK dye degradation	superoxide radical oxygen vacancies	ROS ($\text{O}_2^{\bullet -}$, HOO^\bullet)	[32]
11	top-down modification	VIS dye degradation	peroxo groups amorphous layer		[13]
12	top-down modification	VIS dye degradation	terminal hydroxyl groups	ROS (HO^\bullet)	[15]
13	top-down modification	UV-VIS reforming of methanol	hydroxylation reduced crystallite size		[7]
14	top-down modification	solar dye degradation	surface defects (Ti^{3+} , $\text{Ti}^\bullet\text{OH}$, oxygen vacancies) size distribution		[17]
15	in-situ sensitization	VIS degradation of organic compound		ROS (HO^\bullet)	[12]
16	in-situ sensitization	VIS dye degradation		ROS (HO^\bullet)	[26]
17	in-situ sensitization	DARK dye degradation	superoxide radical	ROS (HO^\bullet , $\text{O}_2^{\bullet -}$, HOO^\bullet) and H_2O_2	[31]
18	in-situ sensitization	DARK dye degradation	superoxide radical oxygen vacancies	ROS ($\text{O}_2^{\bullet -}$, HOO^\bullet)	[32]
19	in-situ sensitization	DARK dyes degradation	peroxo groups high surface area		[28]
20	in-situ sensitization	DARK dyes degradation	oxygen vacancies	ROS ($\text{O}_2^{\bullet -}$, HOO^\bullet , HO^\bullet)	[30]
21	in-situ sensitization	DARK dyes degradation	adsorption amorphous structure (high surface area, hydroxylation)		[29]

**Fig. 11.** Scheme of TiO₂-white and TiO₂-yellow powder production, supplemented with a graphic illustration depicting the differences in the chemical structure of both powders.

low surface pH_{pzc} (point 3.2) being here a consequence of the presence of stable superoxo and peroxo anions entrapped in the structure of the TiO₂-yellow confirmed by EPR, IR and XPS studies (Fig. 8, Fig. 9,

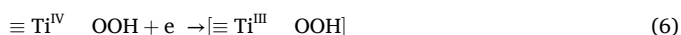
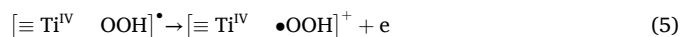
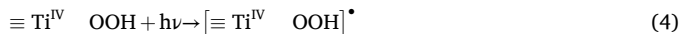
Fig. 10). Negatively charged adooxygen sites enable the adsorption of positively charged MB molecules and facilitated contact of the reagents during the process of their subsequent decomposition, which was

confirmed in studies on H_2O_2 -sensitized TiO_2 [6,31] and Nb_2O_5 [43]. The spectroscopic studies of samples after the MB degradation process conducted in darkness showed substantial consumption of adoxygen groups in favour of the formation of hydroxy groups (Fig. 10). We assume that superoxo groups initiated MB degradation reactions and in combination with peroxo groups created an oxidative environment for its oxidation on the surface of sensitized TiO_2 [31]. In our studies, this process was slow and probably determined the overall rate of the methylene blue removal by slow regeneration of active sites on the powder surface. The products of incomplete methylene blue degradation remained after the process, which was observed as a blue or green colour of the powder samples, indicating sample contamination, but was not confirmed using IR spectroscopy (Figure S8). The observed consumption of adoxygen groups during the process in darkness suggests the role of yellow TiO_2 as a reagent-oxidant instead of as a catalyst. Even though high initial concentrations of MB (16.0 mg/L) were used, the superoxo groups are still present in the samples after the complete MB degradation in dark (Fig. 9). However, because conducted EPR studies are not quantitative, further studies are required in this area to clarify the contribution of different species in organic matter degradation in the dark on the surface of H_2O_2 -sensitized TiO_2 .

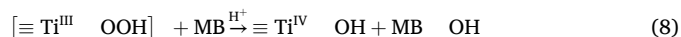
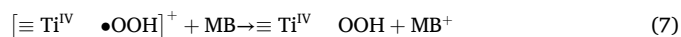
To evaluate longevity of the oxygen-rich groups on the TiO_2 -yellow in the dark, we conducted an additional experiment using the same sample in two cycles of MB removal at a higher concentration (initial MB concentration 16.0 mg/L, with duration of the first cycle 24 h and the second cycle 12 h) without any regeneration or washing step with only drying at room temperature in the dark between the two cycles. The efficiency of MB removal in the first cycle - 82 % decreased to only 68 % in the second cycle. Better efficiency for the second test with comparison with the one for the held for 12 h only (37 %, Fig. 7a), may suggest a contribution of the catalytic mechanism in the process of MB degradation in the dark.

For processes conducted using light (UV, VIS), the decomposition efficiency increases, compared to DARK, which suggests engaging of the photocatalytic mechanism. Even though the differences in the methylene blue concentration (measured spectroscopically) and TOC content to the disadvantage of light-activated processes implies the incomplete mineralization of MB. Additionally, peroxides are considered stable in various conditions [3] besides the presence of some organic compounds under visible light [16], so decrease in the O O component confirmed in the XPS studies (from 40 % to 23 % in VIS and 10 % in DARK, Fig. 10, Table S4) may suggest the cumulative effect of oxidation to the photocatalytic mechanism.

According to Lee et al. [11] and Seo et al. [16], the photochemical activity of the sensitized TiO_2 results from exciting of adoxygen groups. The illumination of H_2O_2 -sensitized titania generates two excited intermediate products $[\equiv \text{Ti}^{\text{IV}} \bullet\text{OOH}]^+$ and $[\equiv \text{Ti}^{\text{III}} \text{OOH}]$ (reactions 4–6). Despite excluding the presence of Ti^{3+} in the TiO_2 -yellow after tests, this does not preclude its formation during the process.



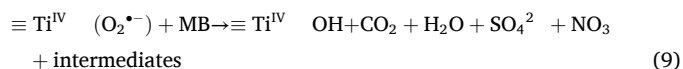
Seo et al. [16] suggest that both photogenerated intermediates are involved in the process of organic compound degradation through the electron abstraction mechanism and hydroxylation, respectively (reactions 7 and 8).



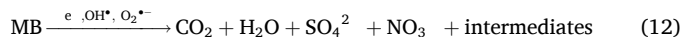
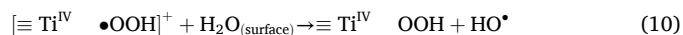
where MB stands for methylene blue and its incomplete degradation

products MB^+ and $\text{MB} \text{OH}$

The illumination is not needed for superoxo groups to initiate MB mineralization (reaction 9):

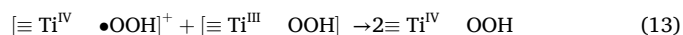


Irrespectively on irradiation type, MB decomposition may also proceed via reactions involving reactive oxygen species HO^\bullet and $\text{O}_2^{\bullet-}$ [11, 25]:



where dissolved oxygen can act as an electron acceptor from the conduction band of the photocatalyst (reaction 11). An additional test conducted in an inert environment (Fig. 7c) revealed that the efficiency of MB removal using H_2O_2 -sensitized TiO_2 under visible-light illumination (78 %) was similar to the efficiency obtained in the oxygenated medium (71 %). This result, similar to observations made by Seo et al. [16], shows minor effect of dissolved oxygen as an electron acceptor from the conduction band of the photocatalyst, which was probably transited to peroxo groups of titania (reaction 6). In contrast, the test with methanol as a hydroxyl radical scavenger [61] may suggest the contribution of reactions 10 and 12 in MB degradation (Figure S14) by inhibiting the process. However, no significant difference was observed using two different molar ratios of MB to methanol, 1:1 and 1:10. We assume that the stronger affinity of MB due to electrostatic attraction resulted in higher adsorption efficiency and, consequently, less impact of methanol in inhibiting the reaction. The effect of adsorption, although opposite in phenol degradation on the TiO_2 surface, was discussed by Schneider et al. [61]. Thus, further studies are needed to confirm the role of hydroxyl radicals.

Following the pattern of the photocatalytic process [16], the photoexcited intermediates eventually recombine:



Rapid electron abstraction and photogenerated intermediate recombination (reactions 7 and 13) leads to the restoration of surface peroxo groups, simultaneously inhibiting photocatalytic degradation. Adoxygen groups are also concurrently consumed in the hydroxylation pathway (reaction 8 and 9), which is particularly evident in samples tested in darkness, that is also competition for light-activated reactions. Those are the possible reasons for the relatively low activity of our product and the prolonged reaction times for complete decomposition of methylene blue (Fig. 4, Fig. 5, Fig. 6, Fig. 7).

Low activity in the dark is also hampered by phase transition. The photocatalytic reactions may promote the crystallisation of amorphous TiO_2 products [62]. Anatase formation is supported by our spectroscopic measurements. The decreased intensity of IR bands assigned to hydroxy groups (Fig. 8b) indicates continuing hydrolysis and condensation during MB degradation in aqueous conditions. The share of the Ti O component in the XPS O 1s spectrum increased after the process conducted in the dark from 25 % to 53 %, which suggests progressive surface crystallisation. Simultaneously, Raman spot measurements (Fig. 8a, DARK) detected very rare crystallites of anatase TiO_2 (156 cm^{-1}), which were also visible in the XRD analyses as the amorphous hump was less broad (Figure S7). Significant changes were observed after the dark process, while after light-activation these were less intense.

Metastability of the TiO_2 -yellow upon MB decomposition encouraged us to check the stability of the material over time without being subjected to any pollutant decomposition processes. Spectroscopic studies after 18 months of storage showed an increased degree of

crystallisation (65 % of TiO₂, Figure S13b), which was similar to that observed after MB removal in the dark. The photocatalytic performance of the four-month-stored sample (Fig. 12) was slightly improved in the visible light-activated process, while its rate in the dark was slightly lower. Presumably, the formed crystalline phases enhance the photocatalytic mechanism of MB degradation by H₂O₂-sensitized TiO₂ [6,18]. This experiment also shows the direction for further modifications to the studied material to improve its efficiency and functionality in photocatalytic processes.

3.5. Perspective and outlook for the obtained material – antimicrobial activity and immobilisation possibility

The degradation of MB was conducted effectively under UV and visible light and without illumination. However, the reaction rate, particularly in dark conditions, was low. For most wastewater treatment processes that rely on continuous flow, such as sewage treatment or water disinfection, self-doping with H₂O₂ alone may be insufficient. Enhancing the kinetics of the reaction can be achieved through band gap engineering or junction engineering [1,2,4–6,8,9,11–13,17,18,21], or directly by addition of H₂O₂ to the reaction chamber [24–27]. Yet another option for such slow-acting materials is their application in a milder environment, utilizing their properties such as self-cleaning and self-sterilizing in order to combat viruses, fungi and bacteria.

In medical settings, where continuous, 24-h operation is essential, this prioritizes qualitative performance in both daylight and dark conditions. The independence of TiO₂ from UV-driven activation resolves a notable drawback of conventional TiO₂ given the limited UV content in the solar spectrum (~4 %) and its absence indoors (UV is blocked by glass), coupled with potential human health risks. Moreover, as the catalytic reaction proceeds on the surface of TiO₂-yellow (only for adsorbed molecules), it avoids the generation of free radicals, thus ensuring human safety in the presence of such a working catalyst. The dark activity of TiO₂-yellow holds promise for continuous cleaning processes (not necessarily under continuous illumination [3,27]), particularly in medical settings, where certain bacteria may persist under photocatalytic conditions and recover in the absence of light [63]. Therefore, after previous investigation of the photocatalytic degradation of MB in the presence of the TiO₂-yellow under visible irradiation and in the dark, the study focused on its antibacterial potential. Generally, similarly to dye degradation processes, the photocatalytic inactivation of bacteria depends on their affinity, illumination and oxidative species generated upon the process [64]. *Enterococcus faecalis* and *Escherichia coli* species, were selected due to their relevance in human pathology [65,66]. Gram-positive *enterococci*, typically harmless in healthy

individuals, can cause serious nosocomial infections, including catheter-associated urinary tract infections, endocarditis, bacteraemia and wound infections. Gram-negative *E. coli* is a frequent cause of hospital-associated bloodstream and urinary tract infections, posing a heightened risk to pregnant women and newborns. Given the high prevalence of these bacteria in the hospital environment and the high risk of them spreading out of medical facilities alongside high wide-spread antimicrobial resistance, the diseases caused by them pose a significant risk to patients and healthcare systems [65,66]. Therefore, the search for modern and safe methods of combatting pathogens is in the interest of public health protection.

The conducted biological tests show (Fig. 13) that both P25 and TiO₂-yellow lead to effective reduction of both Gram-positive (*E. faecalis*) and Gram-negative (*E. coli*) bacteria in the presence of XENON irradiation. Compared to *E. faecalis*, *E. coli* was slightly more susceptible to photocatalytic inactivation with P25 (375 µg/mL leads to 100 % reduction). Photocatalytic inactivation using higher concentrations (750 µg/mL and 1500 µg/mL) of P25 and yellow-TiO₂ led to effective (100 %) eradication of both bacterial strains. The observed photocatalytic activity of the P25 aligns with the current findings on Degussa powder [67,68]. Ricon et al. [64] showed that in-situ sensitization of P25 with H₂O₂ can improve efficiency of *E. coli* photo-inactivation due to direct oxidative action of H₂O₂ and the supplementary effect from surface complexes leading to HO• radical formation. Without H₂O₂ addition, the reduced activity of the TiO₂-yellow activated by a XENON lamp with respect to P25 may relate to the fast recombination of photogenerated intermediates, which impede the disinfection process similarly to the methylene blue degradation described in the previous section (Paragraph 3.5).

In the dark, in contrast, the P25 does not exert any bactericidal action. The lack of activity of P25 in the absence of light is no surprise as TiO₂ is generally acknowledged to be inefficient as an antimicrobial or antiviral agent in dark conditions [64,69]. What is interesting though, is that at a high concentration, TiO₂-yellow exhibit antibacterial activity even in the absence of light. Specifically, 1500 µg/mL of TiO₂-yellow demonstrated a 100 % reduction in the survivability of *E. coli* in the dark, while to achieve the same reduction in the survival of *E. faecalis*, a higher concentration of TiO₂-yellow is required (above 1500 µg/mL). Wiedmer et al. [32] suggested that the primary cause for the observed bactericidal effect in the dark for their H₂O₂-treated TiO₂ coatings was ROS-mediated killing mechanism. Also, the effect of photoinduced ROS introduced prior the antimicrobial test cannot be excluded [27]. The presence of adoxygen groups creating a high oxidative environment formed upon the sensitization of TiO₂ with H₂O₂ may also be a possible explanation for the dark activity of TiO₂-yellow against investigated

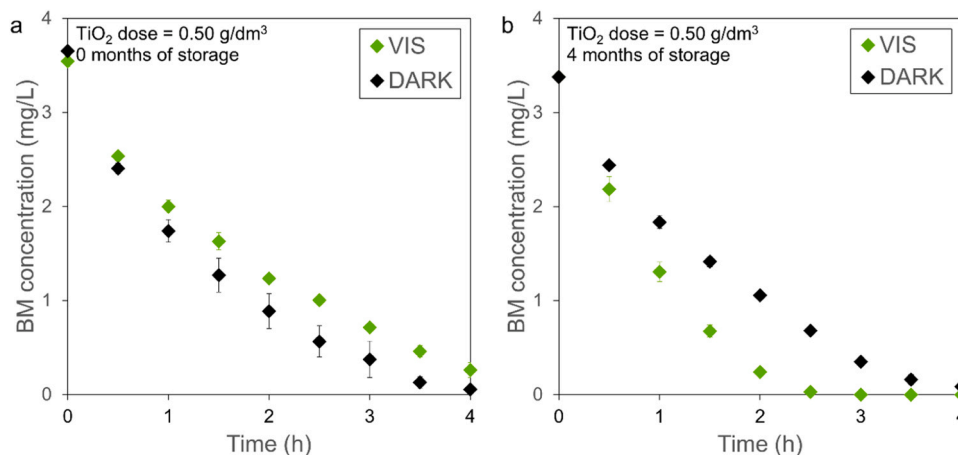


Fig. 12. The influence of storage on the photocatalytic activity and methylene blue degradation of TiO₂-yellow (a) activity directly after synthesis, (b) activity after 4-month storage (MB initial concentration 3.6 mg/L, photocatalyst dose 0.5 g/L, solution volume 100 mL, error bars represent the standard deviation of the mean).

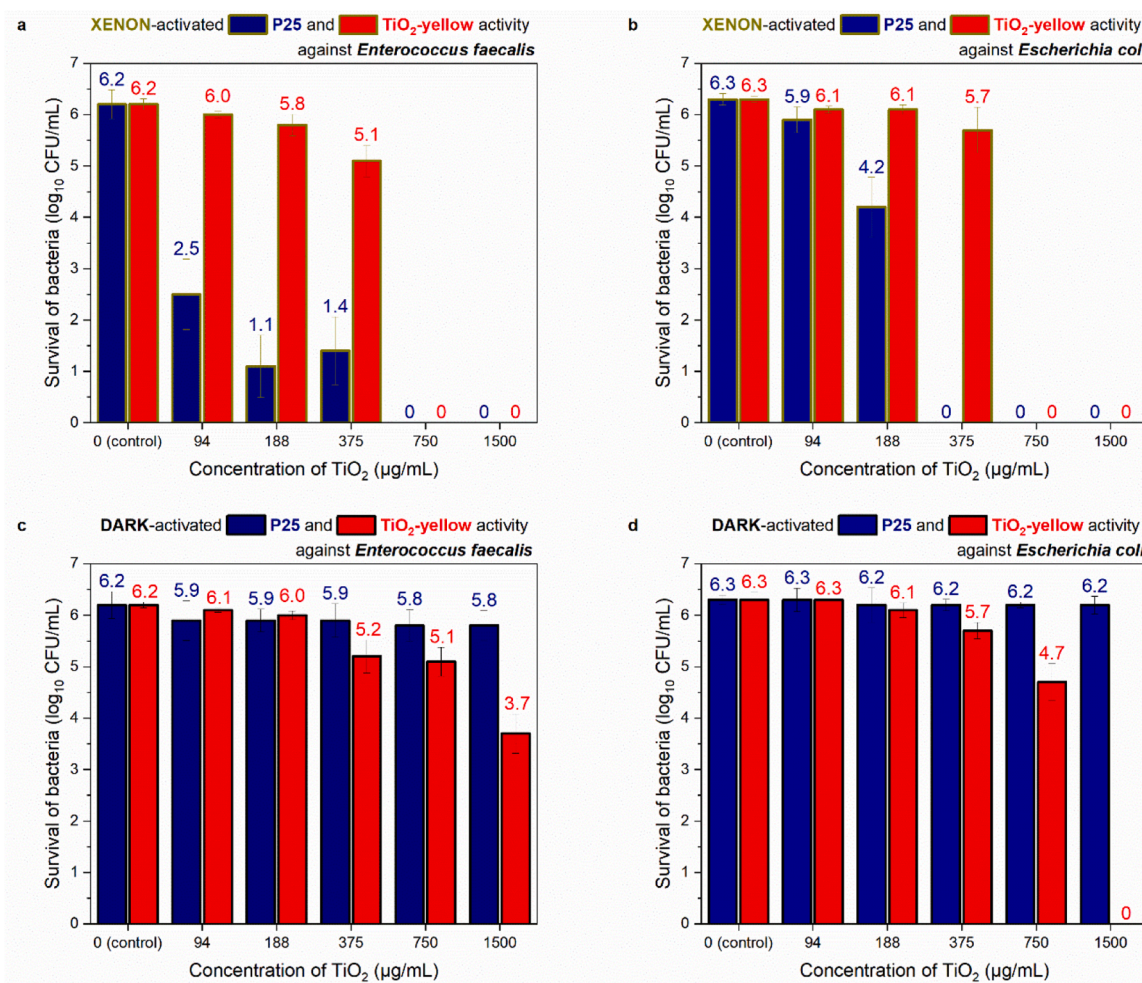


Fig. 13. The bacterial viability of *Enterococcus faecalis* (a,c) and *Escherichia coli* (b,d) at various TiO₂-yellow (red) and P25 (navy) concentrations activated by a XENON lamp (a,b) or without illumination (c,d) (error bars represent the standard deviation of the mean).

planktonic bacteria through peroxidation [27]. The difference in the catalytic response against both spores may originate from difference in the cell wall structure. Thicker peptidoglycan layer of Gram-positive *E. faecalis* compared to Gram-negative provides higher protection against oxidant species [70] which may explain the higher survival rate of enterococci. Additionally, membrane of *E. coli* is more susceptible to peroxidation [27,68], which we confirmed also in the test in the presence of hydrogen peroxide, common disinfectant, only (Figure S15). *E. coli* tends to exhibit also higher adhesion towards TiO₂, which favours inactivation process [70]. Those results are with the agreement of typically reported bacterial susceptibility: *E. coli* > other Gram-negative bacteria > *Enterococcus* > other Gram-positive bacteria [63,70].

Widespread drug-resistant strains of *Enterococci* and *E. coli* prevail in hospital environments, colonizing not only patients but also diverse artificial surfaces. Despite the promising potential of nanostructured TiO₂ dispersed as nanopowders, its practical implementation faces significant challenges, particularly concerning the recovery and recycling of the photocatalyst, as well as posing critical issues due to the potential release of nanosized material into the environment. The problem of catalyst separation and recovery can be addressed by their immobilization, which also facilitate their application and regeneration. Here the versatility of the peroxide-assisted sol-gel should be emphasized as the method enables not only the formation of powders (rods, wires, tubes), but also films and coatings with visible light active photocatalytic properties [4,17,32] and the ability to remove bacteria in the dark [32]. Various approaches have been investigated to immobilize TiO₂

nanostructured photocatalysts on rigid and inert supports [71], representing a highly active area of research in TiO₂ photocatalysis. Currently, several methods are used to produce TiO₂ coatings, although these require more energy and the use of complex equipment, which increases the environmental cost of obtaining such coatings and limits their application potential. Low-pressure cold spraying is a low-energy technique that is scalable and suited to large-scale production. It is also very versatile, allowing for several configurations, also in the field of TiO₂-based nanomaterial deposition [35]. The spraying process can be efficient for forming a coating in a single pass without special atmospheres, e.g. a vacuum or additional post-treatments. For ceramic materials, deposition of their amorphous form provides higher deposition efficiency [35,72] as deformability of the amorphous form enables plastic deformation and hence better anchoring of individual particles [72,73]. This unusual combination of the sol-gel method and low-pressure cold spraying [34] also facilitates the preservation of adoxygen species, as well as maintaining partial amorphicity [33,74]. The crystallinity and the structure of the coating can be controlled by changing the amount of delivered thermal energy [74]. For suspension spraying, the liquid part of the feedstock provides even stronger protection for the suspended oxygen-rich material against degradation upon spraying, consuming a share of energy in the liquid evaporation [34,74]. TiO₂-H₂O₂ coatings sprayed from feedstock in the form of a suspension also eliminate the long and costly drying process. The use of harmful solvents is replaced by the consumption of water, which is used as a reagent for TiO₂ formation without further need for adding reagents

not connected with synthesis. This minimizes the impact on the environment and ensures sustainability for the solution.

4. Conclusion

In this study, TiO₂ was synthesized using the bottom-up-peroxide-assisted sol-gel method without thermal treatment. Consequently, chemical and structural changes in the titania composition were introduced by the incorporation of additional oxygen forming peroxo and superoxo groups, so-called adoxygen groups, appearing in the whole volume of the titania powder grains. These modifications maintained structure amorphization and narrowed the band gap through the formation of midgap states. These properties determined the visible-light-assisted photocatalytic activity of the obtained material in the process of methylene blue degradation. The decomposition of MB started with adsorption on the titania surface, followed by photocatalytic oxidation. The adsorption was facilitated by the low pH_{pzc} of the material, but the overall process rate was restricted by slow MB degradation and the recovery of active sites on the modified titania surface. The low rate of the second step probably resulted from the high recombination speed of the photogenerated intermediates. The obtained material also demonstrated interesting performance in darkness. Chemical and spectroscopic studies confirmed methylene blue adsorption and its subsequent degradation without illumination being involved in the process. This phenomenon resulted from the unique chemical composition of the studied material, which behaved like an adoxygen group reservoir generating reactive oxygen species which enabled MB degradation even in the dark process. The visible-light-driven activity and the activity in the dark of H₂O₂-sensitized TiO₂ were also observed in antibacterial tests against *Escherichia coli* and *Enterococcus faecalis*. The biocidal properties, in combination with activity under different conditions, make modified titania a promising material for obtaining self-cleaning and antibacterial surfaces.

CRedit authorship contribution statement

Agnieszka Lewińska: Resources, Investigation, Formal analysis, Data curation. **Alicja Seniuk:** Investigation. **Agnieszka Ciechanowska:** Writing – original draft, Investigation. **Irena Jacukowicz-Sobala:** Writing – review & editing, Writing – original draft, Validation, Resources, Project administration, Investigation, Data curation, Conceptualization. **Ewa Dworniczek:** Resources, Investigation. **Marek Jasiorski:** Investigation. **Agnieszka Baszczuk:** Writing – review & editing, Writing – original draft, Resources, Project administration, Investigation, Conceptualization. **Anna Gibas:** Writing – review & editing, Writing – original draft, Visualization, Project administration, Investigation, Formal analysis, Data curation, Conceptualization.

Declaration of Competing Interest

The authors declare that they have no known competing financial interests or personal relationships that could have appeared to influence the work reported in this paper.

Data Availability

Data will be made available on request.

Acknowledgements

This research did not receive any specific grant from funding agencies in the public, commercial, or not-for-profit sectors.

The authors would like to thank dr Magdalena Malik from Vibrational Spectroscopy Laboratory, Wrocław University of Science and Technology, for providing the access and offering valuable guidance for FTIR spectroscopic measurements. Thanks are also due to Dr Wojciech

Gil from Electron Microscopy Laboratory, University of Wrocław, for dedicating time during the May long weekend to thoroughly examine all the intriguing samples and for capturing each and every "one more picture". We extend their special gratitude to dr Marcin Kuśmierz from Analytical Laboratory, Maria Curie-Skłodowska University in Lublin, for his enthusiasm and dedication to taking XPS measurements of yellow titania. The XPS measurement was carried out with the equipment purchased thanks to the financial support of the European Regional Development Fund in the framework of the Polish Innovation Economy Operational Program (contract no. POIG.02.01.00–06024/09 – Centre of Functional Nanomaterials).

Appendix A. Supporting information

Supplementary data associated with this article can be found in the online version at [doi:10.1016/j.jece.2024.113975](https://doi.org/10.1016/j.jece.2024.113975).

References

- [1] J. Wang, Z. Wang, W. Wang, Y. Wang, X. Hu, J. Liu, X. Gong, W. Miao, L. Ding, X. Li, J. Tang, Synthesis, modification and application of titanium dioxide nanoparticles: a review, *Nanoscale* (2022) 6709–6734, <https://doi.org/10.1039/d1nr08349j>.
- [2] W. Zhang, H. He, H. Li, L. Duan, L. Zu, Y. Zhai, W. Li, L. Wang, H. Fu, D. Zhao, Visible-Light Responsive TiO₂-Based materials for efficient solar energy utilization, *Adv. Energy Mater.* 11 (2021) 1–24, <https://doi.org/10.1002/aenm.202003303>.
- [3] P. Krishnan, M. Liu, P.A. Itty, Z. Liu, V. Rheinheimer, M.H. Zhang, P.J.M. Monteiro, L.E. Yu, Characterization of photocatalytic TiO₂ powder under varied environments using near ambient pressure X-ray photoelectron spectroscopy, *Sci. Rep.* 7 (2017) 1–11, <https://doi.org/10.1038/srep43298>.
- [4] J.Y. Piquemal, E. Briot, J.M. Brègeault, Preparation of materials in the presence of hydrogen peroxide: From discrete or "zero-dimensional" objects to bulk materials, *Dalt. Trans.* 42 (2013) 29–45, <https://doi.org/10.1039/c2dt31660a>.
- [5] X. Kong, C. Zeng, X. Wang, J. Huang, C. Li, J. Fei, J. Li, Q. Feng, Ti-O-O coordination bond caused visible light photocatalytic property of layered titanium oxide, *Sci. Rep.* 6 (2016) 1–8, <https://doi.org/10.1038/srep29049>.
- [6] Q. Wu, Y. Cheng, F. Huang, X. Li, X. Cui, J. Xu, Y. Wang, In-situ creating elastic lattice O O bonds over semicrystalline yellow TiO₂ nanoparticles for significantly enhanced photocatalytic H₂ production, *J. Hazard. Mater.* 374 (2019) 287–295, <https://doi.org/10.1016/j.jhazmat.2019.04.035>.
- [7] S.A. Razak, H. Bahruji, A.H. Mahadi, H.W. Yun, H₂O₂ Exfoliation of TiO₂ for Enhanced hydrogen production from photocatalytic reforming of methanol, *Bull. Chem. React. Eng. Catal.* 17 (2022) 420–429, <https://doi.org/10.9767/BCREC.17.2.13920.420-429>.
- [8] C. Random, J.T.S. Irvine, Synthesis and visible light photoactivity of a high temperature stable yellow TiO₂ photocatalyst, *J. Mater. Chem.* 20 (2010) 8700–8704, <https://doi.org/10.1039/c0jm01370f>.
- [9] J.Y. Tai, K.H. Leong, P. Saravanan, A.A. Aziz, L.C. Sim, Dopant-free oxygen-rich titanium dioxide: LED light-induced photocatalysis and mechanism insight, *J. Mater. Sci.* 52 (2017) 11630–11642, <https://doi.org/10.1007/s10853-017-1334-9>.
- [10] V. Etacheri, M.K. Seery, S.J. Hinder, S.C. Pillai, Oxygen rich titania: A dopant free, high temperature stable, and visible-light active anatase photocatalyst, *Adv. Funct. Mater.* 21 (2011) 3744–3752, <https://doi.org/10.1002/adfm.201100301>.
- [11] J.W. Lee, R.H. Jeong, D.I. Kim, J.H. Yu, S.H. Nam, J.H. Boo, Facile synthesis of amorphous Ti-peroxo complex for photocatalytic activity under visible-light irradiation, *J. Clean. Prod.* 239 (2019) 118013, <https://doi.org/10.1016/j.jclepro.2019.118013>.
- [12] E. Han, K. Vijayarangamuthu, J. sang Youn, Y.-K.K. Park, S.-C.C. Jung, K.-J.J. Jeon, Degussa P25 TiO₂ modified with H₂O₂ under microwave treatment to enhance photocatalytic properties, *Catal. Today* 303 (2018) 305–312, <https://doi.org/10.1016/j.cattod.2017.08.057>.
- [13] S. Kang, L. Zhang, C. Liu, L. Huang, H. Shi, L. Cui, Hydrogen peroxide activated commercial P25 TiO₂ as efficient visible-light-driven photocatalyst on dye degradation, *Int. J. Electrochem. Sci.* 12 (2017) 5284–5293, <https://doi.org/10.20964/2017.06.54>.
- [14] H. Park, T. Goto, S. Cho, H. Nishida, T. Sekino, Enhancing Visible Light Absorption of Yellow-Colored Peroxo-Titanate Nanotubes Prepared Using Peroxo Titanium Complex Ions, *ACS Omega* 5 (2020) 21753–21761, <https://doi.org/10.1021/acsomega.0c02734>.
- [15] C.Y. Wu, K.J. Tu, J.P. Deng, Y.S. Lo, C.H. Wu, Markedly enhanced surface hydroxyl groups of TiO₂ nanoparticles with Superior water-dispersibility for photocatalysis, *Mater. (Basel)* 10 (2017), <https://doi.org/10.3390/ma10050566>.
- [16] J. Seo, H. Lee, H.-J. Lee, M.S. Kim, S.W. Hong, J. Lee, K. Cho, W. Choi, C. Lee, Visible light-photosensitized oxidation of organic pollutants using amorphous peroxo-titania, *Appl. Catal. B Environ.* 225 (2018) 487–495, <https://doi.org/10.1016/j.apcatb.2017.12.009>.
- [17] L.L. Tan, W.J. Ong, S.P. Chai, A.R. Mohamed, Visible-light-activated oxygen-rich TiO₂ as next generation photocatalyst: Importance of annealing temperature on

- the photoactivity toward reduction of carbon dioxide, *Chem. Eng. J.* 283 (2016) 1254–1263, <https://doi.org/10.1016/j.cej.2015.07.093>.
- [18] M.V. Shankar, T. Kako, D. Wang, J. Ye, One-pot synthesis of peroxo-titania nanopowder and dual photochemical oxidation in aqueous methanol solution, *J. Colloid Interface Sci.* 331 (2009) 132–137, <https://doi.org/10.1016/j.jcis.2008.11.019>.
 - [19] A.H. Pinto, A.E. Nogueira, M.D. Gonçalves, E.R. Camargo, *Fundam. Adv. Oxid. Peroxo Method (OPM) Synth. Transit. Met. Oxides* (2021) 109–154, https://doi.org/10.1007/978-3-030-62226-8_4.
 - [20] V.R. de Mendonça, O.F. Lopes, W. Avansi, R. Arenal, C. Ribeiro, Insights into formation of anatase TiO₂ nanoparticles from peroxo titanium complex degradation under microwave-assisted hydrothermal treatment, *Ceram. Int.* 45 (2019) 22998–23006, <https://doi.org/10.1016/j.ceramint.2019.07.345>.
 - [21] K.I. Yun, K.S. Sonu, T.S. Han, H.G. Ri, K.A. Han, U.G. Pak, Peroxidase-like activity of a peroxotitanium complex and its inhibition by some hydroxyalkanoic acids, *Catal. Sci. Technol.* 12 (2022) 6370–6374, <https://doi.org/10.1039/d2cy00101b>.
 - [22] M. Anpo, M. Che, B. Fubini, E. Garrone, E. Giamello, M.C. Paganini, Generation of superoxide ions at oxide surfaces, *Top. Catal.* 8 (1999) 189–198, <https://doi.org/10.1023/a:1019117328935>.
 - [23] M. Che, A.J. Tench, Characterization and Reactivity of Molecular Oxygen Species on Oxide Surfaces, *Adv. Catal.* (1983) 1–148, [https://doi.org/10.1016/S0360-0564\(08\)60439-3](https://doi.org/10.1016/S0360-0564(08)60439-3).
 - [24] N. Karamoschos, D. Tasis, Photocatalytic Evolution of Hydrogen Peroxide: A Minireview, *Energies* 15 (2022) 1–21, <https://doi.org/10.3390/en15176202>.
 - [25] T. Hirakawa, K. Yawata, Y. Nosaka, Photocatalytic reactivity for O₂ and OH radical formation in anatase and rutile TiO₂ suspension as the effect of H₂O₂ addition, *Appl. Catal. A Gen.* 325 (2007) 105–111, <https://doi.org/10.1016/j.apcata.2007.03.015>.
 - [26] T. Liu, X. Li, X. Yuan, Y. Wang, F. Li, Enhanced visible-light photocatalytic activity of a TiO₂ hydrosol assisted by H₂O₂: Surface complexation and kinetic modeling, *J. Mol. Catal. A Chem.* 414 (2016) 122–129, <https://doi.org/10.1016/j.molcata.2016.01.011>.
 - [27] C.J. Querebillo, A Review on Nano Ti-Based Oxides for Dark and Photocatalysis: From Photoinduced Processes to Bioimplant Applications, *Nanomaterials* 13 (2023), <https://doi.org/10.3390/nano13060982>.
 - [28] C. Zhou, J. Luo, Q. Chen, Y. Jiang, X. Dong, F. Cui, Titanate nanosheets as highly efficient non-light-driven catalysts for degradation of organic dyes, *Chem. Commun.* 51 (2015) 10847–10849, <https://doi.org/10.1039/c5cc03279b>.
 - [29] C. Random, S. Wongnawa, P. Boonsin, Bleaching of Methylene Blue by Hydrated Titanium Dioxide, *ScienceAsia* 30 (2004) 149, <https://doi.org/10.2306/scienceasia1513-1874.2004.30.149>.
 - [30] Z. Wu, K. Guo, S. Cao, W. Yao, L. Piao, Synergetic catalysis enhancement between H₂O₂ and TiO₂ with single-electron-trapped oxygen vacancy, *Nano Res* 13 (2020) 551–556, <https://doi.org/10.1007/s12274-020-2650-y>.
 - [31] D. Wiedmer, E. Sagstuen, K. Welch, H.J. Haugen, H. Tiainen, Oxidative power of aqueous non-irradiated TiO₂-H₂O₂ suspensions: Methylene blue degradation and the role of reactive oxygen species, *Appl. Catal. B Environ.* 198 (2016) 9–15, <https://doi.org/10.1016/j.apcatb.2016.05.036>.
 - [32] D. Wiedmer, C. Cui, F. Weber, F.C. Petersen, H. Tiainen, Antibacterial Surface Coating for Bone Scaffolds Based on the Dark Catalytic Effect of Titanium Dioxide, *ACS Appl. Mater. Interfaces* 10 (2018) 35784–35793, <https://doi.org/10.1021/acsami.8b12623>.
 - [33] A. Gibas, A. Baszczuk, M. Jasiorski, M. Winnicki, D. Ociński, Preparation of Visible-Light Active Oxygen-Rich TiO₂ Coatings Using Low Pressure Cold Spraying, *Coatings* 12 (2022), <https://doi.org/10.3390/coatings12040475>.
 - [34] A. Gibas, A. Baszczuk, M. Jasiorski, A. Lewińska, M. Winnicki, Low-pressure cold spraying of suspension TiO₂ in a single pass – Process optimization, *Surf. Coat. Technol.* 472 (2023), <https://doi.org/10.1016/j.surfcoat.2023.129933>.
 - [35] M. Winnicki, Advanced Functional Metal-Ceramic and Ceramic Coatings Deposited by Low-Pressure Cold Spraying: A Review, *Coatings* 11 (2021) 1044, <https://doi.org/10.3390/coatings11091044>.
 - [36] G. Newcombe, R. Hayes, M. Drikas, Granular activated carbon: Importance of surface properties in the adsorption of naturally occurring organics, *Colloids Surf. A Physicochem. Eng. Asp.* 78 (1993) 65–71, [https://doi.org/10.1016/0927-7757\(93\)80311-2](https://doi.org/10.1016/0927-7757(93)80311-2).
 - [37] J. Mühlebach, K. Müller, G. Schwarzenbach, The peroxo complexes of titanium, *Inorg. Chem.* 9 (1970) 2381–2390, <https://doi.org/10.1021/ic50093a001>.
 - [38] J. Xie, X. Wang, Y. Zhou, Understanding Formation Mechanism of Titanate Nanowires through hydrothermal treatment of various ti-containing precursors in basic solutions, *J. Mater. Sci. Technol.* 28 (2012) 488–494, [https://doi.org/10.1016/S1005-0302\(12\)60087-5](https://doi.org/10.1016/S1005-0302(12)60087-5).
 - [39] R.A. Zárate, S. Fuentes, J.P. Wiff, V.M. Fuenzalida, A.L. Cabrera, Chemical composition and phase identification of sodium titanate nanostructures grown from titania by hydrothermal processing, *J. Phys. Chem. Solids* 68 (2007) 628–637, <https://doi.org/10.1016/j.jpcs.2007.02.011>.
 - [40] M. Ashraful Alam, R. Kumar Bishwas, S. Mostofa, S. Akter Jahan, Low-temperature synthesis and crystal growth behavior of nanocrystal anatase-TiO₂, *Mater. Lett.* 354 (2024) 135396, <https://doi.org/10.1016/j.matlet.2023.135396>.
 - [41] InstaNANO, SAED d value and XRD Peak Position calculator, (n.d.). (<https://instanano.com/all/characterization/tem/saed-d-val>).
 - [42] M.A. Blesa, A.D. Weisz, P.J. Morando, J.A. Salfity, G.E. Magaz, A.E. Regazzoni, The interaction of metal oxide surfaces with complexing agents dissolved in water, *Coord. Chem. Rev.* 196 (2000) 31–63, [https://doi.org/10.1016/S0010-8545\(99\)00005-3](https://doi.org/10.1016/S0010-8545(99)00005-3).
 - [43] L. Wolski, K. Sobańska, M. Muńko, A. Czerniak, P. Pietrzyk, Unraveling the Origin of Enhanced Activity of the Nb₂O₅/H₂O₂ System in the Elimination of
 - Ciprofloxacin: Insights into the Role of Reactive Oxygen Species in Interface Processes, *ACS Appl. Mater. Interfaces* 14 (2022) 31824–31837, <https://doi.org/10.1021/acsami.2c04743>.
 - [44] D.F. Ollis, Kinetics of Photocatalyzed Reactions: Five Lessons Learned, *Front. Chem.* 6 (2018), <https://doi.org/10.3389/fchem.2018.00378>.
 - [45] X. Li, C. Chen, J. Zhao, Mechanism of photodecomposition of H₂O₂ on TiO₂ surfaces under visible light irradiation, *Langmuir* 17 (2001) 4118–4122, <https://doi.org/10.1021/la010035s>.
 - [46] E.V. Savinkina, L.N. Obolenskaya, G.M. Kuzmicheva, E.N. Kabachkov, A. A. Gainanova, Y.V. Zubavichus, V.Y. Murzin, N.V. Sadovskaya, Introduction of peroxo groups into titania: preparation, characterization and properties of the new peroxo-containing phase, *CrystEngComm* 17 (2015) 7113–7123, <https://doi.org/10.1039/C5CE01090J>.
 - [47] A. Gajović, I. Friščić, M. Plodinec, D. Iveković, High temperature Raman spectroscopy of titanate nanotubes, *J. Mol. Struct.* 924–926 (2009) 183–191, <https://doi.org/10.1016/j.molstruc.2008.12.072>.
 - [48] G.L.C. Rodrigues, T.G. d Oliveira, S.B.S. Gusmão, O.P. Ferreira, T.L. Vasconcelos, Y. Guerra, R. Milani, R. Peña-García, B.C. Viana, Study of Structural and Optical Properties of Titanate Nanotubes with Erbium under Heat Treatment in Different Atmospheres, *Mater. (Basel)* 16 (2023), <https://doi.org/10.3390/ma16051842>.
 - [49] W.P. Griffith, T.D. Wickins, Studies on transition-metal peroxo-complexes. Part VI. Vibrational spectra and structure, *J. Chem. Soc. A Inorg., Phys. Theor.* (1968) 397, <https://doi.org/10.1039/j19680000397>.
 - [50] T. Ohno, Y. Masaki, S. Hirayama, M. Matsumura, TiO₂-photocatalyzed epoxidation of 1-decene by H₂O₂ under visible light, *J. Catal.* 204 (2001) 163–168, <https://doi.org/10.1006/jcat.2001.3384>.
 - [51] G. Munuera, A.R. González-Elipe, A. Fernández, P. Malet, J.P. Espinós, Spectroscopic characterisation and photochemical behaviour of a titanium hydroxyperoxo compound, *J. Chem. Soc. Faraday Trans. 1 Phys. Chem. Condens. Phases.* 85 (1989) 1279–1290, <https://doi.org/10.1039/F19898501279>.
 - [52] Y. Gao, Y. Masuda, Z. Peng, T. Yonezawa, K. Koumoto, Room temperature deposition of a TiO₂ thin film from aqueous peroxotitanate solution, *J. Mater. Chem.* 13 (2003) 608–613, <https://doi.org/10.1039/b208681f>.
 - [53] Y. Nosaka, Water Photo-Oxidation over TiO₂—History and Reaction Mechanism, *Catalysts* 12 (2022) 1557, <https://doi.org/10.3390/catal12121557>.
 - [54] Dr Phil Brown 2000+, Advanced Organic Chemistry: Infrared spectrum of propan-2-ol CH₃CH(OH)CH₃, *Adv. Lev. Pre-University Chem. Revis. Study Notes.* (n.d.). (<https://docbrown.info/page06/spectra/propan-2-ol-ir.htm>).
 - [55] A. Elmoulouy, A. Mortadi, E. Chahid, R. Elmoznine, Impedance spectroscopy as a tool to monitor the adsorption and removal of nitrate ions from aqueous solution using zinc aluminum chloride anion clay, *Heliyon* 4 (2018) e00536, <https://doi.org/10.1016/j.heliyon.2018.e00536>.
 - [56] M. Anpo, G. Costentin, E. Giamello, H. Lauron-Pernot, Z. Sojka, Characterisation and reactivity of oxygen species at the surface of metal oxides, *J. Catal.* 393 (2021) 259–280, <https://doi.org/10.1016/j.jcat.2020.10.011>.
 - [57] M. Koinuma, H. Tateishi, K. Hatakeyama, S. Miyamoto, C. Ogata, A. Funatsu, T. Taniguchi, Y. Matsumoto, Analysis of reduced graphene oxides by X-ray photoelectron spectroscopy and electrochemical capacitance, *Chem. Lett.* 42 (2013) 924–926, <https://doi.org/10.1246/cl.130152>.
 - [58] M.K. Rabcinskii, S.A. Ryzhkov, D.A. Kirilenko, N.V. Ulin, M.V. Baidakova, V. V. Shnitov, S.I. Pavlov, R.G. Chumakov, D.Y. Stolyarova, N.A. Besedina, A. V. Shvidchenko, D.V. Potorochin, F. Roth, D.A. Smirnov, M.V. Gudkov, M. Brzhzezinskaya, O.I. Lebedev, V.P. Melnikov, P.N. Brunkov, From graphene oxide towards aminated graphene: facile synthesis, its structure and electronic properties, *Sci. Rep.* 10 (2020) 1–12, <https://doi.org/10.1038/s41598-020-63935-3>.
 - [59] G. Greczynski, L. Hultman, The same chemical state of carbon gives rise to two peaks in X-ray photoelectron spectroscopy, *Sci. Rep.* 11 (2021) 1–5, <https://doi.org/10.1038/s41598-021-90780-9>.
 - [60] H. Perron, J. Vandenborre, C. Domain, R. Drot, J. Roques, E. Simoni, J.J. Ehrhardt, H. Catalette, Combined investigation of water sorption on TiO₂ rutile (1 1 0) single crystal face: XPS vs. periodic DFT, *Surf. Sci.* 601 (2007) 518–527, <https://doi.org/10.1016/j.susc.2006.10.015>.
 - [61] J.T. Schneider, D.S. Firak, R.R. Ribeiro, P. Peralta-Zamora, Use of scavenger agents in heterogeneous photocatalysis: truths, half-truths, and misinterpretations, *Phys. Chem. Chem. Phys.* 22 (2020) 15723–15733, <https://doi.org/10.1039/d0cp02411b>.
 - [62] G. Krylova, C. Na, Photoinduced crystallization and activation of amorphous titanium dioxide, *J. Phys. Chem. C* 119 (2015) 12400–12407, <https://doi.org/10.1021/acs.jpcc.5b02048>.
 - [63] A.G. Rincón, C. Pulgarin, Bactericidal action of illuminated TiO₂ on pure *Escherichia coli* and natural bacterial consortia: Post-irradiation events in the dark and assessment of the effective disinfection time, *Appl. Catal. B Environ.* 49 (2004) 99–112, <https://doi.org/10.1016/j.apcatb.2003.11.013>.
 - [64] A.G. Rincón, C. Pulgarin, Effect of pH, inorganic ions, organic matter and H₂O₂ on *E. coli* K12 photocatalytic inactivation by TiO₂: Implications in solar water disinfection, *Appl. Catal. B Environ.* 51 (2004) 283–302, <https://doi.org/10.1016/j.apcatb.2004.03.007>.
 - [65] J. Vila, E. Sáez-López, J.R. Johnson, U. Römling, U. Dobrindt, R. Cantón, C. G. Giske, T. Naas, A. Carattoli, M. Martínez-Medina, J. Bosch, P. Retamar, J. Rodríguez-Bañó, F. Baquero, S.M. Soto, *Escherichia coli*: An old friend with new tidings, *FEMS Microbiol. Rev.* 40 (2016) 437–463, <https://doi.org/10.1093/femsre/fuw005>.
 - [66] S. Ramos, V. Silva, M. Dapkevicius, G. Igrejas, P. Poeta, Enterococci, from Harmless Bacteria to a Pathogen, *Microorganisms* 8 (2020) 1118, <https://doi.org/10.3390/microorganisms8081118>.

- [67] M. Lanao, M.P. Ormad, R. Mosteo, J.L. Ovelleiro, Inactivation of *Enterococcus* sp. by photolysis and TiO₂ photocatalysis with H₂O₂ in natural water, *Sol. Energy* 86 (2012) 619–625, <https://doi.org/10.1016/j.solener.2011.11.007>.
- [68] A.K. Benabbou, Z. Derriche, C. Felix, P. Lejeune, C. Guillard, Photocatalytic inactivation of *Escherichia coli*. Effect of concentration of TiO₂ and microorganism, nature, and intensity of UV irradiation, *Appl. Catal. B Environ.* 76 (2007) 257–263, <https://doi.org/10.1016/j.apcatb.2007.05.026>.
- [69] J. Prakash, J. Cho, Y.K. Mishra, Photocatalytic TiO₂ nanomaterials as potential antimicrobial and antiviral agents: Scope against blocking the SARS-COV-2 spread, *Micro Nano Eng.* 14 (2022) 100100, <https://doi.org/10.1016/j.mne.2021.100100>.
- [70] R. van Grieken, J. Marugán, C. Pablos, L. Furones, A. López, Comparison between the photocatalytic inactivation of Gram-positive *E. faecalis* and Gram-negative *E. coli* faecal contamination indicator microorganisms, *Appl. Catal. B Environ.* 100 (2010) 212–220, <https://doi.org/10.1016/j.apcatb.2010.07.034>.
- [71] M. Dell'Edera, C. Lo Porto, I. De Pasquale, F. Petronella, M.L. Curri, A. Agostiano, R. Comparelli, Photocatalytic TiO₂-based coatings for environmental applications, *Catal. Today* 380 (2021) 62–83, <https://doi.org/10.1016/j.cattod.2021.04.023>.
- [72] M. Winnicki, A. Gibas, A. Baszczuk, M. Jasierski, Low pressure cold spraying of TiO₂ on acrylonitrile butadiene styrene (ABS), *Surf. Coat. Technol.* 406 (2021) 126717, <https://doi.org/10.1016/j.surfcoat.2020.126717>.
- [73] A. Baszczuk, M. Jasierski, M. Winnicki, Low-Temperature Transformation of Amorphous Sol–Gel TiO₂ Powder to Anatase During Cold Spray Deposition, *J. Therm. Spray. Technol.* 27 (2018) 1551–1562, <https://doi.org/10.1007/s11666-018-0769-0>.
- [74] A. Gibas, M. Winnicki, A. Baszczuk, M. Jasierski, Influence of spraying parameters on microstructure of oxygen-rich TiO₂ coatings deposited using suspension low-pressure cold spray, *Surf. Coat. Technol.* (2023) 129321, <https://doi.org/10.1016/j.surfcoat.2023.129321>.

H₂O₂-sensitized titania with activity under visible light and in the dark

Anna Gibas^a, Agnieszka Baszczuk^a, Irena Jacukowicz-Sobala^b, Agnieszka Ciechanowska^b, Marek Jasiorski^a, Ewa Dworniczek^c, Alicja Seniuk^c, Agnieszka Lewińska^d

^a Department of Mechanics, Materials and Biomedical Engineering, Wrocław University of Science and Technology, 25 Smoluchowskiego Street, 50-370 Wrocław, Poland

^b Department of Chemical Technology, Wrocław University of Economics and Business, Komandorska St., 53-345, Wrocław, Poland

^c Department of Microbiology, Faculty of Medicine, Wrocław Medical University, Wrocław 50-368, Poland

^d Faculty of Chemistry, University of Wrocław, 14 Joliot-Curie Street, 50-383 Wrocław, Poland

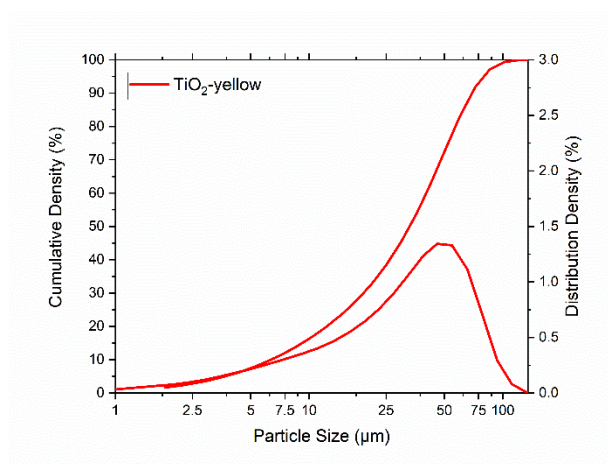


Figure S 1 Particle size distribution of TiO₂-yellow

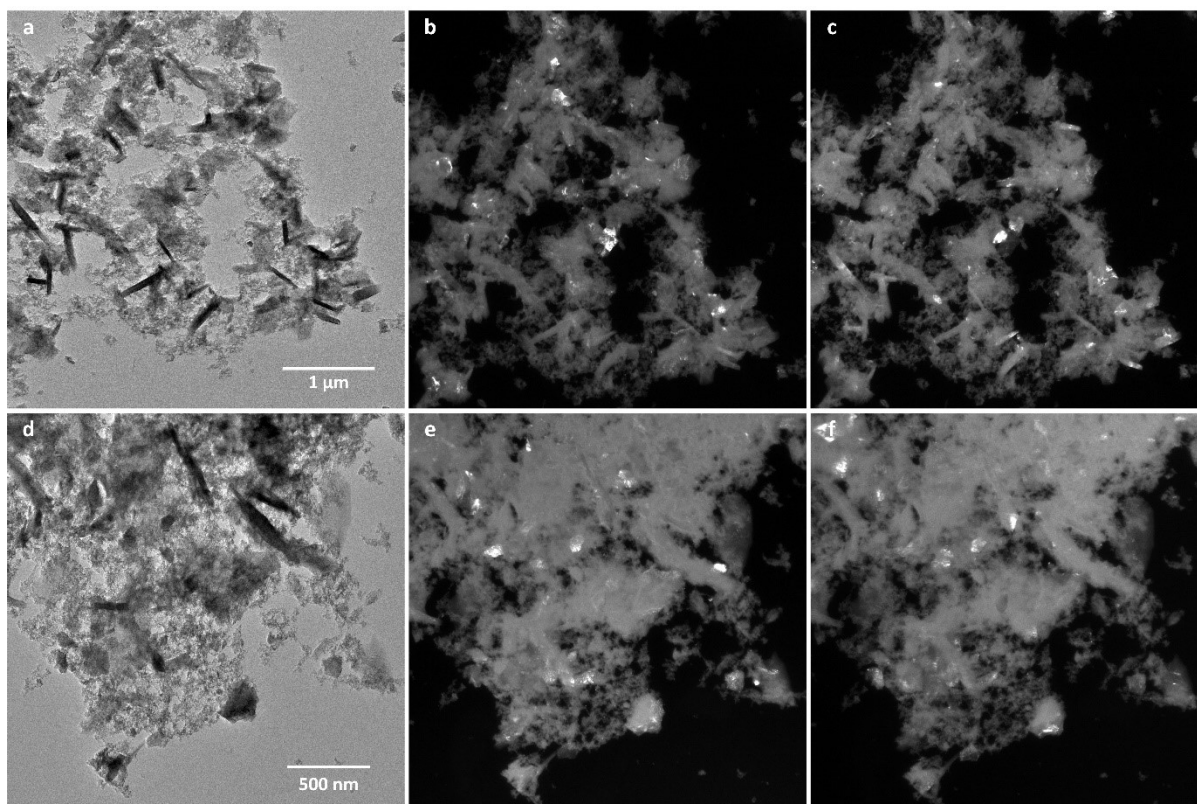


Figure S 2 (a,d) Bright field and (b,c,e,f,) complementary dark field TEM images of TiO₂-yellow

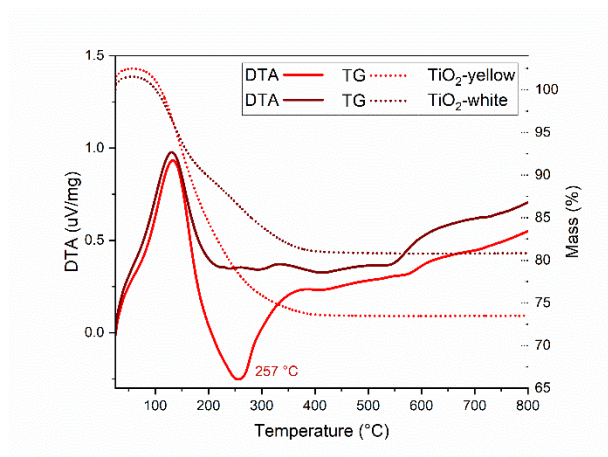


Figure S 3 DSC and TG data for TiO₂-yellow (red) and TiO₂-white (wine)

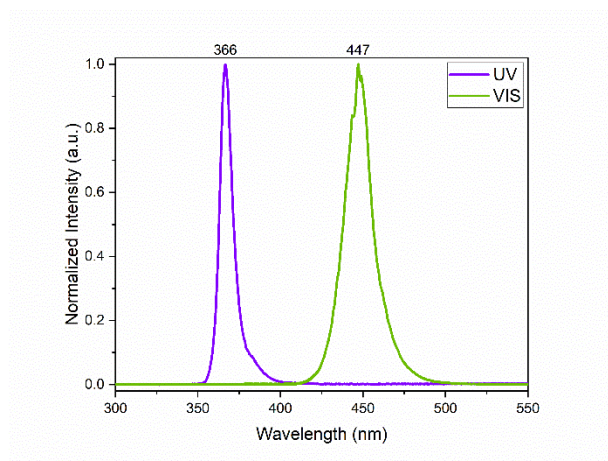


Figure S 4 Spectral characteristics of LED diodes: (a) UV and (b) VIS

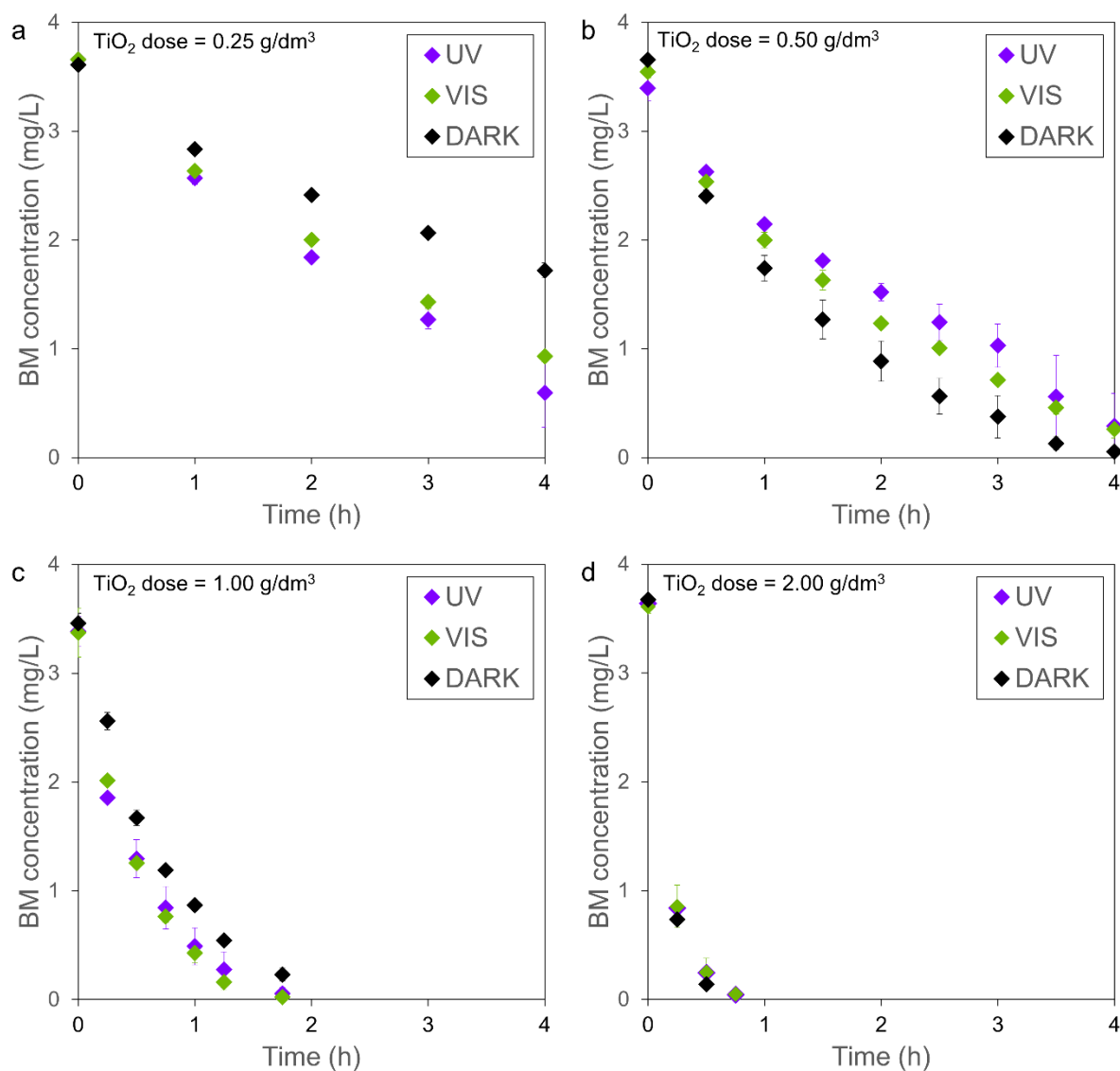


Figure S 5. Kinetics of methylene blue removal using TiO₂-yellow at different photocatalyst dose (a) 0.25 g/L, (b) 0.50 g/L, (c) 1.00 g/L, (d) 2.00 g/L (MB initial concentration 3.6 mg/L, solution volume 100 mL, error bars represent the standard deviation of the mean)

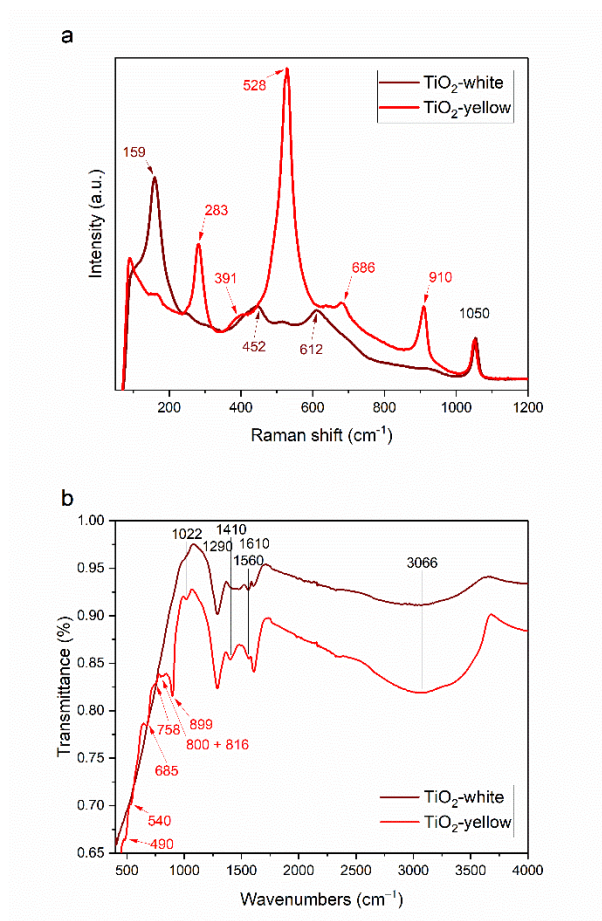


Figure S 6 (a) Raman spectra and (b) FTIR spectra of TiO₂-yellow (red) and TiO₂-white (wine)

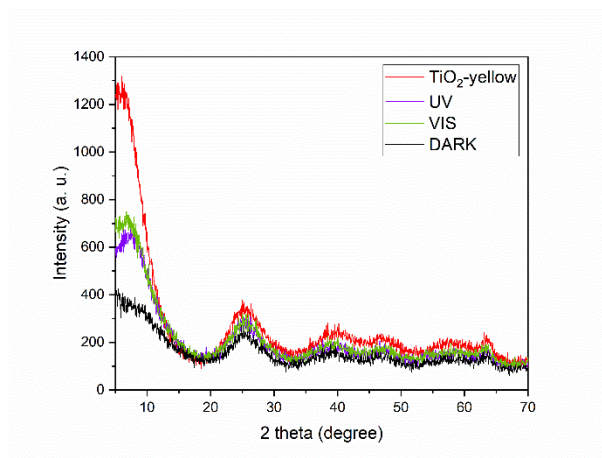


Figure S 7 XRD patterns of TiO₂-yellow before the catalytic testing (red) and after UV (violet), VIS (green) and DARK (black) tests

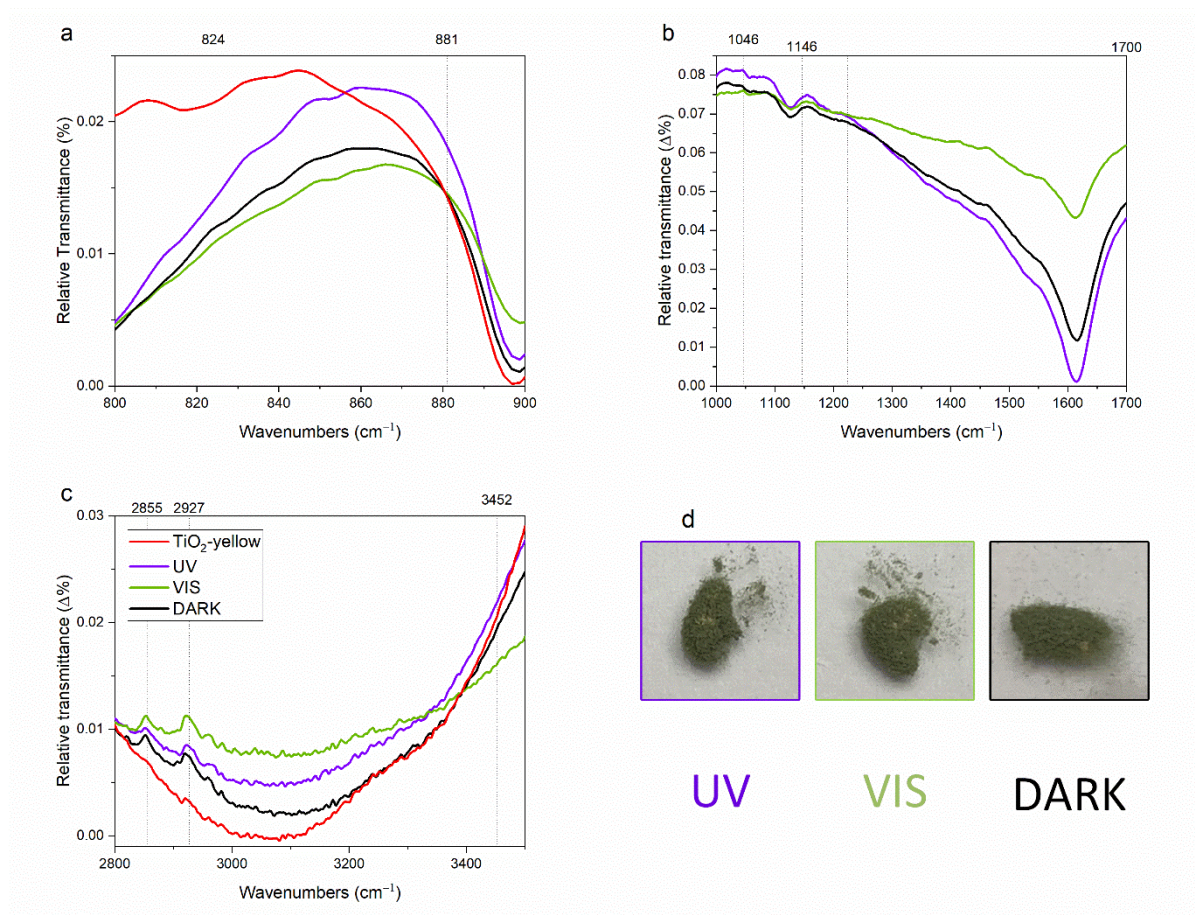


Figure S 8 (a,b,c) FTIR measurement at the selected frequencies to show MB traces (d) pictures of samples with remained light yellow traces after Raman measurements. No traces of MB found in the samples [1].

Table S 1 EPR spectra of TiO₂-yellow before and after photocatalytic process stored 12 months

Sample	TiO ₂ -yellow before and after photocatalytic process (MB ₀ =3.6 mg/L)			TiO ₂ -yellow before and after photocatalytic process (stored 12 months) (MB ₀ =3.6 mg/L)			TiO ₂ -yellow before and after photocatalytic process (stored 12 months) (MB ₀ =16.0 mg/L)		
	gxx	gyy	gzz	gxx	gyy	gzz	gxx	gyy	gzz
TiO ₂ -yellow	2.0021	2.0083	2.0208	2.0032	2.0093	2.0221	2.0032	2.0093	2.0221
DARK	2.0023	2.0084	2.0206	2.0031	2.0092	2.0219	2.0031	2.0092	2.0219
VIS	2.0024	2.0085	2.0206	2.0032	2.0093	2.0221	2.0032	2.0093	2.0221

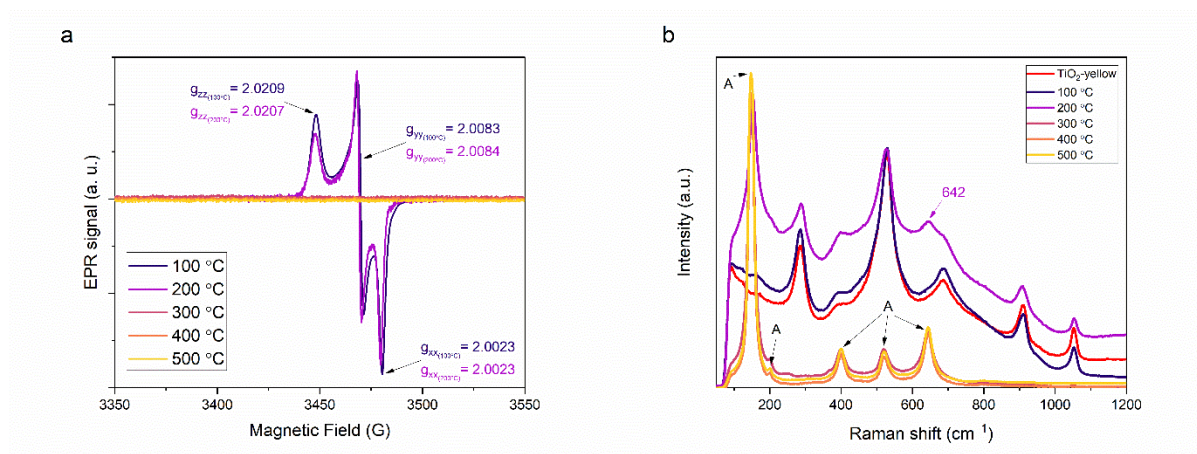


Figure S 9 (a) EPR and (b) Raman spectra of TiO_2 -yellow after 1-h annealing in different temperatures

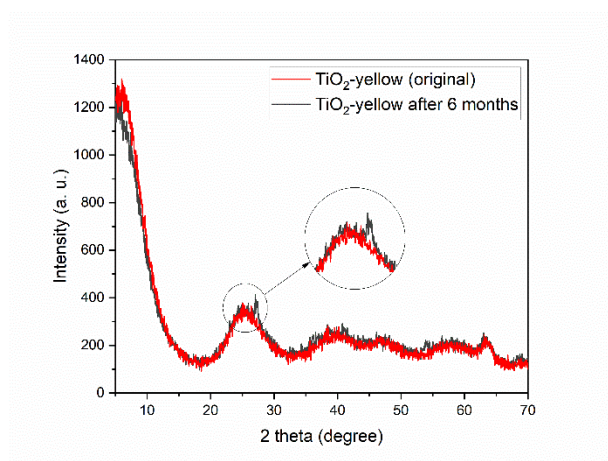


Figure S 10 XRD patterns of TiO_2 -yellow (red) and stored 6 months (dark grey)

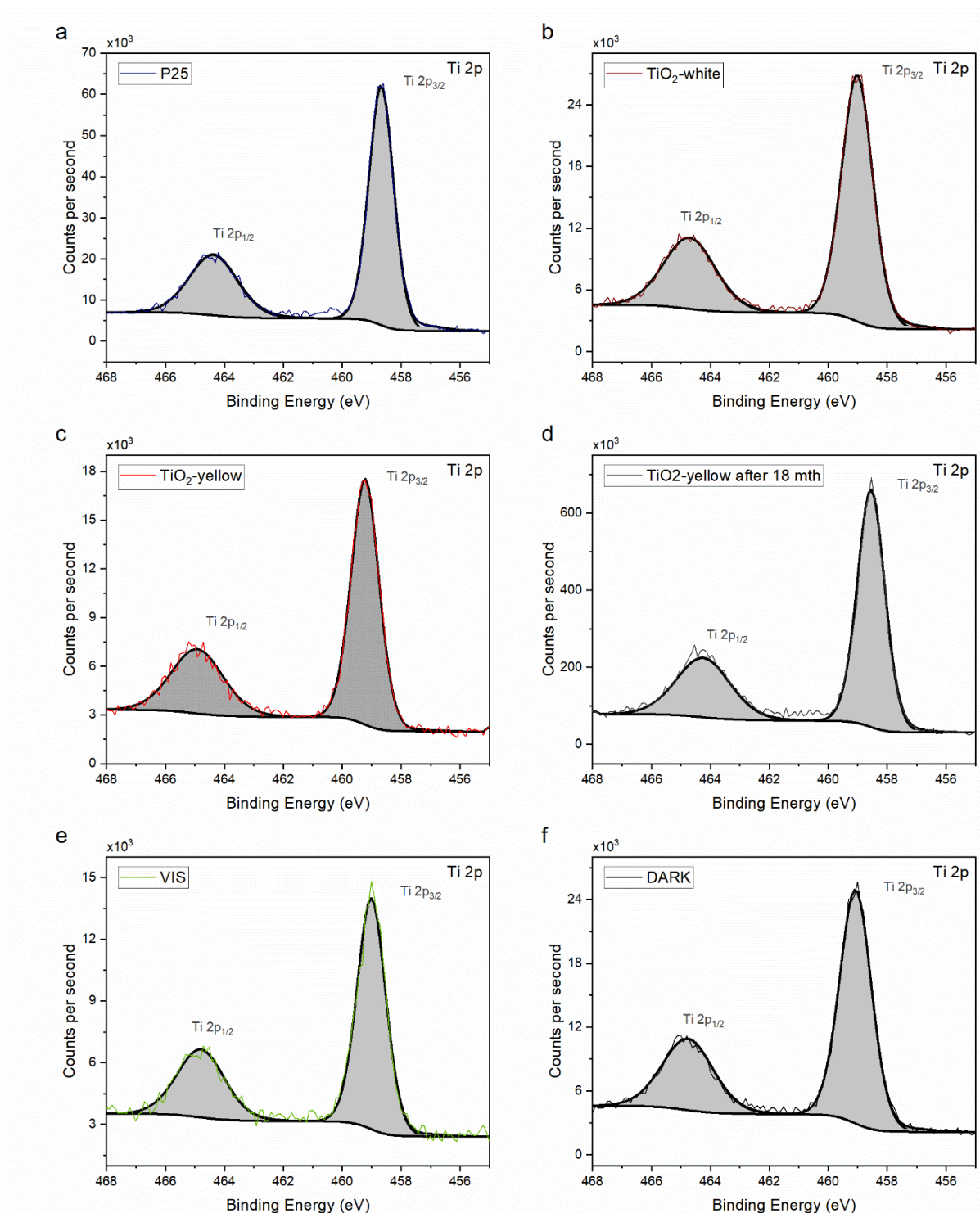


Figure S 11 High-resolution Ti 2p XPS spectra of (a) Degussa P25 (b) TiO₂-white (c) TiO₂-yellow before MB degradation, stored 18 months (dark grey) and after MB degradation (e) under visible light irradiation and (f) in dark

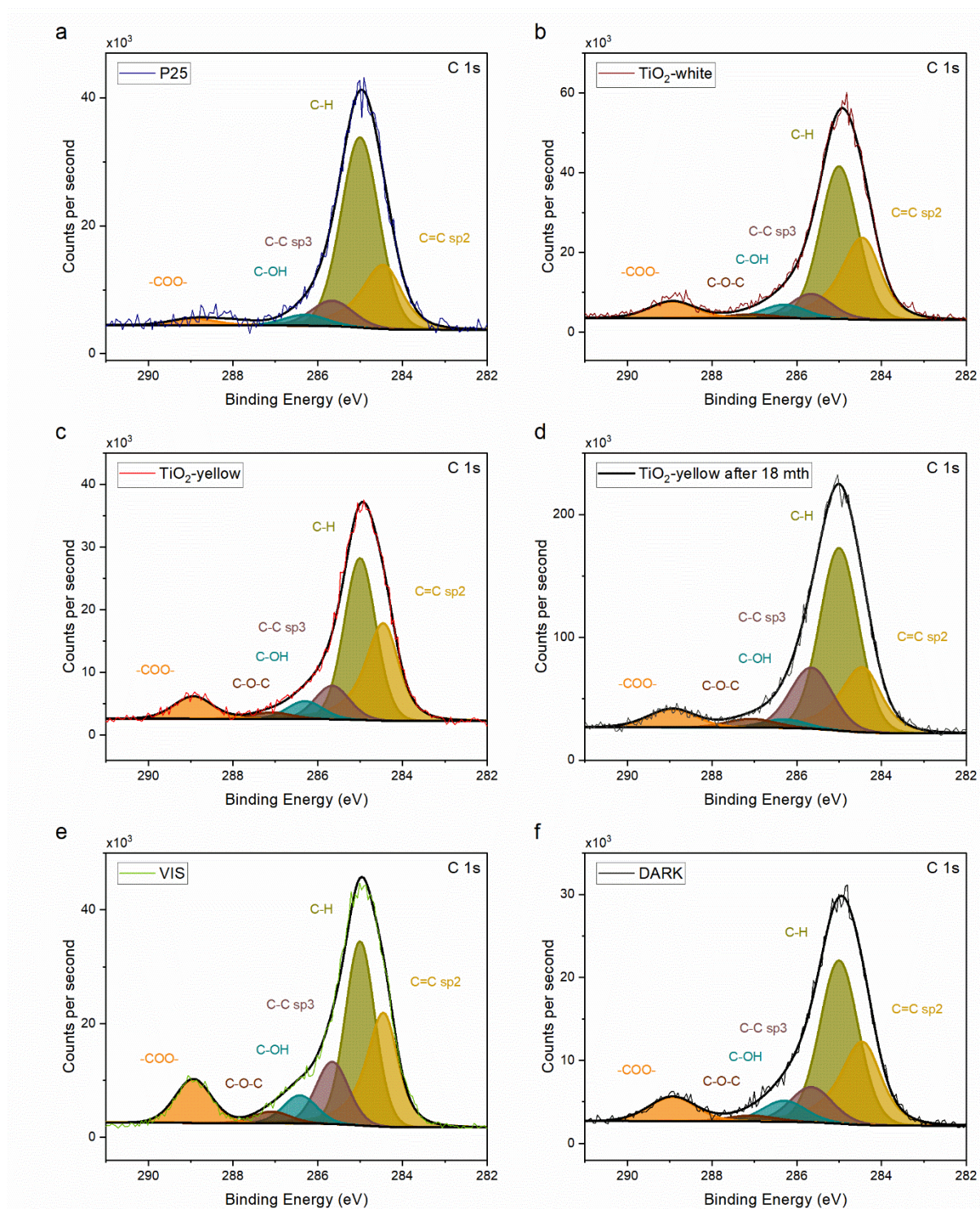


Figure S 12 High-resolution C 1s XPS spectra (a) Degussa P25 (b) TiO₂-white (c) TiO₂-yellow before MB degradation, stored 18 months (dark grey) and after MB degradation (e) under visible light irradiation and (f) in dark

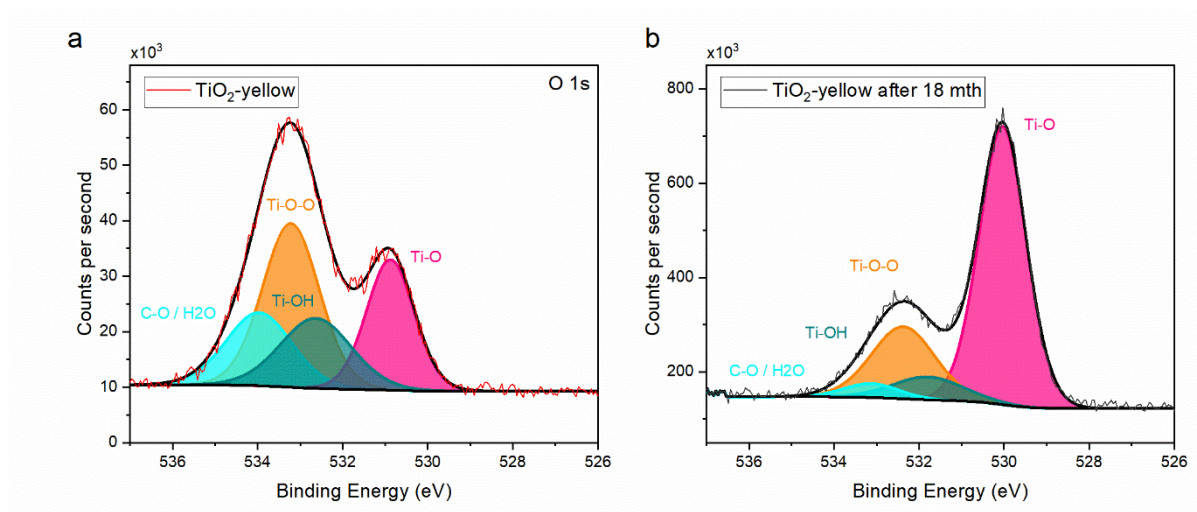


Figure S 13 High-resolution O 1s XPS spectra of (a) TiO₂-yellow and (b) stored 18 months

Table S 2 Resolving the C 1s peak of XPS spectra

For resolving the C 1s peak, the reference binding energies were taken from studies of M. Koinuma et al. [2] and M. Rabchinskii et al. [3].

Sample Identifier	Name	Position	FWHM	Raw Area	%At Conc
P25	C-H	285.00	1.05	33938.846	58.9
	C=C sp ²	284.44	1.03	14146.061	24.5
	C-C sp ³	285.66	1.16	5021.160	8.7
	C-OH	286.30	1.19	2244.214	3.9
	C-O-C	287.08	1.33	1.385	0.0
	C=O	287.97	1.21	856.311	1.5
	-COO-	288.94	1.29	1445.318	2.5
	-COOR	289.74	1.29	1.000	0.0
TiO ₂ -white	C-H	285.00	1.04	43341.182	47.3
	C=C sp ²	284.44	1.02	28739.620	31.4
	C-C sp ³	285.66	1.15	7733.460	8.4
	C-OH	286.30	1.18	4487.924	4.9
	C-O-C	287.08	1.32	1530.809	1.7
	C=O	287.97	1.20	1.000	0.0
	-COO-	288.94	1.28	5792.770	6.3
	-COOR	289.74	1.28	2.799	0.0
TiO ₂ -yellow	C-H	285.00	0.87	24525.417	43.0
	C=C sp ²	284.44	0.86	18193.463	31.9
	C-C sp ³	285.66	0.96	5654.790	9.9
	C-OH	286.30	0.99	3120.452	5.5
	C-O-C	287.08	1.10	1288.887	2.3
	C=O	287.97	1.01	7.993	0.0
	-COO-	288.94	1.07	4134.973	7.3
	-COOR	289.74	1.07	78.944	0.1

Sample Identifier	Name	Position	FWHM	Raw Area	%At Conc
VIS	C-H	285.00	0.82	28849.280	37.2
	C=C sp ²	284.44	0.80	22042.927	28.4
	C-C sp ³	285.66	0.90	10812.067	13.9
	C-OH	286.42	0.93	5026.114	6.5
	C-O-C	287.08	1.04	2361.625	3.0
	C=O	287.97	0.95	1.366	0.0
	-COO-	288.94	1.01	8418.069	10.9
	-COOR	289.74	1.01	3.757	0.0
DARK	C-H	285.00	1.07	22791.973	44.5
	C=C sp ²	284.44	1.04	14321.783	28.0
	C-C sp ³	285.66	1.17	5429.082	10.6
	C-OH	286.30	1.21	3398.516	6.6
	C-O-C	287.08	1.35	1074.284	2.1
	C=O	287.97	1.23	2.537	0.0
	-COO-	288.94	1.31	4157.945	8.1
	-COOR	289.74	1.31	1.908	0.0
TiO ₂ -yellow after 18 month	C-H	285.00	1.07	173220.270	48.7
	C=C sp ²	284.44	1.05	76430.314	21.5
	C-C sp ³	285.66	1.18	64049.261	18.0
	C-OH	286.30	1.22	9678.737	2.7
	C-O-C	287.08	1.35	10899.556	3.1
	C=O	287.97	1.24	1.000	0.0
	-COO-	288.94	1.32	21056.906	5.9
	-COOR	289.74	1.32	582.011	0.2

Table S 3 Resolving the Ti 2p peak of XPS spectra

Sample Identifier	Name	Position	FWHM	Raw Area	%At Conc	%At Conc Total
P25	Ti 2p 3/2 Ti (IV)	458.67	0.99	11955.243	48.9	96.9
	Ti 2p 1/2 Ti (IV)	464.37	1.91	11743.432	48.0	
	Ti 2p 3/2 Ti (III)	457.15	1.54	378.399	1.5	3.0
	Ti 2p 1/2 Ti (III)	462.84	2.97	371.695	1.5	
TiO ₂ -white	Ti 2p 3/2 Ti (IV)	459.01	1.25	6201.965	50.1	98.4
	Ti 2p 1/2 Ti (IV)	464.71	2.06	5969.359	48.3	
	Ti 2p 3/2 Ti (III)	457.14	1.38	99.700	0.8	1.6
	Ti 2p 1/2 Ti (III)	462.84	2.67	97.933	0.8	
TiO ₂ -yellow	Ti 2p 3/2 Ti (IV)	459.22	1.11	3488.762	50.1	99.3
	Ti 2p 1/2 Ti (IV)	464.92	2.07	3426.952	49.2	
	Ti 2p 3/2 Ti (III)	457.14	1.54	26.748	0.4	0.8
	Ti 2p 1/2 Ti (III)	462.84	2.98	26.274	0.4	
VIS	Ti 2p 3/2 Ti (IV)	459.01	1.14	2656.792	49.8	98.7
	Ti 2p 1/2 Ti (IV)	464.80	1.89	2609.722	48.9	
	Ti 2p 3/2 Ti (III)	457.14	1.61	36.791	0.7	1.4
	Ti 2p 1/2 Ti (III)	462.84	3.12	36.139	0.7	

Sample Identifier	Name	Position	FWHM	Raw Area	%At Conc	%At Conc Total
DARK	Ti 2p 3/2 Ti (IV)	459.07	1.27	5794.59	49.6	98.4
	Ti 2p 1/2 Ti (IV)	464.76	2.03	5691.927	48.8	
	Ti 2p 3/2 Ti (III)	457.14	1.55	93.733	0.8	1.6
	Ti 2p 1/2 Ti (III)	462.84	3.00	92.072	0.8	
TiO ₂ -yellow after 18 months	Ti 2p 3/2 Ti (IV)	458.54	1.10	140065.105	49.6	98.4
	Ti 2p 1/2 Ti (IV)	464.24	2.14	137583.583	48.8	
	Ti 2p 3/2 Ti (III)	457.13	1.62	2260.647	0.8	1.6
	Ti 2p 1/2 Ti (III)	462.83	3.12	2220.595	0.8	

Table S 4 Resolving the O 1s peak of XPS spectra

Sample Identifier	Name	Position	FWHM	Raw Area	%At Conc
P25	Ti-O	529.94	1.12	49531.915	89.1
	Ti-OH	531.70	1.66	6079.630	10.9
TiO ₂ -white	Ti-O	530.43	1.29	29827.060	56.0
	Ti-OH	532.18	1.92	14714.703	27.6
	C-O / H ₂ O	533.52	1.79	8687.601	16.3
TiO ₂ -yellow	Ti-O	530.88	1.33	11559.879	24.6
	Ti-OH	532.63	1.98	9181.975	19.6
	C-O / H ₂ O	533.97	1.84	7167.235	15.3
	Ti-O-O-	533.27	1.65	19001.821	40.5
VIS	Ti-O	530.39	1.24	10567.638	32
	Ti-OH	532.15	1.85	4747.219	14.4
	C-O / H ₂ O	533.64	1.59	10033.278	30.4
	Ti-O-O-	532.36	1.30	7699.338	23.3
DARK	Ti-O	530.53	1.41	21296.808	53.0
	Ti-OH	532.29	2.11	11113.692	27.6
	C-O / H ₂ O	533.62	1.95	3725.517	9.3
	Ti-O-O-	532.92	1.87	4075.306	10.1
TiO ₂ -yellow after 18 months	Ti-O	530.03	1.30	285359.020	65.3
	Ti-OH	531.79	1.94	35025.536	8.0
	C-O / H ₂ O	533.12	1.53	17113.324	3.9
	Ti-O-O-	532.37	1.76	99782.164	22.0

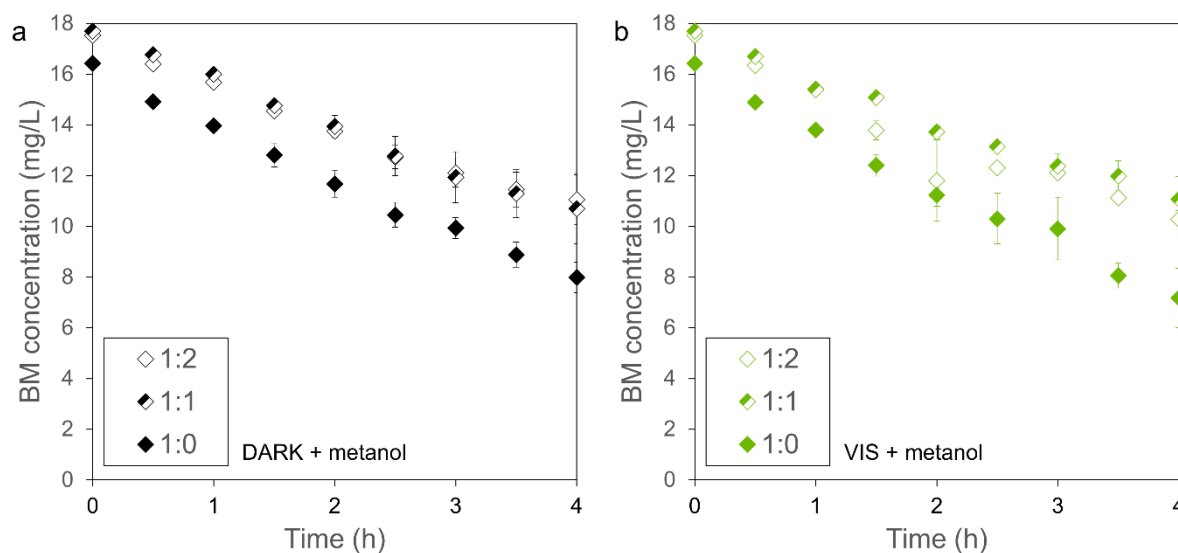


Figure S 14 Kinetics of methylene blue removal using TiO_2 -yellow at different ratio of MB solution and methanol (MB:methanol) (a) in the dark and (b) under visible light (b) (MB initial concentration 16.0 mg/L, solution volume 100 mL, error bars represent the standard deviation of the mean)

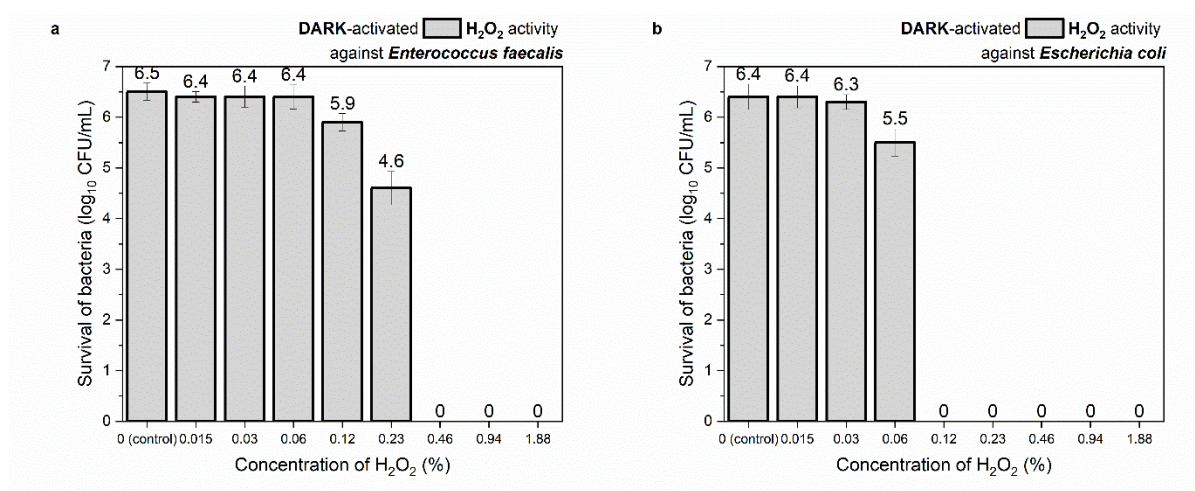


Figure S 15 The bacterial viability of *Enterococcus faecalis* (a) and *Escherichia coli* (b) at various H_2O_2 concentrations activated without illumination (c,d) (error bars represent the standard deviation of the mean)

References

- [1] A.A. Alshehri, M.A. Malik, Biogenic fabrication of ZnO nanoparticles using *Trigonella foenum-graecum* (Fenugreek) for proficient photocatalytic degradation of methylene blue under UV irradiation, *J. Mater. Sci. Mater. Electron.* 30 (2019) 16156–16173.
<https://doi.org/10.1007/s10854-019-01985-8>.
- [2] M. Koinuma, H. Tateishi, K. Hatakeyama, S. Miyamoto, C. Ogata, A. Funatsu, T. Taniguchi, Y. Matsumoto, Analysis of reduced graphene oxides by X-ray photoelectron spectroscopy and electrochemical capacitance, *Chem. Lett.* 42 (2013) 924–926.
<https://doi.org/10.1246/cl.130152>.
- [3] M.K. Rabchinskii, S.A. Ryzhkov, D.A. Kirilenko, N. V. Ulin, M. V. Baidakova, V. V. Shnitov, S.I. Pavlov, R.G. Chumakov, D.Y. Stolyarova, N.A. Besedina, A. V. Shvidchenko, D. V. Potorochin, F. Roth, D.A. Smirnov, M. V. Gudkov, M. Brzhezinskaya, O.I. Lebedev, V.P. Melnikov, P.N. Brunkov, From graphene oxide towards aminated graphene: facile synthesis, its structure and electronic properties, *Sci. Rep.* 10 (2020) 1–12. <https://doi.org/10.1038/s41598-020-63935-3>.

H₂O₂-sensitized titania with activity under visible light and in the dark

Anna Gibas^a, Agnieszka Baszczuk^a, Irena Jacukowicz-Sobala^b, Agnieszka Ciechanowska^b, Marek Jasiorski^a, Ewa Dworniczek^c, Alicja Seniuk^c, Agnieszka Lewińska^d

^a Department of Mechanics, Materials and Biomedical Engineering, Wrocław University of Science and Technology, 25 Smoluchowskiego Street, 50-370 Wrocław, Poland

^b Department of Chemical Technology, Wrocław University of Economics and Business, Komandorska St., 53-345, Wrocław, Poland

^c Department of Microbiology, Faculty of Medicine, Wrocław Medical University, Wrocław 50-368, Poland

^d Faculty of Chemistry, University of Wrocław, 14 Joliot-Curie Street, 50-383 Wrocław, Poland

Description of columns:

A No.	The serial number used also in the Table 2 in the article.
B Sensitization method	Articles are grouped in 3 sections: bottom-up synthesis, top-down modification, in situ sensitization. Additionally, papers containing photocatalytic biological studies are tagged with "BIO".
C Source	The article in the form of the hyperlink.
D Form used to obtain Ti-Based Oxides	Information about initial form of the Ti-based oxides with distinction of self-synthesized and commercial materials.
E H ₂ O ₂ sensitization procedure	The details of the sensitization with hydrogen peroxide.
F Post-treatment after H ₂ O ₂ sensitization	Information about the treatment used after sensitization.
G H ₂ O ₂ -sensitization effects	The description of the material received as a result of sensitization given by the Authors.
H Investigated VIS activity	Information about the type of the photocatalytic test with the source of the light and filters.
I Representative results	The exemplary measurement confirming the performance.
J Authors' explanation	The explanation of investigated performance.
K Investigated DARK activity	Information about the type of the dark test activity.
L Representative results	The exemplary measurement confirming the performance.
M Authors' explanation	The explanation of investigated performance.
N Investigated activity	Information about the type of the test.
O Materials factors	Typical materials features providing activity.
P Factors appearing during activity test	The activity gained during the activity test.

data from **Table 2** in the article

No.	Sensitization method	Source	Form used to obtain Ti Based Oxides	H ₂ O ₂ sensitization procedure	Post treatment after H ₂ O ₂ sensitization	H ₂ O ₂ sensitization effects	Investigated VIS activity	Representative results	Autors explanation	Investigated DARK activity	Representative results	Autors explanation	Investigated activity	Materials factors	Factors during activity test
1	bottom-up synthesis	H2O2-sensitized titania with activity under visible light and in the dark (our work)	self-synthesized TiO ₂ : titanium (IV) isopropoxide + H ₂ O + HNO ₃	adding H ₂ O ₂	drying at room temperature	amorphous TiO ₂ + layered titanates with surface covered with peroxo, superoxo and hydroxy groups, with intermediate bandgap states	degradation of methylene blue with LED lamp (max 455 nm)	75% of MB in 8 h, zero-order kinetics, k = 0.027 (mg/L) min ⁻¹	formation of oxygen-rich O–O groups: peroxo and superoxo groups; narrowed band gap ; surface hydroxylation; and amorphous layered structure	degradation of methylene blue	36% of MB in 8 h, zero-order kinetics, k = 0.014 (mg/L) min ⁻¹	formation of oxygen-rich O–O groups: peroxo and superoxo groups; surface hydroxylation; and amorphous layered structure	VIS and DARK dye degradation	adsorption peroxo groups superoxide radical	
2	bottom-up synthesis	Visible light-photosensitized, oxidation of organic pollutants using amorphous peroxo-titania	self-synthesized TiO ₂ : titanium(IV) isopropoxide	adding H ₂ O ₂	drying at 50 °C for 4 h + HCl treatment	amorphous structure with surface peroxo complexes, with particles < 10 nm, specyfic surface area 267.89 m ² /g	degradation of 4-chlorophenol, acetaminophen, phenol, benzoic acid and carbamazepine under fluorescent lamp with 400 nm cut-off filter	(1) 99% of 4-CP in 4h, k = 0.0485 min ⁻¹ (2) degradates AAP and phenol (3) does not degradates BA ands CBZ	(1) Photogenerated intermediates ([•Ti ^{IV} -OOH]• and [•Ti ^{III} -OOH]•) are responsible for selective oxidative degradation of organic compounds (via a series of electron abstraction and hydroxylation reactions) (2) ROS such as radical HO• and O ₂ ^{•-} were found to be insignificant (3) senitzitization effect is reduced by heating				VIS organic compounds degradation	peroxo group lack of heating	
3	bottom-up synthesis	In-situ creating elastic lattice OO bonds over semicrystalline yellow TiO2 nanoparticles for significantly enhanced photocatalytic H2 production	self-synthesized TiO ₂ : titanium(IV) isopropoxide + H ₂ O + HNO ₃	adding H ₂ O ₂	drying at 60 °C	amorphous structure (small share of anatase), with superoxide ions and peroxy groups, bandgap of 1.88 eV	reforming of formaldehyde with xenon with a 420 nm cut-off filter	from 6.5 to 72 μmol/g H ₂ production in 1 h	(1) superoxide ions (O ₂ ^{•-}) are consumed during tests giving lattice O-O bonds (2) O-O lattice bonds elongate to capture electrons and return to their original length after these electrons are consumed in photocatalytic reactions, which facilitates the breaking of bonds of formaldehyde				VIS hydrogen production	O–O lattice bonds formed from superoxide ions	
4	bottom-up synthesis	Enhancing Visible Light Absorption of Yellow-Colored Peroxo-Titanate Nanotubes Prepared Using Peroxo Titanium Complex Ions	self-synthesized titanates: TiH ₂ + NaOH	adding H ₂ O ₂	heating at 100 °C for 12 h	nanotubes with lepidocrocite titanate structure with peroxo titanium bonds formed in the interlayers, BET surface area of 183.1 m ² /g , bandgap of 2.5 eV, zeta potential of −28.0 ± 0.3 mV	degradation of rhodamine B under solar lamp with a 420 nm cut-off filter	64.3% of RhB degradation in 6 h	negative surface potential improve dye adsorption, bandgap narrowing, active radicals formation				VIS dye degradation	negative surface potential band gap narrowing	ROS (HO•, O ₂ ^{•-})
5	bottom-up synthesis	Facile synthesis of amorphous Ti-peroxo complex for photocatalytic activity under visible-light irradiation	self-synthesized Ti-peroxo complex: TiH ₂ powder + H ₂ O	multistep adding H ₂ O ₂	drying at 100 °C	TiH ₂ core with amorphous-peroxo complexes with surface area of 154.1 m ² /g and bandgap of 2.4 eV and different oxidation state of Ti (Ti ²⁺ , Ti ³⁺)	degradation of rhodamine B under 150 W white LED lamp	98% in 30 min, pseudo-first-order kinetics, k = 0.1 min ⁻¹ , activity maintained after 10 photocatalytic cycles	(1) excited peroxide groups transfer electrons to the TiO ₂ conduction band (2) free radicals (hydroxyl and superoxide) are generated (3) oxygen vacancies produce new donor levels (4) amorphous structure enables formation of superoxide anions				VIS dye degradation	peroxo groups oxygen vacancies amorphous structure	ROS (HO•, O ₂ ^{•-})
6	bottom-up synthesis	Dopant-free oxygen-rich titanium dioxide: LED light-induced photocatalysis and mechanism insight	self-synthesized TiO ₂ : titanium (IV) n-butoxide, H ₂ O	adding H ₂ O ₂	drying at 50 °C for 3 h + drying 100 °C for 24 h + heating at 300, 400 and 500 °C for 2 h	anatase with peroxo groups, diameter of 3–12 nm, bandgap ~ 2.9-3.0 eV	degradation of methylene blue under visible light LED	from 47% (500 °C) to 57% (300 °C) MB degradation in 240 min, pseudo-first-order kinetics, k = 0.00271 min ⁻¹ (500 °C) and 0.00447 min ⁻¹ (300 °C)	bandgap narrowing, the excess oxygen on the lattice surface of O ₂ -TiO ₂ acting as electron scavenger facilitates electron–hole pair separation				VIS dye degradation	peroxo groups band gap narrowing	ROS (HO• > h• > O ₂ ^{•-} > e•)
7	bottom-up synthesis	Visible-light-activated oxygen-rich TiO2 as next generation photocatalyst: Importance of annealing temperature on the photoactivity toward reduction of carbon dioxide	self-synthesized TiO ₂ : titanium (IV) butoxide, H ₂ O	adding H ₂ O ₂	drying at 100 °C for 24 h + heating at 200-800 °C for 2 h	amorphous structure (200 °C) and anatase/rutile mixtures (280 - 800 °C) with peroxy groups with bandgap of 2.9-3.0 eV	reduction of CO ₂ with daylight bulb	max 1.03 μmol g _{cat} ⁻¹ of total methane yield in 6 h for samples heated at 300 °C	the anatase/rutile ratio (resulting from the heating temperature) has a dominant role in enhancing the photocatalytic activity				solar methane production	phase composition	
8	bottom-up synthesis	Oxygen Rich Titania: A Dopant Free, High Temperature Stable, and Visible-Light Active Anatase Photocatalyst	self-synthesized TiO ₂ : TiCl ₄ , H ₂ O, NH ₃	adding H ₂ O ₂	heating at 50 °C for 2 h + drying at 100 °C for 24 h + heating at 600–1000 °C for 2 h	anatase band or anatase-rutile mixtures band gap ~ 2.8-3.0 eV	degradation of methylene blue under solar lamp with a 450 nm cut-off filter	600 °C: first-order kinetics, k = 0.0163 min ⁻¹ [two-fold higher than for P25]	anatase phase stability, superior textural properties (increased surface area, pore diameter and pore volume), and band gap narrowing				VIS dye degradation	anatase phase stability textural properties band gap narrowing	
9	bottom-up synthesis	Synthesis and visible light photoactivity of a high temperature stable yellow TiO2 photocatalyst	self-synthesized TiO ₂ : TiN + HNO ₃	adding H ₂ O ₂ to completely dissolve TiN	evaporation at 90 °C + drying at 150 °C + heating at 400 °C, 600 °C, 900 °C and 1200 °C	rutile with absorption edge at 400–410 nm (3.2 eV) + 450–600 nm (indirect transition) and Ti ³⁺ (600 °C) or oxygen vacancies (900, 1200 °C) depending on heating temperature with surface area 44 m ² /g (600 °C)	degradation of methylene blue under UV bulb with a 420 nm cut-off filter	90% of MB degradation in 300 min with 25% of adsorption (600 °C) 48% of MB degradation in 300 min with 18% of adsorption (900 °C) 25% of MB degradation in 300 min with 0% of adsorption (no heating)	large amounts of surface defects in the form of Ti ³⁺ ions, an increase in the red shift				VIS dye degradation	band gap narrowing Ti ³⁺	
10	top-down modification	Antibacterial Surface Coating for Bone Scaffolds Based on the Dark Catalytic Effect of Titanium Dioxide	self-prepared TiO ₂ : rutile scaffolds coated with anatase	immersing in H ₂ O ₂	drying at 37 °C for 24 h	rutile scaffold coated with anatase		degradation of methylene blue	~ 20% degradation of MB in 180 min	1) intermediate free radicals (HO• and HOO•) (2) O ₂ ^{•-} coordinated at a Ti ^{IV} site has the oxidative effect (3) oxidative power due to more abundant oxygen vacancies	DARK dye degradation	superoxide radical oxygen vacancies	ROS (O ₂ ^{•-} , HOO•)		
11	top-down modification	Hydrogen Peroxide Activated Commercial P25 TiO2 as Efficient Visible-light-driven Photocatalyst on Dye Degradation	commercial TiO ₂ : Degussa P25	adding H ₂ O ₂	drying at 60 °C	anatase-rutile mixture with bandgap energy reduced from 3.15 eV to 2.91 eV and increased amount of water physisorbed on TiO2 covered with an amorphous layer 1 nm thick	degradation of rhodamine B under xenon lamp with a 420 nm cut-off filter	~ 60% RhB degradation in 210 min	(1) peroxide complexes (≡Ti-OOH) is formed on the surface responsible for activity in visible light (2) amorphous film on crystalline P25 grains is responsible for the separation of photogenerated charges.				VIS dye degradation	peroxo groups amorphous layer	
12	top-down modification	Markedly Enhanced Surface Hydroxyl Groups of TiO 2 Nanoparticles with Superior Water-Dispersibility for Photocatalysis	commercial TiO ₂ : 100% anatase with BET surface area of 290 m ² /g and average particle size of 7 nm	adding H ₂ O ₂ -NaOH	drying at 60 °C for 24 h	well-separated primary particles with reduced crystal size (5 nm) and increased desity of OH groups (12.0 OH/nm ²)	degradation of sulforhodamine B under xenon lamp with a 480 nm cut-off filter	84% of SRB degradation in 40 min, pseudo-first-order kinetics, k = 0.033 min ⁻¹	the increase of terminal hydroxyls on the surface (reducing particle aggregation and inhibiting electron-hole recombination)				VIS dye degradation	terminal hydroxyl groups	ROS (HO•)
13	top-down modification	H2O2 Exfoliation of TiO2 for Enhanced Hydrogen Production from Photocatalytic Reforming of Methanol	commercial TiO ₂ : Aeroxide P25 (80% of anatase and 20% rutile)	adding H ₂ O ₂	drying at 80 °C	anatase content increased from 75% to 85%, degree of crystallinity increased from 45.6 to 50.0 %, crystallite size reduction from 14.7 nm to 13.1 nm, bandgap energy reduction from 3.23 eV to 3.07 eV, formation of an amorphous layer on crystalline grains	reforming of methanol under UV-visible light (350–800 nm)	~150 μmol of H ₂ production in 3 h	(1) an increase in the density of surface hydroxyl groups, which are responsible for limiting recombination processes (2) Fast transfer of charge carriers and more active sites thanks to reduced crystallite size				UV-VIS reforming of methanol	hydroxylation reduced crystallite size	
14	top-down modification	Degussa P25 TiO2 modified with H2O2 under microwave treatment to enhance photocatalytic properties	commercial TiO ₂ : Degussa P25 (81% anatase and 19% rutile, surface area of 54 m ² /g, particle size 26 nm and crystallite size of 21 nm)	adding H ₂ O ₂ during ultrasonic treatment + 60 min microwave treatment in 125 °C	drying at 100 °C for 1 day	hydroxylated antase-rutile mixture with increased rutile share (25%) and crystallinity, but increased crystallinite size (25 nm), reduced particle size (18 nm), increased surface area increase (80 m2g-1)	degradation of rhodamine B under solar irradiation	51% pf RhB in 120 min, pseudo-first-order kinetics, k = 0.026 min ⁻¹	surface disorder, such as Ti ³⁺ , Ti-OH, and oxygen vacancies, and size distribution of the anatase/rutile phases				solar dye degradation	surface defects (Ti ³⁺ , Ti-OH, oxygen vacancies) size distribution	
15	in-situ sensitization	Mechanism of Photodecomposition of H2O2 on TiO2 Surfaces under Visible Light Irradiation	commercial TiO ₂ : Degussa P25 (80% anatase, 20% rutile; 50 m ² /g)	adding H ₂ O ₂ to TiO ₂ suspension and then to salicic acid	none	not investigated	degradation of salicylic acid under halogen lamp	spectrophotometric method: for 7 h about 70% salicylic acid was degraded, zero-order kinetics with k = 0.01 TOC: mineralization yield of salicylic acid was about 25% after irradiation for 4 h	formation of active HO• radicals in the decomposition of H ₂ O ₂ which possess strong oxidation ability and may cause oxidation reaction of organic compounds adsorbed on the TiO ₂ surface (surface electron transfer from the surface complex to the TiO ₂ conduction band)				VIS degradation of organic compound		ROS (HO•)
16	in-situ sensitization	Enhanced visible-light photocatalytic activity of a TiO2 hydrosoal assisted by H2O2: Surface complexation and kinetic modeling	self-synthesized TiO ₂ : hydrosols from H ₂ TiO + H ₂ O + NH ₃ (until the pH exceeded 9) + HNO ₃ (to reduce pH to 1.5) (anatase)	adding H ₂ O ₂ to TiO ₂ hydrosol-MB solution	none	not investigated	degradation of methylene blue under xenon lamp with a UV cutoff filter at 420 nm and 400 nm	50-90% of MB with H ₂ O ₂ , pseudo-first-order kinetics, k = 0.002-0.012 min ⁻¹	(1) solution-phase H ₂ O ₂ played a critical role in the system: H ₂ O ₂ in the solution may function as an electron acceptor to subsequently generate reactive oxygen species (ROS)				VIS dye degradation		ROS (HO•)
17	in-situ sensitization	Oxidative power of aqueous non-irradiated TiO2-H2O2 suspensions: Methylene blue degradation and the role of reactive oxygen species	commercial TiO2: Degussa P25, Kronos 1171, Hombitan Anatase, Sigma Aldrich rutile and Sensient Eurovit	adding H ₂ O ₂ to TiO2-dye suspension with pH adjustment	none	not investigated		degradation of methylene blue	i.e. 100% in 10 min (P25 at ph 6.7)	(1) ROS (O ₂ ^{•-} , HOO•) (2) adsorption due to more negative surface potential (superoxide radical anions O ₂ ^{•-})	DARK dye degradation	superoxide radical	ROS (HO•, O ₂ ^{•-} , HOO•) and H ₂ O ₂		

18	in-situ sensitization	Antibacterial Surface Coating for Bone Scaffolds Based on the Dark Catalytic Effect of Titanium Dioxide	self-prepared TiO ₂ : rutile scaffolds coated with anatase	adding H ₂ O ₂ into scaffold-dye system	none	not investigated				degradation of methylene blue	~ 90 % degradation in 180 min	1) intermediate free radicals (HO [•] and HOO [•]) (2) O ₂ ^{•-} coordinated at a Ti ^{IV} site has the oxidative effect (3) oxidative power due to more abundant oxygen vacancies	DARK dye degradation	superoxide radical oxygen vacancies	ROS (O ₂ ^{•-} , HOO [•])
19	in-situ sensitization	Titanate nanosheets as highly efficient non-light-driven catalysts for degradation of organic dyes	self-synthesized titanate: Li ₂ CO ₃ , K ₂ CO ₃ and TiO ₂ + HCl at 1000 °C (stacked nanosheets with BET surface area (~50 m ² /g)	adding H ₂ O ₂ into titanate-dye solution with desired pH	none	not investigated				degradation of rhodamine B, methylene blue, malachite green and methyl violet	~ 95% of RhB degradation in 120 min, first-order kinetics, k = 0.0232 min ⁻¹ ~70% of RhB degradation in 120 min	(1) peroxo groups (2) large surface area to adsorb H ₂ O ₂	DARK dyes degradation	peroxo groups high surface area	
20	in-situ sensitization	Synergetic catalysis enhancement between H2O2 and TiO2 with single-electron-trapped oxygen vacancy	self-synthesized TiO ₂ : ultrasonic treatment of TiCl ₄ + H ₂ O + NH ₃ (anatase-amorphous powders with lattice defects)	adding H ₂ O ₂ to TiO ₂ sols and then to dyes solutions	none	not investigated				degradation of rhodamine B, methyl orange and tetracycline	~ 90% of RhB in 90 min ~ 80% of MO in 150 min ~ 70% of tetracycline in 24 h	(1) oxygen vacancies (2) ROS (O ₂ ^{•-} , HOO [•] , HO [•])	DARK dyes degradation	oxygen vacancies	ROS (O ₂ ^{•-} , HOO [•] , HO [•])
21	in-situ sensitization	Bleaching of Methylene Blue by Hydrated Titanium Dioxide	self-synthesized TiO ₂ : TiCl ₄ + NH ₃ (mainly amorphous TiO ₂ with 5% of anatase, highly hydrated surface with BET surface area 237 m ² /g)	adding H ₂ O ₂ to the TiO ₂ -dye system	none	not investigated				degradation of methylene blue	95.47% of MB in 1 h	(1) presumably due to adsorption rather than photocatalyzed degradation (2) amorphous surface adsorbs higher number of H ₂ O ₂ and MB molecules due to more abundant OH groups and higher surface area	DARK dyes degradation	adsorption amorphous structure (high surface area, hydroxylation)	
22	BIO in-situ sensitization	Inactivation of Enterococcus sp. by photolysis and TiO2 photocatalysis with H2O2 in natural water	commercial TiO ₂ : 20% rutile, 80% anatase with a particle size of 500 µm	adding H ₂ O ₂ to TiO ₂ and bacterial suspension	none	not investigated	bacterial viability of <i>enterococcus</i> (Gram-positive) under UVA and visible radiation (320–800 nm)	slightly less efficiency of light/TiO ₂ /H ₂ O ₂ (1.7 log ₁₀ CFU/mL removal) compared to light/TiO ₂ systems (2.3 log ₁₀ CFU/mL removal)	(1) the molecules of hydrogen peroxide present in the aqueous colloidal suspension have filled spaces in the TiO ₂ surface (2) the low dose of H ₂ O ₂ used in the experiments, unable to generate enough oxidative stress on <i>Enterococcus</i> sp. (3) hydroperoxide radicals are less active as regards disinfection				solar bacterial activity	adsorption HO [•] radicals from TiO ₂	H ₂ O ₂ ROS
23	BIO in-situ sensitization	Effect of pH, inorganic ions, organic matter and H2O2 on E. coli K12 photocatalytic inactivation by TiO2: Implications in solar water disinfection	commercial TiO ₂ : P25 (mainly anatase, specific surface area 50 m ² /g)	adding H ₂ O ₂ to TiO ₂ and bacterial suspension	none	not investigated	bacterial viability of <i>E. coli</i> K12 (Gram-negative) under solar lamp (UV+VIS)	light/TiO ₂ /H ₂ O ₂ system is 1.5-fold more efficient than light/TiO ₂ (7 log ₁₀ CFU/mL removal in 40 and 60 min respectively)	(1) direct action of H ₂ O ₂ (free radicals formation) (2) supplementary increase of radical HO [•] generation in the contact with TiO ₂ holes				solar bacterial activity	HO [•] radicals from interaction phenomenon between TiO ₂ and H ₂ O ₂	HO [•] radicals from H ₂ O ₂
24	BIO in-situ sensitization	Inactivation of Clostridium perfringens spores and vegetative cells by photolysis and TiO2 photocatalysis with H2O2	commercial TiO ₂ : anatase heated at 900 °C (anatase-rutile mixture with particles of 500 µm diameter and specific area 6.43 m ² /g)	adding H ₂ O ₂ to TiO ₂ and bacterial suspension	none	not investigated	bacterial viability of <i>C. perfringens</i> vegetative cells (gram-positive) under xenon lamp with a 320 nm cut-off filter	result for light/TiO ₂ /H ₂ O ₂ (7 log ₁₀ CFU/mL removal) system are similar to light/H ₂ O ₂ system (8.5 log ₁₀ CFU/mL removal) and light/TiO ₂ system (6 log ₁₀ CFU/mL removal)	(1) only H ₂ O ₂ decomposition (2) no interaction phenomenon between TiO ₂ and H ₂ O ₂	bacterial viability of <i>C. perfringens</i> vegetative cells (gram-positive)	slight disinfectant effect (0.5 log ₁₀ CFU/mL removal)	(1) only H ₂ O ₂ decomposition (2) no interaction phenomenon between TiO ₂ and H ₂ O ₂	solar and DARK bacterial activity	HO [•] radicals from interaction phenomenon between TiO ₂ and H ₂ O ₂	HO [•] radicals from H ₂ O ₂
25	BIO bottom-up synthesis	Antibacterial Surface Coating for Bone Scaffolds Based on the Dark Catalytic Effect of Titanium Dioxide	self-prepared TiO ₂ : rutile scaffolds coated with anatase	immersing scaffolds to H ₂ O ₂	drying at 37 °C for 24 h	rutile scaffold coated with anatase				bacterial viability of <i>Staphylococcus epidermidis</i> Xen43 (coagulase-negative) and <i>Staphylococcus epidermidis</i> 1457 (coagulase-negative)	scaffolds were unable to prevent biofilm formation (2 log ₁₀ and 1 log ₁₀ CFU/sample removal for 4 and 12 h, respectively)	(1) high oxidative environment due to superoxide radicals (O ₂ ^{•-}) stabilized on TiO ₂ (2) ROS-mediated killing mechanism (3) O ₂ ^{•-} consumption is a cause of lack of long-term activity	DARK bacterial activity	superoxide radicals	ROS (O ₂ ^{•-})
26	BIO bottom-up synthesis	H2O2-sensitized titania with activity under visible light and in the dark (our work)	self-synthesized TiO ₂ : titanium (IV) isopropoxide + H ₂ O + HNO ₃	adding H ₂ O ₂	drying at room temperature	amorphous TiO ₂ + layered titanates with surface covered with peroxo, superoxo and hydroxy groups, with intermediate bandgap states	photocatalytic inactivation of <i>E. faecalis</i> (Gram-positive) and <i>E. coli</i> (Gram-negative) under Xenon lamp (UV+VIS)	MBC _{enterococcus} = 750 µg/mL MBC _{coli} = 375 µg/mL (6 log ₁₀ CFU/mL removal)	(1) ROS-mediated killing mechanism. (2) high oxidative environment due to the presence of adoxygen groups	catalytic inactivation of <i>E. faecalis</i> (Gram-positive) and <i>E. coli</i> (Gram-negative)	MBC _{enterococcus} > 1500 µg/mL MBC _{coli} = 1500 µg/mL (6 log ₁₀ CFU/mL removal)	(1) the effect of photoinduced ROS introduced prior the antimicrobial test (2) high oxidative environment due to the presence of adoxygen groups	solar and DARK bacterial activity	residual ROS superoxide radicals peroxo groups	